Redesign and Testing of a Surface UnderSea Kite Model

A Major Qualifying Project Report
Submitted to the Faculty of the
WORCESTER POLYTECHNIC INSTITUTE
in Partial Fulfillment of the Requirements for the
Degree(s) of Bachelor of Science in:

Aerospace Engineering
by:

_____
Olivia Chiasson

_____
Adrianne Curtis

_____
Zachary Sotland

_____
Andrew Ventura Molina

Aerospace Engineering and Physics
by:

_____
Thomas Rau

Approved
by:

_____
David J. Olinger, Advisor
Professor, Aerospace Engineering Department
Worcester Polytechnic Institute

_____
Nancy A. Burnham, Co-Advisor
Professor, Physics Department
Worcester Polytechnic Institute

Table Of Contents

Abstract

Surface UnderSea Kites (SUSK) are an emerging renewable tethered ocean energy technology. SUSK systems use a vertical underwater wing suspended beneath a surface hull that moves cross-current in a simple arc on the ocean surface. This concept moves the tether above the water surface to reduce tether drag and increase wing speed and power output. Our project builds on earlier tethered energy research at WPI. A SUSK scale-model with a higher aspect ratio wing, improved hull configuration and new turbine was designed, analyzed, and tested. We determined the optimal hull shape for our design that will maximize stability in the water. A 3D printed Wells turbine within a converging nozzle at the lower wingtip allows for increased power output during SUSK motions along the ocean surface arc.

Acknowledgements

We would like to thank the following individuals and groups for their help and support throughout the entirety of this project.

- Professor Olinger & Professor Burnham
    - Our advisor and co-advisor for their guidance, insight, and support throughout the course of the project.
- Paul Bennett and WPI Sports & Recreation Center Lifeguards
    - For assistance with Pool Testing
- Mitra Varun Anand
    - Makerspace Advanced Technology & Prototyping Specialist, for assisting with methods upon 3D Printing.
- Tina Stratis
    - Aerospace Engineering Department Secretary, for helping coordinate weekly MQP meetings, and assisting with purchase orders.

Table of Authorship

Section	Writing Completed by	Work Completed by
Cover Page	OC	
Table of Contents	ZS	
Abstract	ALL	
Acknowledgements	ALL	
Table of Authorship	TR	
List of Figures	ALL	
List of Tables	ALL	
List of Nomenclature	TR	
[1.1.1]	AC	
[1.1.2]	AC	
[1.1.3]	AC	
[1.1.4]	ZS	
[1.1.5]	AVM	
[1.1.6]	OC	
[1.1.7]	OC	
[1.2]	TR	
[1.3]	TR, ZS	
[1.4]	OC	
[1.5]	TR, ZS	
[1.6]	TR, ZS	
[2.1]	TR	ALL
[2.2.1]	ZS	ZS
[2.2.2]	ZS	ZS
[2.2.3]	ZS	ZS
[2.3.1]	OC	OC, AVM
[2.3.2]	OC	OC, AVM
[2.3.3]	AVM	OC, AVM
[2.3.4]	AVM	OC, AVM

[2.4.1]	AC	AC
[2.4.2]	AC	AC
[2.4.3]	AC	AC
[2.4.4]	ZS	ZS
[2.4.5]	ZS	ZS
[2.5.1]	TR	TR
[3.1.1]	ZS	ZS
[3.1.2]	ZS	ZS
[3.1.3]	ZS	ZS
[3.2.1]	TR	TR
[3.2.2]	TR	TR
[4.1.1]	TR*	TR*
[4.1.2]	TR*	TR*
[4.1.3]	TR*	TR*
[4.2.1]	TR*	TR*
[4.2.2]	TR*	TR*
[4.2.3]	TR*	TR*
[5.1]	ZS	
[5.2]	AC	
[5.3]	ZS	
[5.4]	ZS	
Appendix's	TR*, ZS	
References	ALL	

KEY:	
OC	Olivia Chiasson
AC	Adrianne Curtis
TR	Thomas Rau
ZS	Zachary Sotland
AVM	Andrew Ventura Molina
*** Indicates work incorporated for a double major in Physics**	

List of Figures

List of Tables

1 Introduction

1.1 Background and Literature Review

1.1.1 Renewable Energy

Since the beginning of the Industrial Revolution (approximately from the mid 1700s - mid 1800s), nonrenewable resources have dominated energy production in various forms, mainly from the use of fossil fuels. The use of these resources has been a large topic of concern for the past several decades due to the impact they have on the environment, and the lessening abundance of these resources needed to create fuels and electricity.

In order to offset the need for fossil fuels, various forms of renewable energy sources are under development. Some of the major sources include biomass, hydropower, geothermal, wind and solar power. According to the US Energy Information Administration, only 12% of energy consumption in The United States can be attributed to renewable resources as of 2020. While within this 12%, only 22% of the renewable energy was derived from hydroelectric power (US Energy Information Administration, 2020). The most substantial provider of renewable energy is biomass, which is primarily from biological waste and wood products.

1.1.2 Hydrocarbon and Fossil Fuel Concerns

Fossil fuels are considered hydrocarbons due to the fact that they are derived from deceased carbon based life that has been buried beneath sedimentary rock and underground reservoirs. Once the oil or gas has been extracted, these materials can be processed into fuel to power cars, generators and other appliances. As of 2019, 80% of the domestic energy produced by the United States can be attributed to the consumption of fossil fuels (Sanchez, 2020). The remaining 20% can be attributed to nuclear power, renewable sources and others.

The use of fossil fuels has been a major contributor to the climate crisis over the past several decades. The use of natural gas, crude oil and coal are all culpable of air and water pollution, while the greenhouse effect and second hand issues such as erratic weather and decrease in biodiversity are due to climate change through the use of these fossil fuels. Even deciding to discontinue the use of these fuels immediately may not be able to reverse the effects of climate change.

In addition to the negative impact these resources have on the environment, they are also limited in their supply. The need for energy production is growing dramatically due to an increasingly large population. As of 2021, Earth's human population is approaching 8 billion, requiring a massive amount of resources to sustain our energy needs. According to The Millenium Alliance of Humanity, an initiative of Stanford University, naturally occurring oil, gas and coal reserves will be depleted by the year 2100 and will need replacements.

1.1.3 Air, Current, and Tidal Power

To combat the need for harmful fossil fuels, several sources of renewable energy are being studied, including wind and marine hydrokinetic power. Turbines are present in both wind and hydrokinetic power, making them a major component of renewable energy production. To generate energy, water or air flows across the turbine blades causing them to spin. The rotors are connected to a generator, allowing the force of the fluid on the turbine wings to create electricity.

One popularized method utilizing air power is the use of wind turbines. These structures can be built on land or in the sea. When there are wind turbines built in large quantities they are called ‘farms’. The Rampion Offshore Wind Farm located off the Sussex Coast within the English Channel is able to supply 350,000 homes with electricity utilizing 116 turbines. The electricity powering these homes requires about 1,400 GWh to be produced every year. The contributions of his wind farm has saved 600,000 tons of carbon dioxide emissions per year in the UK (Rampion Offshore Wind, 2021).

Power produced by dams and tidal power plants are other options for utilizing renewable energy. According to the Bureau of Reclamation, the Hoover Dam is able to generate about 4 billion KWh per year to 1.3 million residents (Bureau of Reclamation, 2018). This location takes up less space than the Rampion Offshore Wind farm, but utilizes water power to generate substantially more power within the structure. The Mutriku Wave Power Plant utilizes an oscillating water column to generate electricity, but wave and tidal power is not as commonplace, as of now this powerplant can only produce enough energy to sustain 250 homes using 16 Well’s Turbines (Power Technology, 2020). This power plant has broken records in energy production within the tidal and wave power sectors.

Other options are also available, but most are still in the developmental phase and not yet in widespread use.

1.1.4 Tethered Energy

Airborne wind energy (AWE) was developed as a renewable energy alternative to wind turbines. While traditional wind turbines have a height of around 100 meters, AWE systems use tethered kites or wings to harness energy at altitudes over 500 meters (*Airborne wind energy*, 2019). This results in higher energy production with faster and more consistent winds at those increased altitudes. Using previous studies, it can be seen that there is a potential for 7.5 TW of AWE production using jet stream winds (Miller, 2011). This being almost half of the current global energy usage, AWE represents a viable option for renewable energy.

There are two main types of AWE systems, being spooled tether and fixed tether systems, shown in Figure 1.

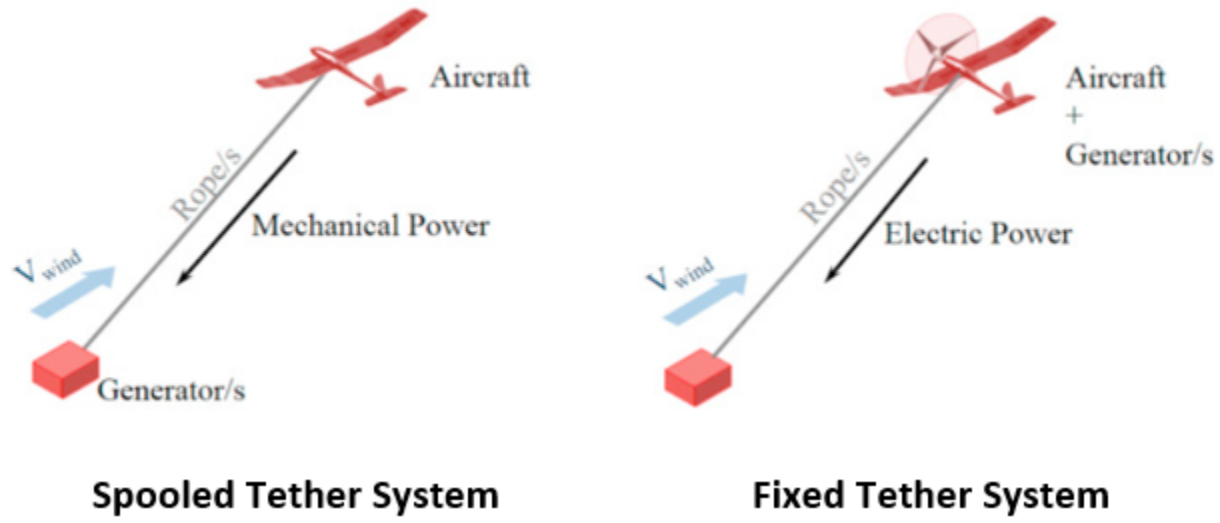

Figure 1: Comparison of Spooled Tether vs. Fixed Tether AWE Systems (Cherubini et al., 2015) Copyright 2015 Elsevier.

Fixed tether systems connect a location on the ground to a kite at a fixed length, where the generator and turbine are located on the kite, using similar energy production methods to traditional wind turbines. Spooled tether systems use a rope or cord that is able to retract and extend so that the generator can produce mechanical energy while the tether is changing length. AWE systems introduce a component of drag from the tether compared to traditional wind turbines, however the increased wind speeds at higher altitudes are great enough to overcome the loss to drag. Another issue arises when there is not enough wind to keep the kite moving in the air, and it falls to the ground where you would have to send it back up again when there is more wind, making the system not fully autonomous like traditional wind turbines.

Tethered undersea kites (TUSK) are a spin off of AWE systems and utilize water and ocean currents instead of air to generate energy. They are similar to AWE systems in that there are also the same two main types of TUSK systems, being spooled tether and fixed tether. The only difference is that the tether is underwater connected to a point on land or a buoy, or connected to the floor of the body of water. This results in a shorter tether needed than the ones hundreds of meters long for AWE systems. However, the drag from the tether is significantly greater due to the density of water being 800 times that of air. This ends up not being as big of a factor because the increased density also increases the power generated by the system. To determine the power generated by these systems we use equations 1.1, 1.2 and 1.3.

$$P = \frac{1}{2}\rho V^3 \tag{1.1}$$

$$P_{water} = \rho_{water} * V^3_{water} \tag{1.2}$$

$$P_{air} = \rho_{air} * V^3_{air} \tag{1.3}$$

Note: P = power density, ρ = density, V = velocity

To determine the increase in power that a TUSK system produces versus a AWE system we chose potential locations where these systems could be placed to use possible velocity measurements. For the AWE system, Boston was chosen since it has the highest wind speeds of any city in the US with 11.5 mph, as well as having a close proximity to WPI (*Wind speed 2018,* 2018). For the TUSK system, the Gulf stream was chosen, due to its fast moving water of 4 mph, and its proximity to the US east coast (US Department of Commerce, 2013). Additionally, using 998 kg/m^2 as the density of water and 1.225 kg/m^2 as the density of air, equations 1.2 and 1.3 produce a ratio of increased power from TUSK versus AWE.

$$P_{water} = 998\left[\frac{kg}{m^2}\right] * 4^3\,[mph]$$

$$P_{air} = 1.225\left[\frac{kg}{m^2}\right] * 11.5^3\,[mph]$$

$$\frac{P_{water}}{P_{air}} = \frac{63872}{1863.1} \cong 34$$

As seen through these calculations, AWE systems produce 34 times more power when placed at these specific locations. This is due to the increased density of water as compared to air, even though there is increased drag and decreased velocities in water. Note that this calculation does not account for the drag from both systems, although the power output from a TUSK system would still be significantly greater than that of the AWE system. Even placing a TUSK system in a location where the water velocity is half of the previous calculation, the power produced would still be about 4.3 times that of the same AWE system.

Surface undersea kites (SUSK) represent a modification of a TUSK system. Instead of the kite being fully submerged with a tether, the kite is now connected to a boat or small craft that is floating on top of the water. This aims to minimize drag by removing the tether from being submerged to now being above the water connected to the boat. Now with only the kite being submerged, the system will be able to produce more energy with less drag. The SUSK system can be seen in Figure 2.

Challenges arise in SUSK systems as to what designs to use for the boat, and how to attach a turbine. Different hull designs and shapes have been studied, such as a flat bottom, round bottom, and V bottom hull, as well as the multihull catamaran style, while multiple turbine locations are possible, such as connecting one to the hull, top of wing, or bottom of wing (Petilli, 2021). For this project we have selected the catamaran style hull with the turbine at the bottom of the wing.

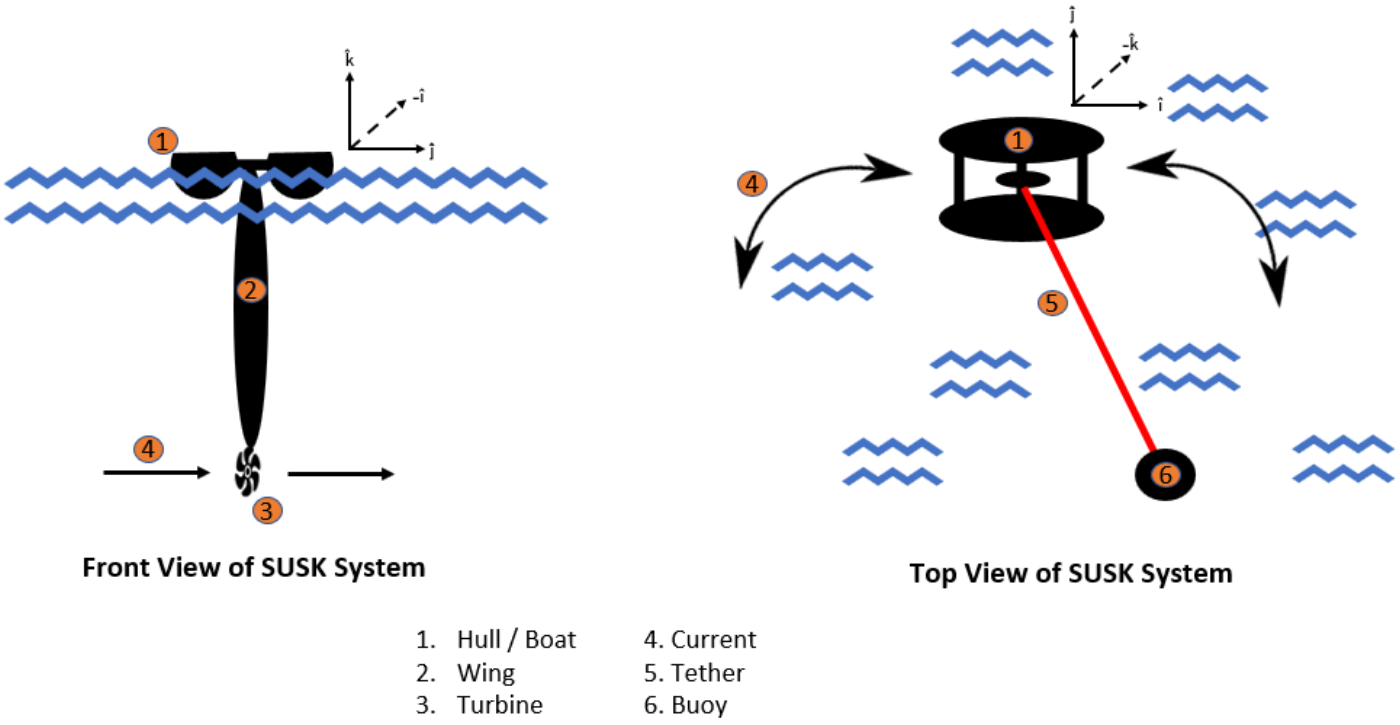

Figure 2: The SUSK System

1.1.5 Potential use for SUSK system

Minesto Inc. created a system that concentrates on underwater turbine kites which generate power from water. The team of researchers and engineers were able to create an underwater kite that was able to fly ten times faster than the water currents in the ocean. They accomplished this by attaching a turbine to the kite itself. The technology generates electricity from streams and currents, moving in an infinity symbol pattern with the help of onboard control systems and rudders. Although they created a TUSK system, they proved there was potential in underwater energy generation. Developing a SUSK system will be different as we are not focusing on the current itself, but creating our own movement in the water itself. The image below shows a drawn model of the Minesto Inc. underwater kite.

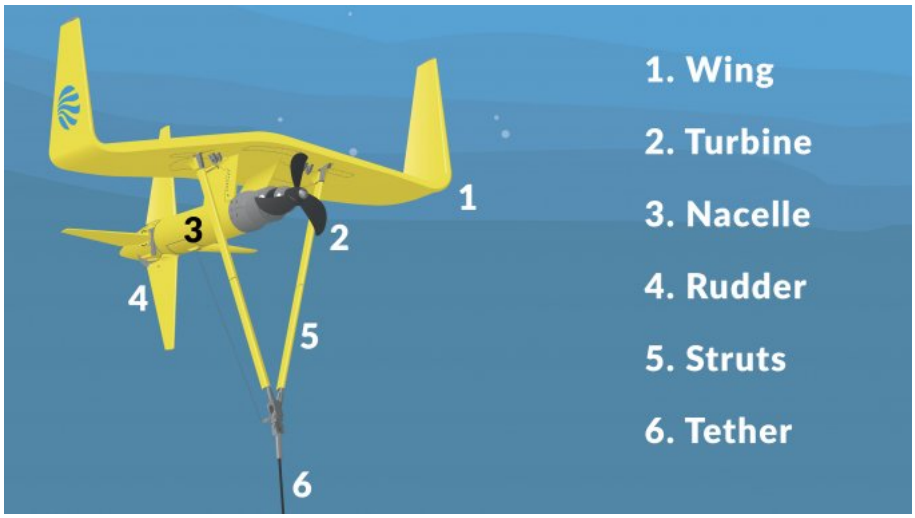

Figure 3: Minesto Inc. TUSK System Copyright 2021 Minesto Inc.

If the system can be created at a low cost, it may help low-income towns or other nations for generating power needed for heat, lighting, regular power consumption, etc. The expansion and development of marine hydrokinetic power will not only benefit people, but the earth itself. Renewable energy is important to the state of our planet and pushing to use clean energy will create a healthier environment.

1.1.6 Previous Research on Tethered Ocean Energy

The recent surge in renewable energy studies, specifically AWE and marine hydrokinetic technologies, has led to numerous research projects involving TUSK and SUSK. WPI is an innovative institution so it comes as no surprise that professors, graduate, and undergraduate students here have played a massive role in such research. Professor Olinger has published numerous articles on the topic and overseen many student projects. In one of Olinger's most recent articles with Yao Wang they discuss hydrokinetic energy technology such as TUSK and its different concepts (2015). The concepts discussed were "an axial-flow turbine mounted on a rigid underwater kite to extract power from an ocean current or tidal flow" and the second concept "...removes the turbine from the kite, and instead generates power by transmitting hydrodynamic forces on the kite through the flexible underwater tether to a generator on a floating buoy." For these two concepts, power output was estimated and comparisons were made between the key parameters of conventional turbines and TUSK systems. The two concepts are pictured in Figure 4.

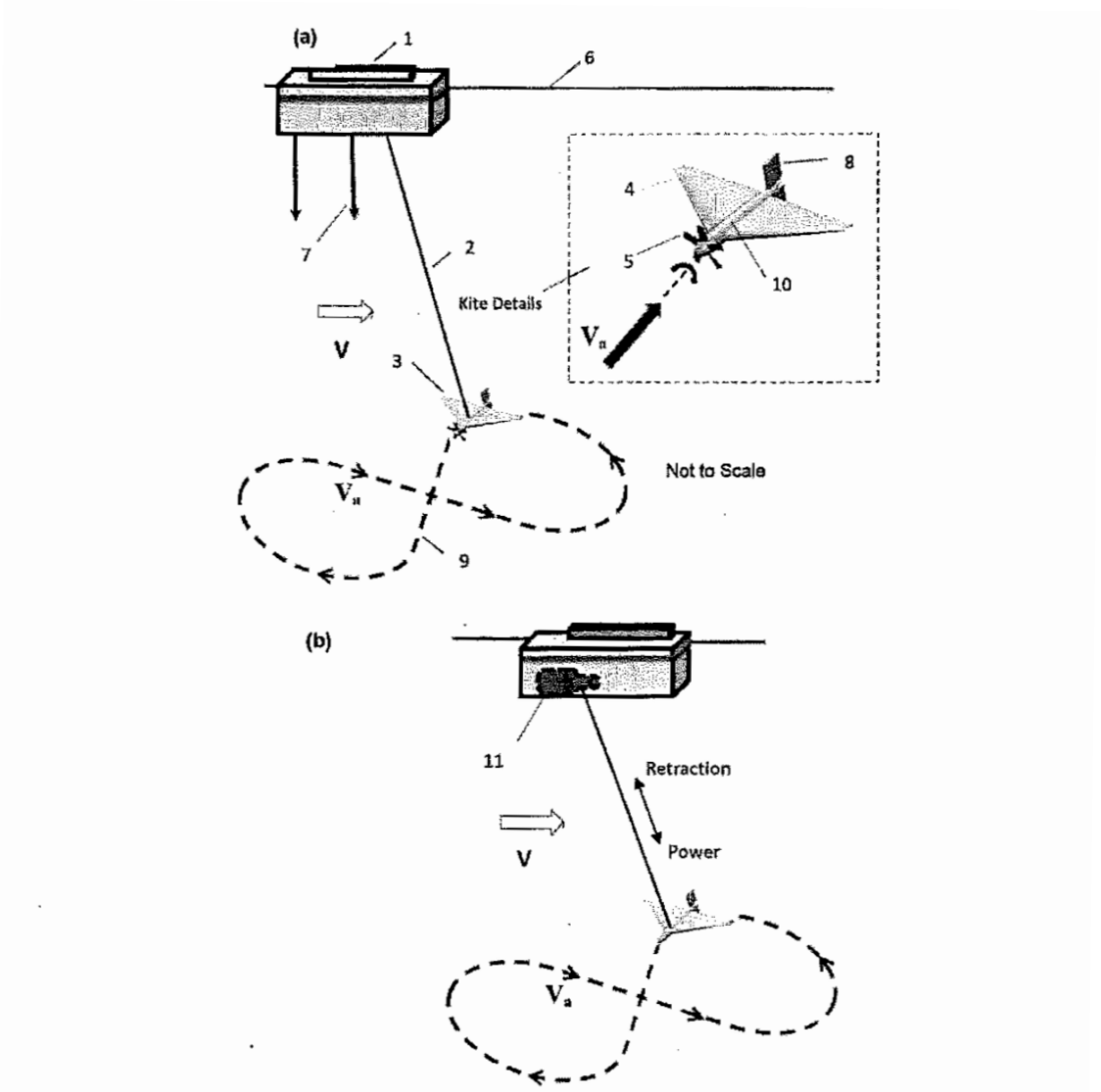

FIG. 1. (a) Kite mounted turbine (SubGen) TUSK concept. 1: Floating buoy; 2: TUSK tether; 3: kite; 4: wing; 5: turbine generator; 6: ocean surface; 7: mooring lines to ocean floor (also transmit electricity to distribution networks); 8: rudde control surfaces; 9: cross-current figure-8 kite motion; 10: fuselage with internal ballast tanks. (b) BuoyGen TUSK concept 11: spool and generator/motor.

Figure 4: Different TUSK Concepts (Olinger & Wang, 2015). Copyright 2015 American Institute of Physics (AIP).

In their study a comparison of TUSK, AWE, and marine turbine parameters were made and can be seen in Figure 5.

TABLE I. Comparison of TUSK, AWE, and marine turbine parameters.

	Parameter	TUSK	AWE	Marine turbine (MHK)	Ratio: TUSK/AWE	Ratio: TUSK/MHK	Notes
A	ρ (kg/m^3)	1025	1.18	1025	868	1.0	Seawater; AWE at 300 m altitude
B	V (m/s)	2.0	8.0	2.0	0.25	1.0	Current, wind speeds
C	C_L	1.0	1.0	...	1.0	...	Kite lift coefficient
D	C_D	0.142	0.142	...	1.0	...	Kite drag coefficient
E	C_L/C_D	7.0	7.0	...	1.0	...	Kite lift-to-drag ratio
F	V_a (m/s)	9.33	37.33	2.0	0.25	4.66	$V_a = \frac{2}{3}\frac{C_L}{C_D}V$
G	A_K (m^2)	35	35	35	1.0	1.0	Kite area for MHK: $A_T = A_K$
H	P' (kw/m^2)	416	30.7	4.1	13.5	101.5[a,b]	Power density $P' = \frac{1}{2}\rho V_a^3$
I	P (kW)	1040	77	85	13.5	12.2[b]	Power[c]
J	q (kN/m^2)	44.6	0.82	2.1	54.3	21.2	Dynamic pressure $q = \frac{1}{2}\rho V_a^2$
K	W/A_K (kN/m^2)	4.5	0.082	...	54.3	...	Wing loading $(C_L = 0.1)\ \frac{W}{A_K} = \frac{1}{2}\rho V_a^2 C_L$
L	Re[d]	$\sim 2 \times 10^7$	$\sim 6 \times 10^6$	...	3.33	...	Reynolds number

[a]Ratios in the TUSK/Marine Turbine column differ between rows H and I because the row H power densities compare two turbines of the same frontal area which is different (smaller) than the kite area, while row I uses a marine turbine frontal area = kite area (larger). The two ratios differ by a factor of $A_K/A_T = 8.3$ which is a reasonable area ratio for a TUSK system.
[b]27/16 × zeta factor $= \xi = (1/4)C_L(C_L/C_D)^2$, $A_T = A_K$.[3,4]
[c]Power calculated using $P = (2/27)\rho V^3 A_K C_L (C_L/C_D)^2$ for TUSK, AWE;[2,3] $P = (1/2)C_P \rho V^3 A_T$ for MHK with $C_P = 16/27$.
[d]Kite Reynolds number based on V_a and assumed kite chordlength of c = 2.5 m.

Figure 5: Comparison of Renewable Energy Technologies (Olinger & Wang, 2015).

The parameters found were then used in a simulation where results showed that TUSK systems would be feasible with current technology. Marine turbines (MHK) have also been studied by North Carolina State University program members in 2020. The research examined two configurations, one in which the kite was suspended from a surface-mounted platform, and

another in which the kite was deployed from the seabed. They created simulations for the configurations and used these to demonstrate the effectiveness of the control system in terms of power generation and robust flight. The simulations showed "robust flight control in the presence of turbulence, along with power production numbers approximately 90 percent as large as in the constant flow case" (Reed et al., 2020). North Carolina State University's CORE LAB also has professors who have key areas of research in dynamic modeling and control system design for tethered marine hydrokinetic energy systems. One professor, Dr. Vermillion collaborated on the research for "An Integrated Model of the Flight and Tether Dynamics of a Marine Hydrokinetic Energy Harvesting System" (Alvarez et al., 2021). Their latest focus with this research was to explore kite dynamics sensitivity to tether parameters and "address the need for a simple model capturing the interplay between [those] systems" (Alvarez et al., 2021). A partial differential equation model was created of the tether dynamics using an elastic tether. The coordinates for this system are seen in Figure 6.

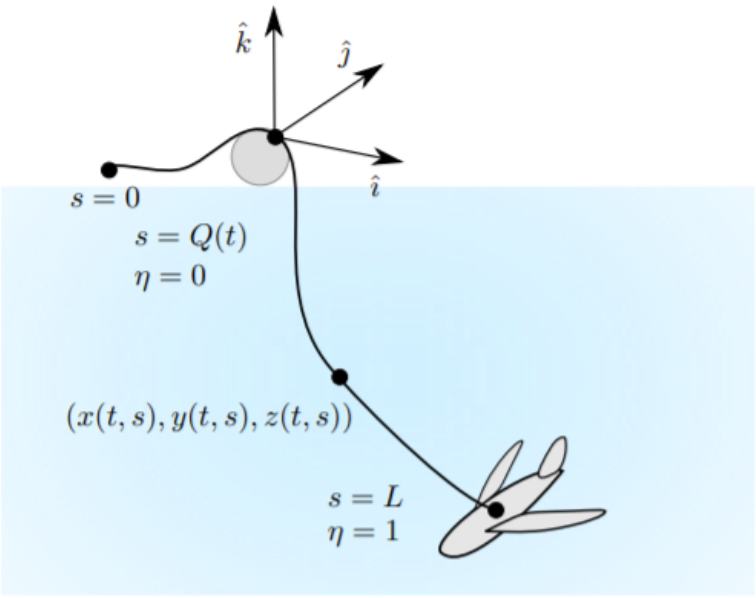

Figure 6: Elastic Tether Components for PDE Model (Alvarez et al., 2021). Copyright 2021 European Control Conference (ECC).

The trajectories were compared for kites following a typical figure-8 trajectory for a kite with this elastic tether versus a kite that had the tether as a kinematic restrain. The effect of mass was the most significant of the tether parameters that the research explored, requiring "considerably more control authority to achieve desired figure-8 trajectory, than the kite with a massless tether" (Alvarez et al., 2021). Following much of the outside research, the subject has sparked the interest of college project work.

1.1.7 Previous Project Research at WPI on Tethered Ocean Energy

Professor Olinger's research was expanded upon by a Major Qualifying Project (MQP) research group in 2014. The team aimed to design a scale-model of a rigid, tethered undersea kite with an attached turbine that could be used for power generation. The team hoped that their project would help determine "the feasibility of producing power with a TUSK system" (Aye-Addo et al., 2014). The project was divided into three subsections; hydro-kite design, electricity generation, and a motion support system. The hydro-kite was composed of a pylon, wing, turbine, nacelle, and rudder all aided in proving the advantages of incorporating 3D printing in the manufacturing process. The electricity generation section aimed to figure out the amount of power transmission from the generator and turbine. The motion support system included a gimbal, tether, and several connection points. Figure 7 shows the 2014 MQP team's hydro-kite CAD design.

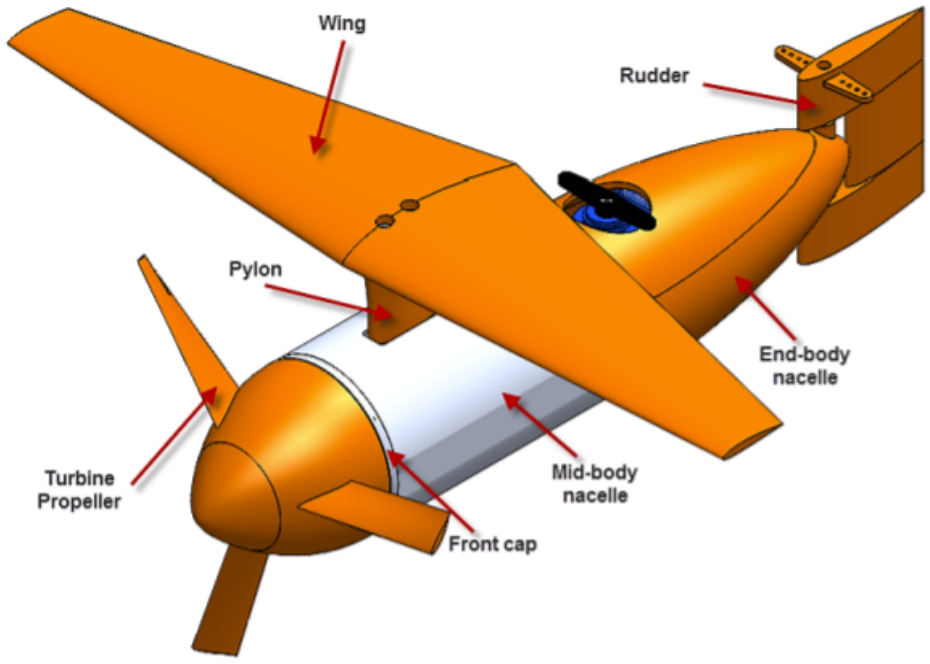

Figure 7: Isometric View of CAD Drawing of Hydro-Kite (Aye-Addo et al., 2014)

The team was unable to test their full system before completion of their project but the testing model is seen in Figure 8.

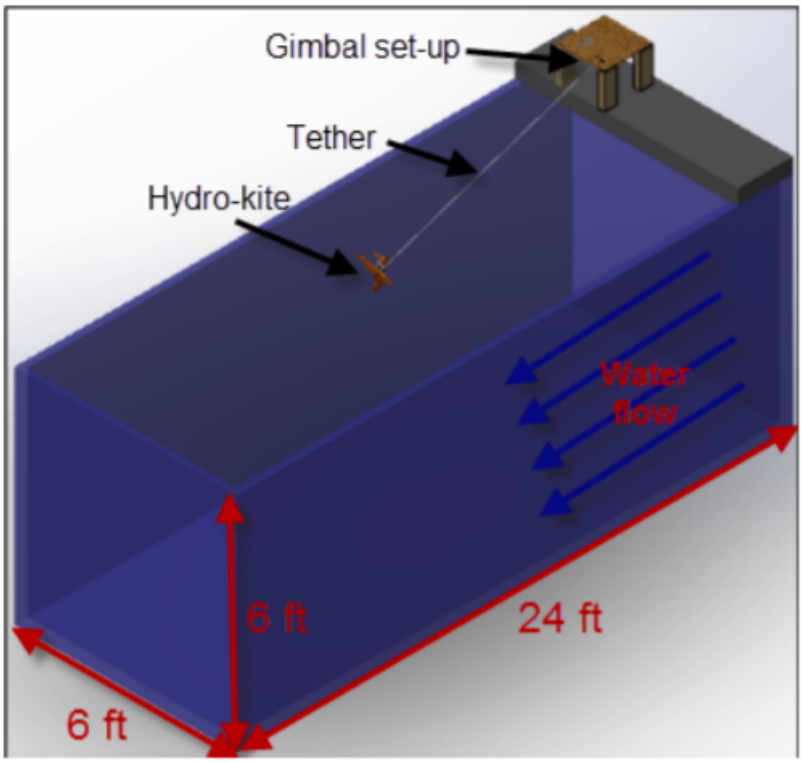

Figure 8: Complete CAD Model (Aye-Addo et al., 2014)

While the team was unable to test their model, they were able to produce a small-scale system and a theoretical power output was estimated. The team believed their work provided that the system "should work and produce clean electrical energy" (Aye-Addo et al., 2014).

Following the 2014 group, in 2015 graduate student Ryan Fredette researched tethered undersea kites being tested for power generation in his thesis paper. Once again, the focus of this research was on the feasibility of TUSK systems. A scale-model TUSK was designed and then tested in a water flume. These tests help collect data including the "azimuth and declination angles of the rigid tether as well as the power output of the generator on board the kite" (Fredette, 2015). Graphs were created from the data and relationships between velocities, kite

pitch angle, and power output were measured. Fredette also made note of areas of improvement for his work which noted a need for improved kite, turbine and data collection systems. The power output of this design was much less than originally predicted, mainly due to significant amounts of drag.

In 2017, an MQP group undertook the design and testing of a SUSK system. The team constructed a scale-model SUSK system including a "streamlined surface boat hull, an underwater wing, a dragging turbine assembly, and a carbon fiber tether attached to a stationary gimbal above the water surface" (Higgins et al., 2017). To obtain power estimates, dynamic simulations of the system were developed and the scale-model was tested. In Figure 9 the team's scale-model is shown.

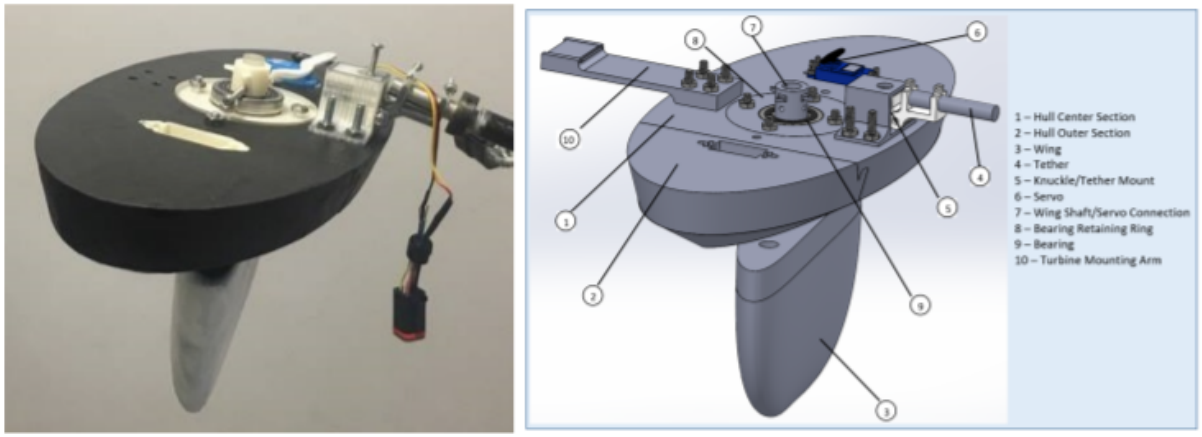

Figure 9: Previous MQP SUSK design and CAD rendering (Higgins et al., 2017)

The project demonstrated that the SUSK system is as good, and possibly better than, other tethered energy systems and has the potential to be better than stationary harvesting methods. The team had many suggestions for future teams, including to "experiment with different wing planform shapes, chord lengths, and spans study effects on system performance" (Higgins et al., 2017). Our project will build on the work done by this MQP team with modifications.

More recently, in 2021, Nicole Petilli redesigned a SUSK system improving the wing size and hull shape. She also performed "an analysis of the optimal aspect ratio for a half-chord [symmetric] wing" (N. Petilli, 2021). The optimal aspect ratio was calculated using the equations shown below:

$$L = \frac{1}{2} * \rho * V^2 * S * C_L \quad (1.4)$$

$$D = \frac{1}{2} * \rho * V^2 * S * C_D \quad (1.5)$$

$$S = c * b \quad (1.6)$$

$$C_L = \frac{2\pi}{1+1/AR} * (\alpha - \alpha_{zero\ lift}) \quad (1.7)$$

$$AR = b/c \quad (1.8)$$

$$C_D = C_{d0} + C_{di} + C_{dp} \quad (1.9)$$

$$C_{di} = C_L^2/(2\pi * AR * e) \quad (1.10)$$

$$C_{dp} = k * C_L^2 \quad (1.11)$$

Note: L = lift; D = drag; ρ = density of water; V = apparent velocity; S = surface area of the wing; C_L = coefficient of lift; C_D = coefficient of drag; c = chord length; b = length of wing; AR = aspect ratio; α = angle of attack [radians]; C_{d0} = parasitic drag; C_{di} = induced drag; C_{dp} = pressure drag; e = span efficiency; k = shape facture equal to slope of C_D v. C_L^2 curve; and (1+1/AR) is used to account for only one wingtip vortex. (N. Petilli, 2021).

Based on the above equations, Petilli plotted the max power and aspect ratio (at max power) by varying the chord length, from 0.01 to 2 m, for each angle of attack, -4 to 12 degrees. Figure 10 shows that the max power is produced when the aspect ratio is equal to 4.347.

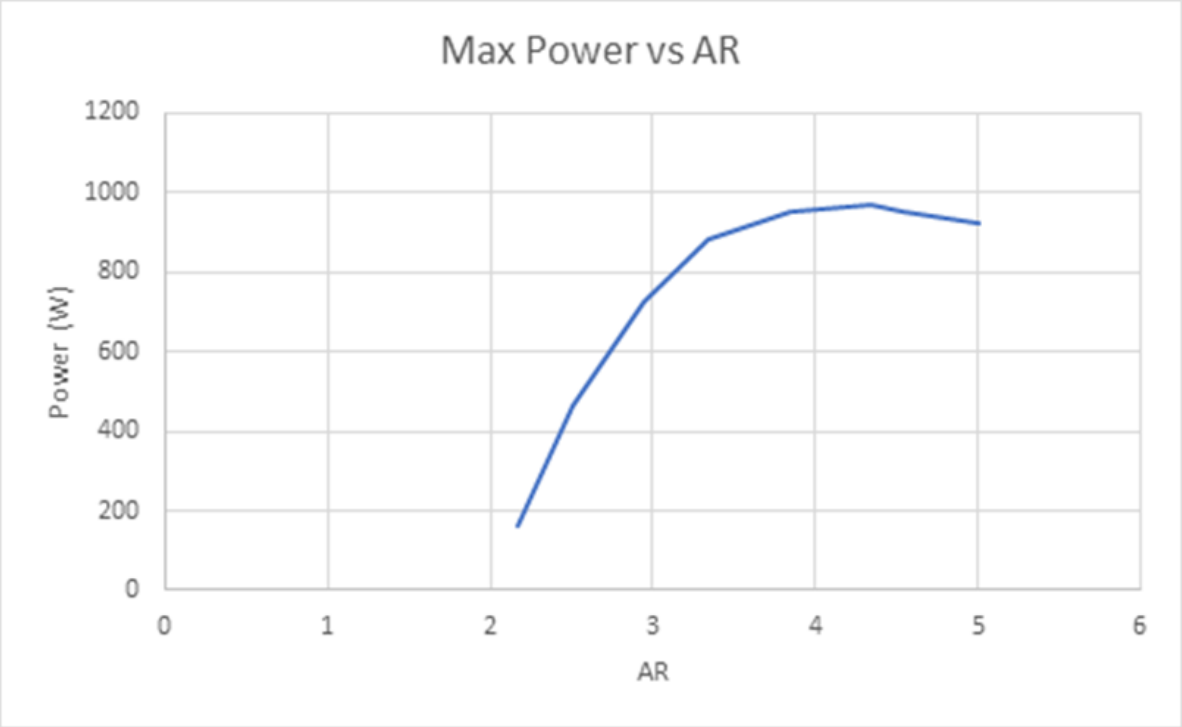

Figure 10: Maximum Power Produced as a Function of Kite Wing Aspect Ratio (N. Petilli, 2021)

The optimum aspect ratio is produced where power output is maximized due to the following equation.

$$P = \frac{2}{27} \cdot \rho \cdot V^3 \cdot A \cdot c_L \cdot \left(\frac{c_L}{c_D}\right)^2 \quad (1.12)$$

Note: P = power output from a cross-current kite; ρ = water density; V = current velocity; A = area; c_L = lift coefficient; c_D = drag coefficient. This finding holds much significance as we will implement this optimum aspect ratio in our iteration of the SUSK scale-model.

1.2 Project Goals

The following project goals were determined to further the studies on high-aspect ratio wings incorporated in tethered ocean energy systems as a renewable energy source.

- Redesign the previously developed WPI scale model SUSK system to include a higher aspect ratio (AR = 4) wing.
- Fabricate an improved scale model of SUSK with interchangeable wing, hull, and turbine arrangements.
- Experimentally reproduce the expected power output of SUSK.
    - Compare estimated power from scale model to larger designs of system.
- Determine further SUSK component improvements after initial testing.

1.3 Project Design Requirements, Constraints, and Other Considerations

The project had the following constraints.

Design Constraints:

- Project Budget
    - Limited to $250 per student, yielding a max budget of $1,250 for this project.
- Prototype Size
    - 3D Printing Limitations
        - LulzBot TAZ 6 Print Dimensions: 11" x 11" x 9.8"
        - Ultimaker 3 Extended Print Dimensions: 8.5" x 8.5" x 11.8"
        - Makerspace Hours, Print Time less than 15 Hours

Testing Constraints:

- WPI Recreation Center
    - Only able to perform pool testing during open swim hours.
- Creating SUSK system's electrical components to be water resistant for desired prototype depth upon testing in the pool.

The project had the following requirements.

Project Requirements:

- Experimentation of a higher aspect ratio wing.
- Prototype maneuverability in transportation among facilities.

1.4 Project Management

The project took place starting in A-term of 2021 and continued through C-term of 2022. The group is composed of five undergraduate students majoring in Aerospace Engineering, with one student double-majoring in Physics. The team members are Olivia Chiasson, Adrianne Curtis, Andrew Ventura Molina, Thomas Rau (AE/Physics double major), and Zachary Sotland. Preliminary tasks were completed in A-term followed by designing and fabricating an improved SUSK scale-model prototype in B-term. Finally, C-term testing was completed and conclusions were made. The physics modeling and equations of motion were composed through the course of B and C terms. Each week the team presented updates on their project to their advisors. A project review presentation was presented to advisors, in C-term, as well as Master's and PhD students who will be continuing the project research. Finally the team will present to the Aerospace Engineering Department on Project Presentation Day in D-term. Thomas will also present to the Physics Department.

As engineers we have ethical and professional responsibilities we must consider when conducting our research. We have a responsibility as engineers to adhere to the principles of sustainable development in order to protect the environment for future generations. Our project has a strong focus on renewable energy, so we are doing our part to uphold this responsibility. It is also our ethical responsibility to properly cite any previous research that influenced our project work. Technical contributions of each member is designated in the authorship table of the report, and is also reiterated here with additional detail.

The following table represents the work completed throughout the year.

Project Work	**Project Work Completed By**
System Design	ALL
System Modeling MATLAB	TR*
System Modeling SolidWorks	ZS
Parts List & Order Forms	ALL
3D Printing	TR, ZS
Hull Fabrication	OC, AVM
Wing Fabrication	ZS
Turbine Fabrication	AC, ZS

1.5 MQP Objectives, Methods and Standards

1. Determine the best design for the Hull, Wing, and Turbine of SUSK
    a. Using the past project research to determine the optimal shape for the hull and airfoil.
    b. Designing Turbine head casing, blade, and generator components.
2. 3D printing of the Wing and Turbine
    a. The wing was exported to SolidWorks from XFLR5, then printed to be assembled in 6 pieces.
    b. The turbine was also designed in SolidWorks in three parts, the turbine blades, the turbine casing, and the inlet and outlet flow nozzles. Then each will be printed out individually before connecting together with the generator to complete the turbine.
3. Shaping of Hull
    a. The styrofoam hull was cut out of large styrofoam disks and then shaped using surface planers. The inner structure was connected by an inner aluminum rod frame.
4. Controlling the Wing
    a. Using an Arduino, the wing was controlled to turn so that the boat is always moving with the wing having an optimal angle of attack.
5. Testing of the SUSK model
    a. The full model was tested in the WPI pool to assess power outputs and feasibility as a renewable energy alternative.
6. Reevaluated SUSK system designs and implemented desired changes to benefit performance.

1.6 MQP Tasks and Timetable

The timeline was decided based around constraints within the design, building, testing stages. A-Term mainly consisted of deciding our designs for the hull, wing, and turbine. This is where the evolution of the physics modeling met a practical design. The assembly of SUSK began in B-Term, with modifications continuing into C-Term. B-Term was also a time where the majority of the 3D printing took place due to the need in manufacturing specific pieces. The equations of motion and a mechanics review for the physics modeling took place throughout the first two terms. C-Term mostly consisted of pool testing and analysis. A few iterations of SUSK were made after initial testing to render better results. Table 1 denotes the Gantt Chart that visually represents this timeline throughout the course of the school year.

Table 1: Gantt Chart of Project

a) Timeline for A-Term

	A-Term						
	Week 1 (8/25 - 9/2)	Week 2 (9/6 - 9/9)	Week 3 (9/13 - 9/17)	Week 4 (9/20 - 9/24)	Week 5 (9/27 - 10/1)	Week 6 (10/4 - 10/8)	Week 7 (10/11 - 10/15)
Preliminary Tasks							
Preliminary Designs							
Finalize Designs							
Materials and Parts List							
Literature Review							
Design							
XFLR5 Design							
SolidWorks Blades and Wing							
SolidWorks Turbine							
Order Parts List							
3D Print of Wing, Blades, Turbine							
Build							
Hull Fabrication							
Turbine , Generator, and Wing Fabrication							
First Full Assembly							
2nd Iteration Assembly							
Test							
Testing in Pool							
Testing Analysis							
Physics Modeling							
Mechanics Review							
Equations of Motion							
Iterations of System							

b) Timeline for B-Term

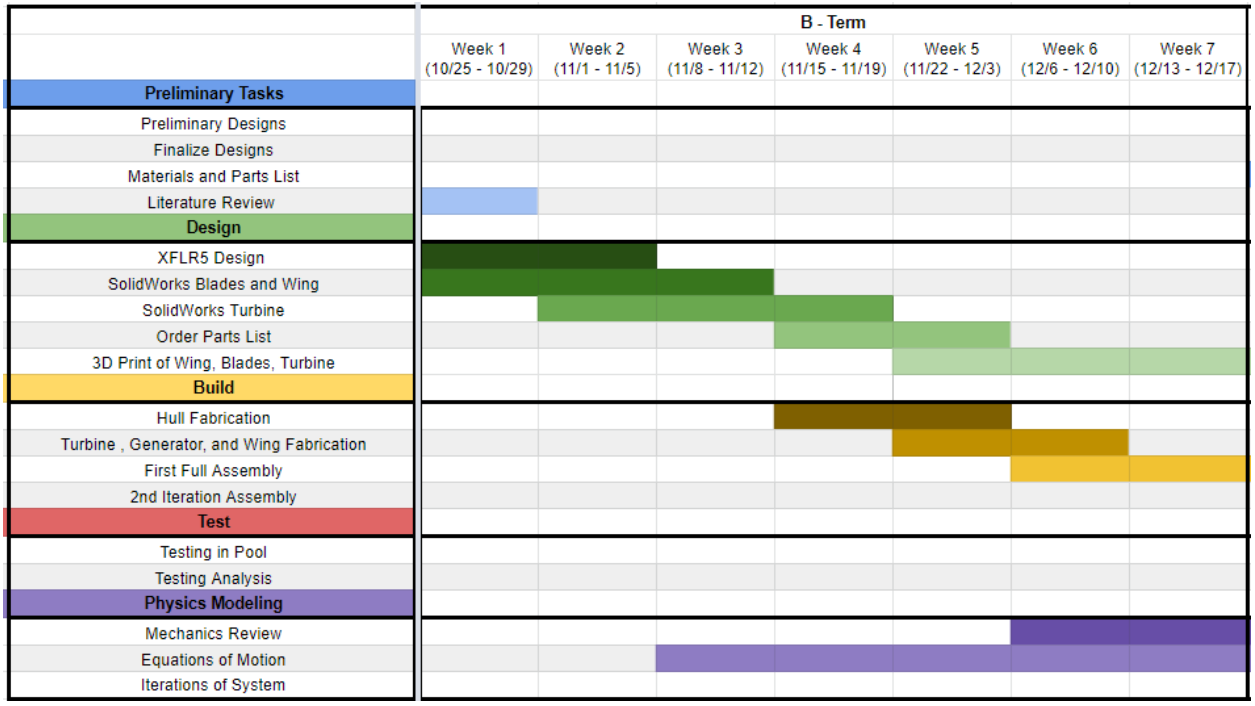

c) Timeline for C-Term

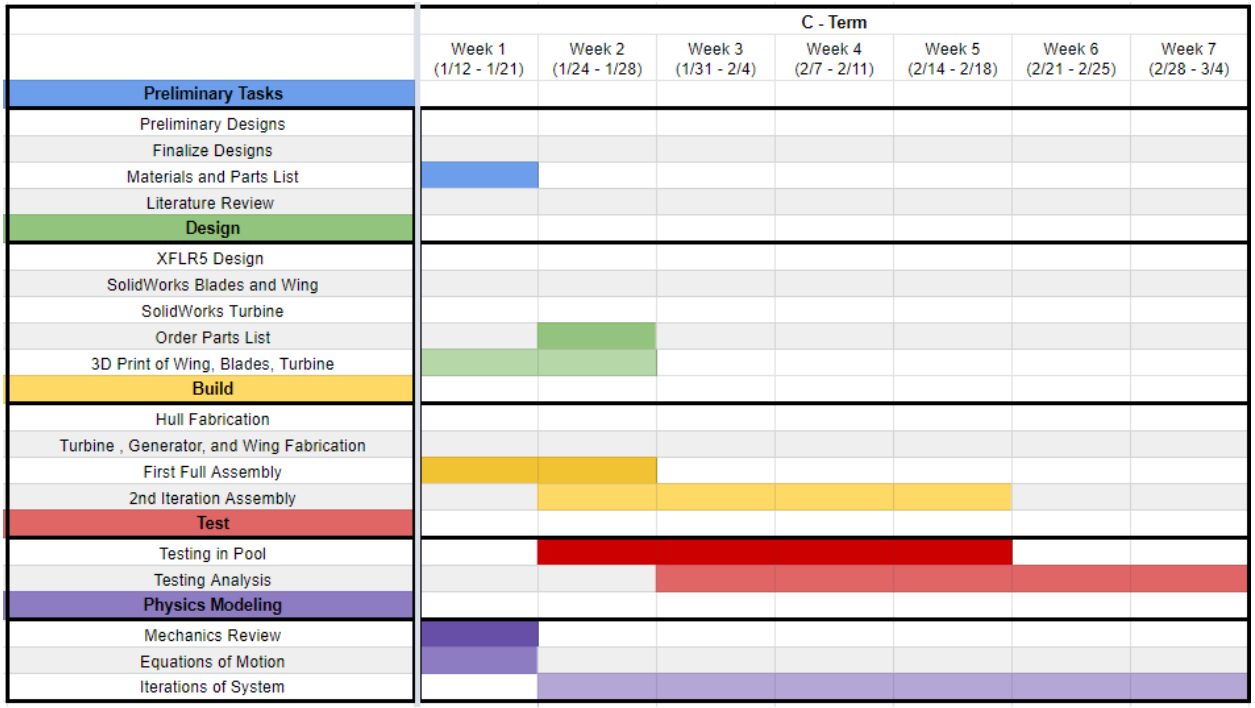

2 SUSK Scale-Model Subsystems

2.1 Final Scale Model SUSK Design

The new WPI SUSK scale model that was developed in this project has four major components as shown in Figure 10. Comparing Figure 8 from Section 1 with Figure 11 shows the dramatic changes that have been made to the WPI SUSK scale model design during the course of our project. The design, analysis, and testing of the new SUSK scale model are described in subsequent sections of this report. The SUSK model consists of a catamaran style hull (1), a higher 4:1 aspect ratio wing (2), a Wells turbine within a converging nozzle (3), and a servo control box for mounting the tether and electrical components (4).

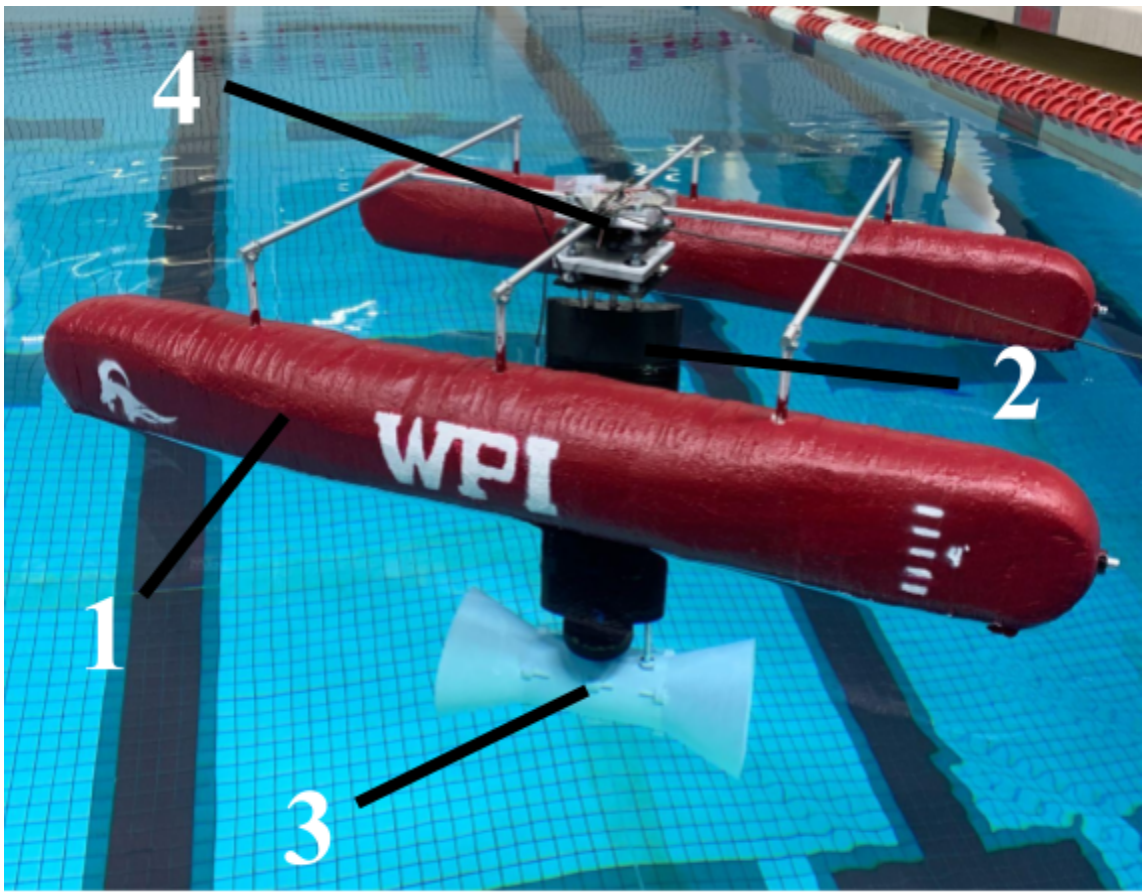

Figure 11: Final Scale Model of SUSK System

The various components of the new WPI SUSK system use the materials listed below:

- Hull
    - 8 inch diameter styrofoam disks
    - ½ inch aluminum rods
    - ½ inch bore locks
    - ½ inch 90 angle locks
    - Flex seal
    - Acrylic paint
- Wing
    - 3D printed PLA wing pieces
    - ½ inch bore locks
    - Flex seal
- Turbine Head
    - 3D printed PLA nozzle, Wells Turbine blades, and cylindrical pieces
    - Flex seal
    - 5 lb weights
    - ½ inch bore locks
- Servo Control Box
    - ⅜ lag bolts, nuts, and washers
    - 3D printed 6x6 inch PLA holster plates
    - 6x6 inch aluminum plates
    - Two arduino 35 kg 270 degree servo's
    - Two ½ inch aluminum rods
- Generator
    - 3D printed PLA casing and turbine blades
    - Pacific Sky Power DC Motor
    - 26 gauge silicone wire
    - Flex seal
    - Tile caulk

2.2 Wing Design

2.2.1 Airfoil Design

The 2017 MQP completed a thorough analysis to find the optimal airfoil shape for the SUSK model (Higgins et al, 2017). Standard airfoils have a trailing and leading edge that have significant differences, notably the leading edge being rounded and the trailing edge ending in a point. For this project, a half chord symmetric airfoil was chosen so the boat can move forwards and backwards without having to rotate the wing 180 degrees each time it changes direction, as shown in Figure 12. Analysis was completed by the 2017 MQP team through XFLR5 on twelve different airfoil shapes with thicknesses varying from 10% to 20% of the chord length, and cambers varying from 2% to 5% of the chord length. Simulations were also performed on XFLR5 using Reynolds numbers of 150000, 250000, and 350000, with an angle of attack from 0° to 18°. The results from these simulations proved that half chord symmetric airfoils would be a viable option so extra energy was not used to turn the wing during operation (Higgins et al, 2017).

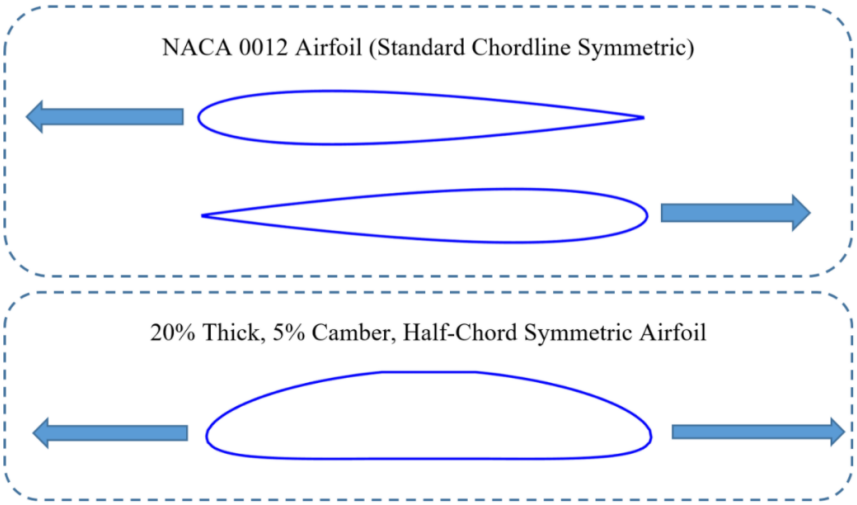

Figure 12: Comparison Between Chordline Symmetric and Half Chord Symmetric Airfoil

A force analysis on the airfoils was then used to determine which out of the twelve candidates was best. The airfoil with 20% thickness and 5% camber was determined to have the best lift to drag ratio, which can be seen in XFLR5 in Figure 13, as well as in Table 2 (Higgins et al, 2017).

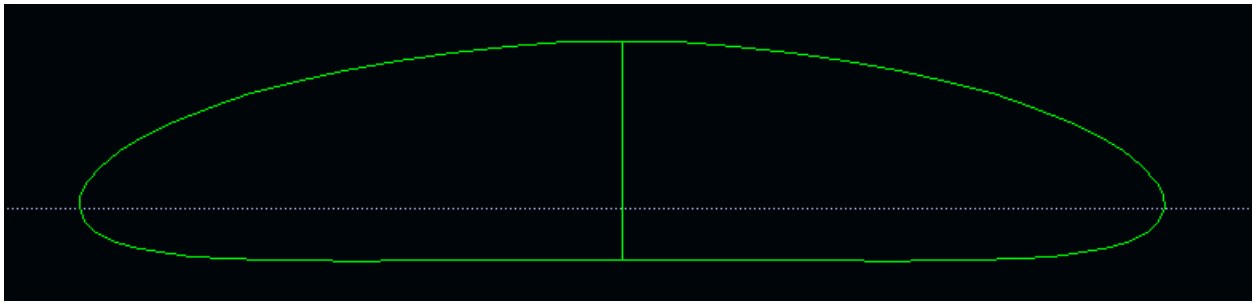

Figure 13: Final Airfoil Design of 20% Thickness and 5% Camber Displayed in XFLR5

Table 2: Data from XFLR5 simulations demonstrating the force (in Newtons) produced based on different cambers and thicknesses at the maximum lift to drag ratio (Higgins et al, 2017)

		Camber			
		2%	3%	4%	5%
Thickness	10%	22.447	19.066	22.481	24.546
	15%	21.337	24.934	27.555	29.690
	20%	27.947	31.295	32.065	35.834

The optimal airfoil was 3D printed as well as one with decreased thickness to 10% and one with decreased camber to 2%. Wind tunnel testing was then performed with a Reynolds number of 350000 and angle of attack from 0° to 18°. This testing confirmed the 20% thickness and 5% camber as the optimal airfoil after plotting airfoil data against XFLR5 data (Higgins et al, 2017).

2.2.2 3D Wing Planform Shape Design

The optimal airfoil design was created in XFLR5 by modifying the thickness and camber directly, and then Excel was used to reflect the airfoil over the half chord to generate symmetry. This work was done by the 2017 MQP team and then repeated by our team, to be able to later 3D print a model wing. From previous work, this optimal design was found through simulations in XFLR5 and wind tunnel testing to find an airfoil with the highest lift to drag ratio (Higgins et al, 2017). Next, the design was modified to fit an optimal aspect ratio. In previous research, A SUSK model was created and went through simulations to find the aspect ratio where the maximum power would be produced at a fixed angle of attack. The optimal ratio was determined to be 4.347:1 (Petilli, 2021). This led us to creating our model around a 4:1 aspect ratio to generate the maximum power for our SUSK system. Using equation 2.1 our chord length was determined, using a total wing span length of 3 ft or 36 inches.

$$c = \frac{b}{AR} \tag{2.1}$$

$$c = \frac{36}{4} = 9\ [in]$$

Note: c = chord length, b = wing span, AR = aspect ratio

The coordinates were then scaled to a chord length of nine inches and loaded into SolidWorks. A hole was cut out in the center of the wing for a metal rod to connect the turbine to the hull. This is so the wing can rotate while the boat is turning to gain maximum lift, while the turbine remains stationary to achieve maximum inflow velocity. There is also extra space next to the rod in the middle of the wing for wires to connect to the generator if needed. Since the 3D printer we have access to only has a height of 11.8”, and the 3D printing lab has maximum

operating hours, the maximum span length of the wing we were able to print was 6 inches. This led us to putting in pegs on one side of the airfoil and a socket on the other side so that the wing would be able to be printed in parts and the individual wing section pieces would fit together. The final design is shown in Figures 14 -16.

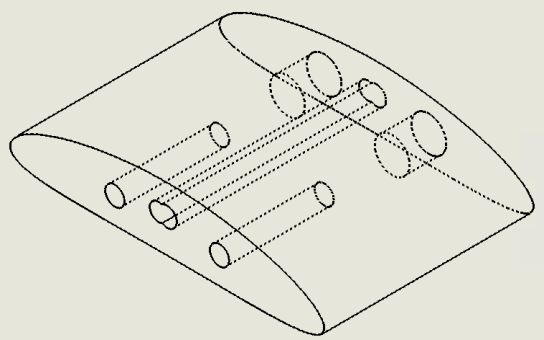

(a) Isometric view of top wing section

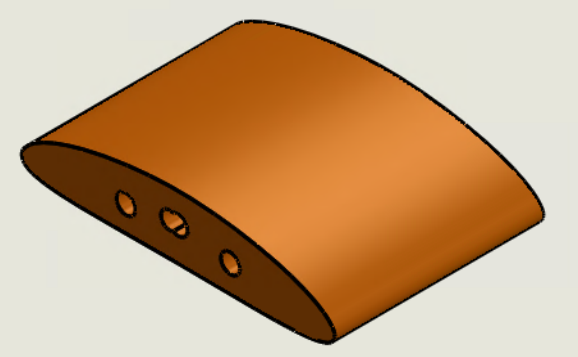

(b) Colorized view of top wing section

Figure 14: Final Drawings of Top Wing Section in SolidWorks

In order to achieve a 4:1 desired aspect ratio with a 36 inch wing span, six 6 inch long wing sections were required. The top piece is different as it has one side with sockets and the other side is modified to fit rods in the top so the servo can turn the wing, shown in figure 14. Additionally, the bottom piece is also slightly different from the middle sections, as it only has one side with pegs and the other side is flat to be placed right above the turbine, shown in Figure 16.

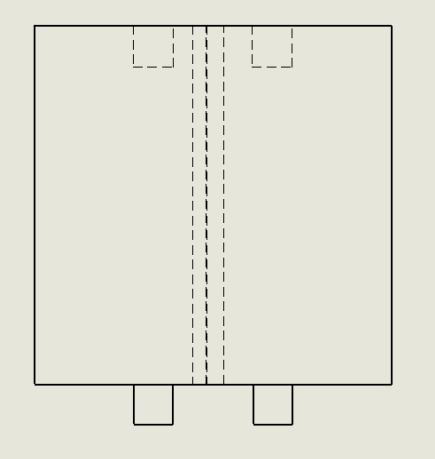

(a) Top view of wing section

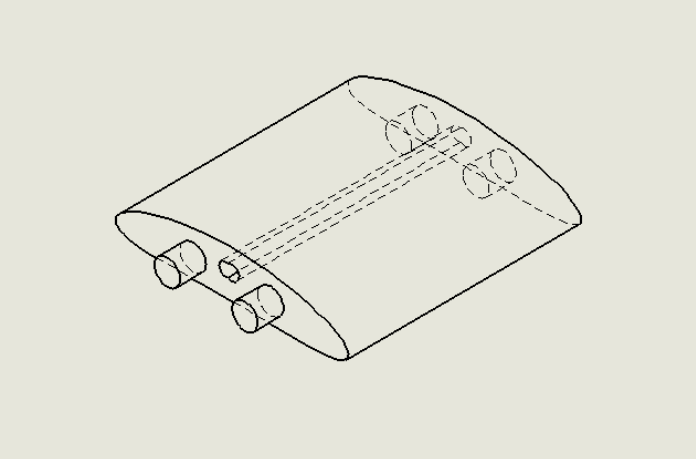

(b) Isometric view of wing section

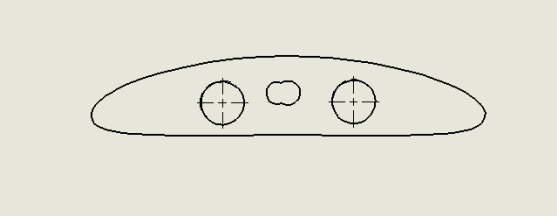

(c) Front view of wing section

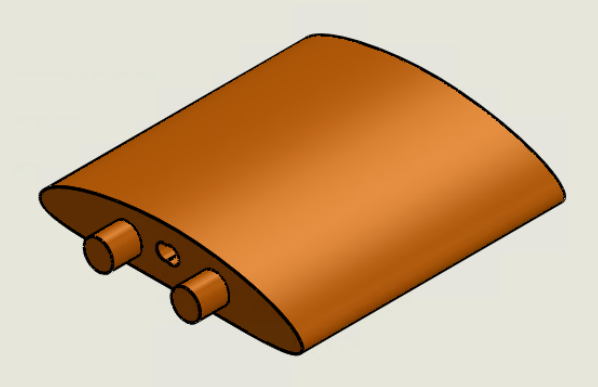

(d) Colorized view of wing section

Figure 15: Final Drawings of Middle Wing Sections in SolidWorks

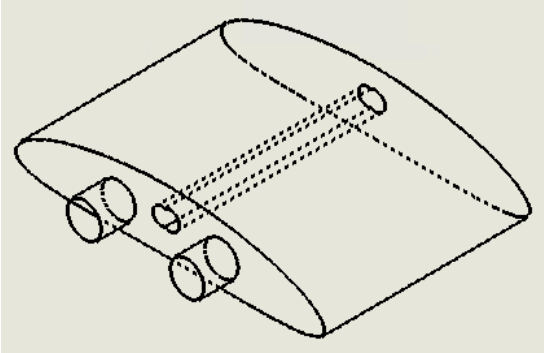

(a) Isometric view of bottom wing section

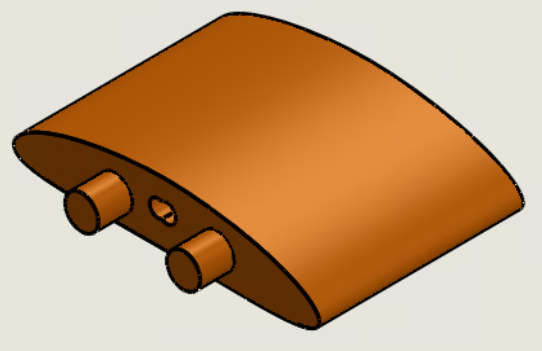

(b) Colorized view of bottom wing section

Figure 16: Final Drawings of Bottom Wing Section in SolidWorks

The 3D prints were completed through WPI's innovation studio 3D printing lab. Due to the size of the prints, each section took approximately 13-14 hours to print.

2.2.3 Wing Assembly

The wing pieces were 3D printed as pieces so they would be able to fit together and be used as a single wing. This was done due to the available 3D printers not being able to print a single four foot wing in one print. We were also limited to a time constraint as the 3D prints were only able to be printed between the hours of 10 AM and 1AM for a max of 15 hours. This resulted in us printing the pieces at six inches long instead of a max of 11 inches from the printer constraint. The individual wing pieces and two wing pieces put together are shown in figure 17.

Figure 17: Individual Wing Pieces

The wing pieces fit together so snugly that it is near impossible to pull them apart. They were then coated with Flex Seal. This was so the wing would be waterproof and not absorb water

since we used PLA as a 3D print material. The full wing assembly is shown in figure 18. And with Flex Seal and paint in figure 19.

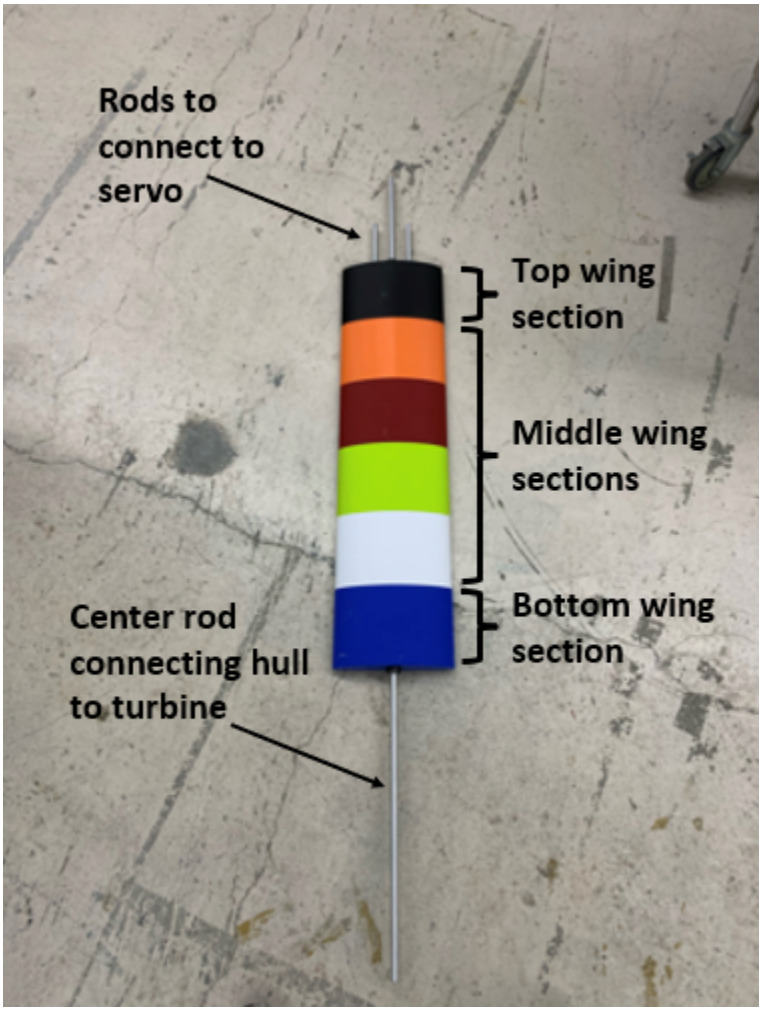

Figure 18: Full Wing Assembly

Figure 19: Wing assembly with paint and Flex Seal

The wing assembly will be sandwiched to the inner aluminum rod via ½ inch bore locks. The locks on the rod will have a slight spacing which will allow the wing to turn.

2.3 Hull Design

2.3.1 Hull Design

In the 2017 iteration of this project (Higgins et al., 2017), the MQP team considered hull designs of a rounded flat plate (horizontal), a half ellipsoid, and a catamaran. Higgins and his group's goals when designing the hull was to minimize the drag in the direction of travel. This drag would have caused stress on the tether and slowed the boat down. Another factor in their design was the stability of the boat. Each hull candidate was tested in a water tunnel where pros and cons of each design was noted. The half ellipsoid was the least stable, and it was hard to mount the other components of the boat. The rounded flat plate had the least perpendicular drag but also had a low buoyant range, while the catamaran style was determined to be the most stable of the design candidates. In the end, the group decided on the plate style hull which can be seen in Figure 16 in Section 1.1.7. In Figure 20 is another view of the hull from the 2017 MQP group.

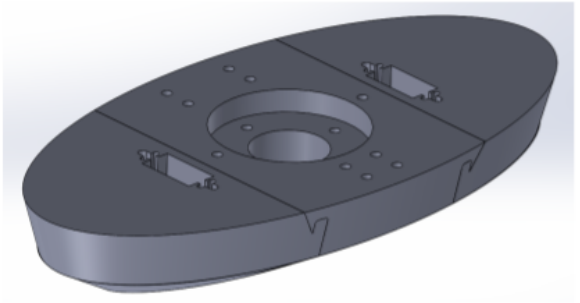

Figure 20: CAD Rendering of Flat Plate Hull Design (Higgins et al., 2017)

The final construction of the hull had the rest of the mechanisms attached to the top, with the wing on the bottom side, under the water surface. The hull needed to be treated with sealant and waterproof servos and wires were used.

Based on the previous project work on TUSK and SUSK systems our team initially decided our hull should be a catamaran shape. The catamaran shape is considered a multihull design which is very stable and provides multiple mounting surfaces for the wing and turbine. A basic initial design of our hull and entire system is shown in Figure 21.

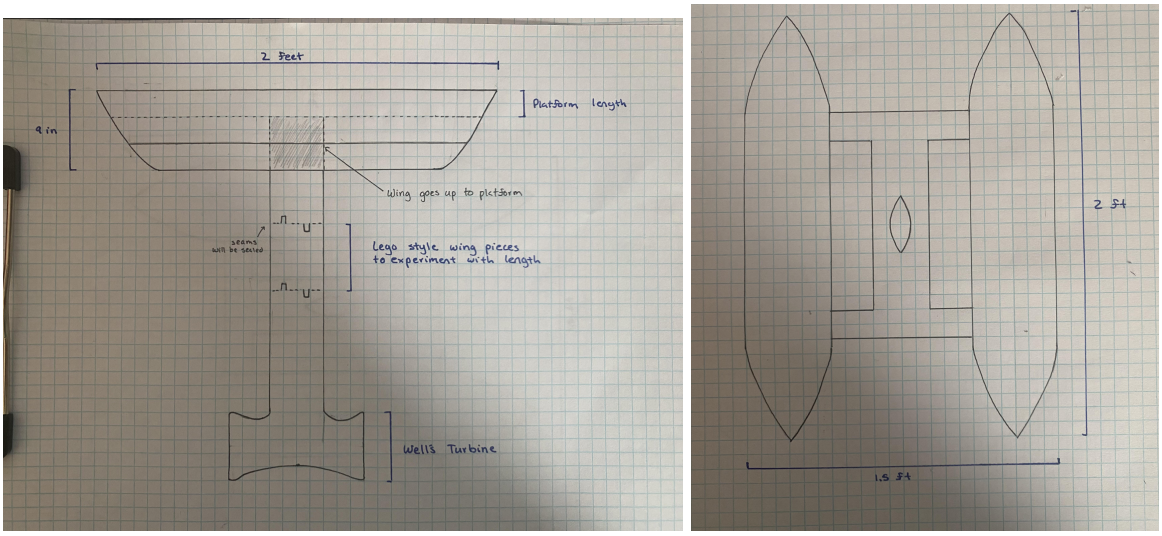

Figure 21: Initial System Design Showcasing Hull

The team decided the design should have a length of 5 feet and a width of 3 feet in between each hull shape. Rods would be used to keep each hull shape connected as well as provide a platform for the control box, and a place to attach the tether, and wing.

2.3.2 Hull Fabrication

Metal rods were used to connect the two hulls to provide a platform for the servo control box. We cut the rods to our desired lengths. For each hull, the rods were roughly around 5 feet and the rods attaching the hulls together were 3 feet each. Then we drilled holes the diameter of the aluminum rods through the styrofoam and then placed them on the rods. Figure 22 shows members of our team drilling holes through the center of the styrofoam disks.

Figure 22: Team Members Prepping the Styrofoam Disks

A styrofoam half-sphere was attached to the end of each rod to create a rounded hull shape at the bow and stern. The rods were also connected using joints so that the control box would be far above water level as well as allowing the length between the hulls to be adjustable. Figure 23 shows the fully connected hull with the aluminum rods attaching each side.

Figure 23: Completed Hull After Assembly

We planned to add one rod diagonally across the top of the rods to increase stability but our pool tests confirmed that this was not necessary. After the pieces of styrofoam were added to the frame, we sanded each hull to make a more streamlined hull shape to reduce drag. Figure 24 shows our team members shaping the hull using an orbital sander, a saw to cut off bigger pieces, and sandpaper to smooth out tiny details.

Figure 24: Sanding of the Hull

After the shaping was completed, we used Flex Seal to cover the styrofoam so that water would not be absorbed during testing. Figure 25 shows one of our team members applying the coatings of Flex Seal to the hull.

Figure 25: Flex Seal Application to the Hull

The servo box rests on the middle aluminum rod of the hull's frame. Details on the servo box can be found in Chapter 2.4 and 2.5. Two perpendicular rods are fastened to the outside rods for a fixed connection. These joints are detachable to allow for easy transportation of the SUSK system between facilities upon testing. We also ran a rod through the center of the servo box to attach the wing pieces, weights, and the turbine nozzle to. Figure 26 shows the frame completely put together.

Figure 26: Servo Box Connection onto Hull

After the completion of the hull assembly, we then made the model look more aesthetically pleasing.

2.3.3 Paint and Waterproofing

Once the flex seal layers dried and the hull was evenly coated, we decided to paint and add decals to the hulls. The hull was painted a WPI red (Pantone 187c) and 3 decals were added: the WPI letters, a symbol of the goat, and finally several tallies which represent the height of the hull. The metal rod within is 4 inches from the middle to the bottom. To do the stencils, we sketched them out on cardboard and then used a razor to cut out the pieces. When the stencils were ready we spray painted over them using a white. The figures below show the testing and application of the decals to the hull.

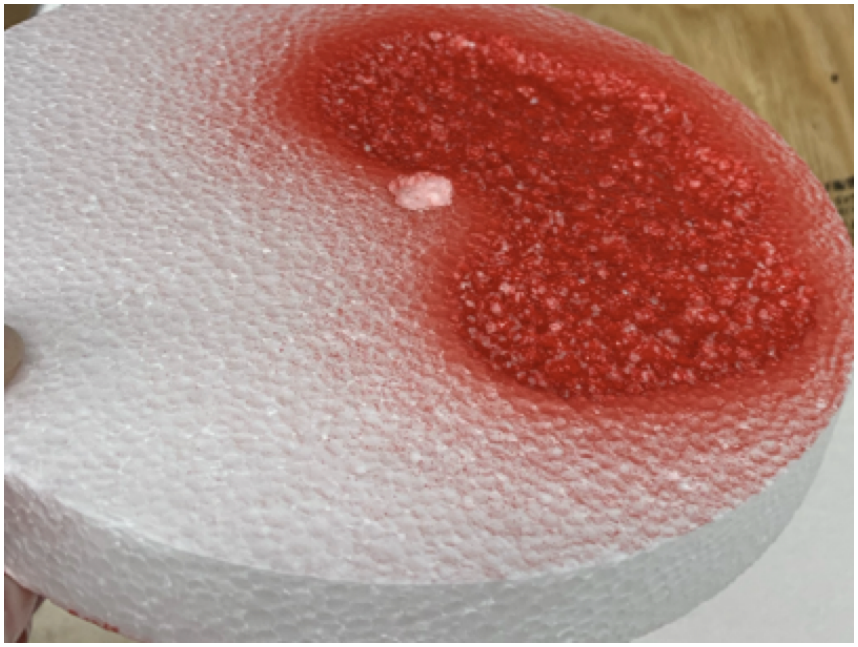

Figure 27: Failed Spray Paint Attempt

An issue we ran into during the painting process of the hull was finding a paint that would not damage the styrofoam. Figure 27 shows a piece of styrofoam that got deteriorated after being spray painted. From there we needed to search for alternative paint that would not damage the hulls. After some research, we discovered that the only paint possible to use on the

styrofoam is acrylic. Spray paint or any paints containing latex or enamel will degrade styrofoam during its application. Although the hulls were covered in flex seal, we decided to play it safe and use a regular acrylic paint and only use spray paint for the decals.

Figure 28: Testing of the Goat Stencil

Figure 29: Application of the Decals

Figure 30: Hulls after Spray Painting

After assembly, waterproofing, and painting the hull portion was complete.

2.4 Turbine Design

2.4.1 Turbine Type Selection

The inclusion of a water turbine will allow the SUSK system to generate power using current flow over rotating turbine blades. As the flow of water passes over the turbine blades, it produces rotational energy, which is then translated into the generator to produce electricity.

For this project, the Well's Turbine was selected due to its ability to spin in the same direction regardless of the direction of the flow. This turbine consists of symmetric airfoil blades, which are able to convert aerodynamic forces into mechanical energy. These turbines are often used in oscillating water column (OWC) technologies, which is a relatively new form of renewable energy generation. OWC systems utilize ocean waves to push air through a nozzle, which causes the Well's Turbine to spin. When the wave recedes, a vacuum suction is created in the chamber and the air is pulled back down, but due to the symmetric airfoil shape of the turbine's blades it continues spinning in one direction. This reduces loss of energy which occurs with an unsymmetric turbine needing to slow, stop, and change direction to accommodate a differing flow direction.

The incidence angle for this turbine needs to be less than 15 degrees, preferably the smaller the better, to keep the blades from stalling, which reduces the performance of the turbine overall (Cambuli & Ghisu, 2017). The only exception is when the turbine is initially set into motion, but even at this time the incidence angle cannot exceed 90 degrees.

2.4.2 New Turbine Design

The properties of the Well's Turbine discussed above were applied to a previous design to improve its performance. The design constructed in 2016 included a turbine which was fixed on the downstream side of the SUSK system. When a current flowed over the turbine blades, it was allowed to swivel back and forth in free-rotation in order to ensure water was flowing across the system at all times. An extra NACA 0015 airfoil was added to the back of the turbine to assist in these rotations.

To simplify this design, the Well's Turbine was chosen for the 2021-2022 project to eliminate the need for the turbine to swivel to face the current. This newer design is also beneficial in that it minimizes the need for extra parts, such as the airfoil that was acting as a rudder behind the turbine itself.

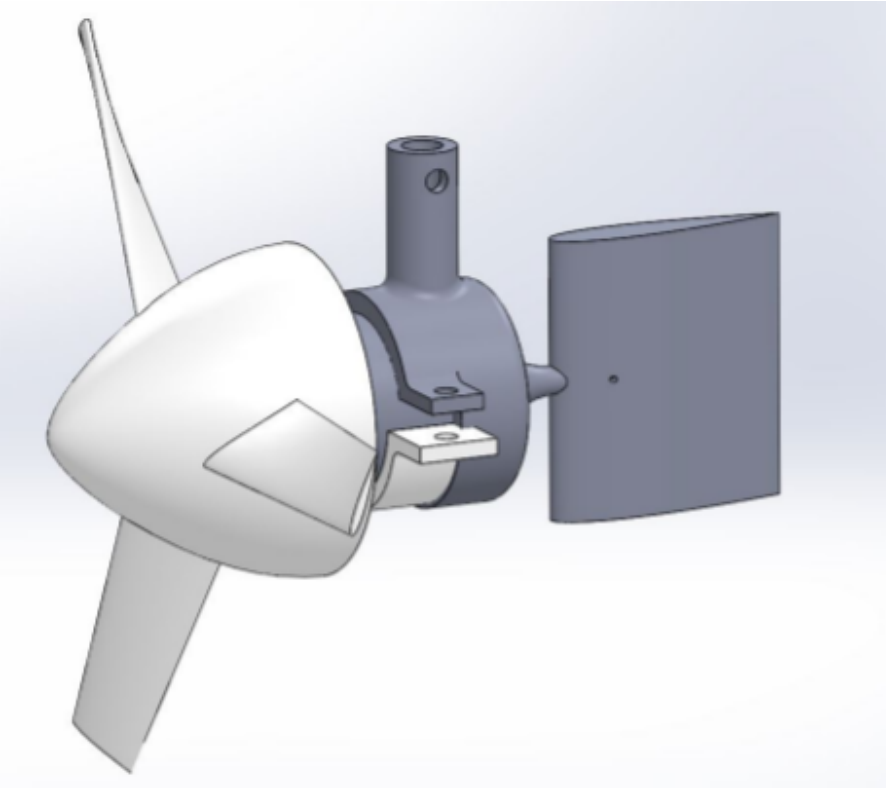

Figure 31: CAD Model of 2017 SUSK MQP (Higgins et al., 2017)

This year's iteration of the SUSK turbine includes five NACA 0006 symmetric airfoil blades around a conical nose cone. In total, the full system is divided into three separate parts. The first being the turbine head itself, the centerpiece being the generator housing, and the final piece being a conical nose end piece of equal shape to the turbine head. Each piece was designed using CAD software and printed on the 3D printers located in the Innovation Labs on WPI's campus.

Five blades were selected for the turbine because a typical Well's Turbine will consist of five or six blades depending on the application. Although for the purpose of this project, six caused too much crowding on the turbine head itself. Densely populated blades are a culprit for inducing more drag, which was an important aspect we were trying to minimize in this project.

The generator housing was constructed to fit the generator within the smaller opening, which would face the turbine head. The wires would then be organized neatly within the rest of the cylinder with a shaft connected up to the vertical wing. A hole for the metal shaft was not constructed into the solidworks design because it was more efficient to gauge where these holes would be located after the physical piece was printed, as opposed to making a mathematical approximation. It also allowed for more flexibility to change the location of the connection to the nozzle as the entire system was assembled together.

Finally, the conical end cap is identical to the turbine head on the opposite side of the cylinder, although with a lack of turbine blades. This was created so the turbine system itself is more aerodynamic and encourages flow across its surface.

Instead of a custom-made turbine, there were also options that were considered as alternatives, one being the utilization of the WaterLily Turbine. Marketed by the WaterLily company, this turbine is advertised as an alternative renewable energy source that is able to output 15W, which would have been suitable for the prototype of this project. A Waterlily

turbine was ordered late in 2021 B-term, however overseas shipping issues delayed delivery of the turbine prior to the project end. As a result, the team pursued the custom-made turbine option described earlier.

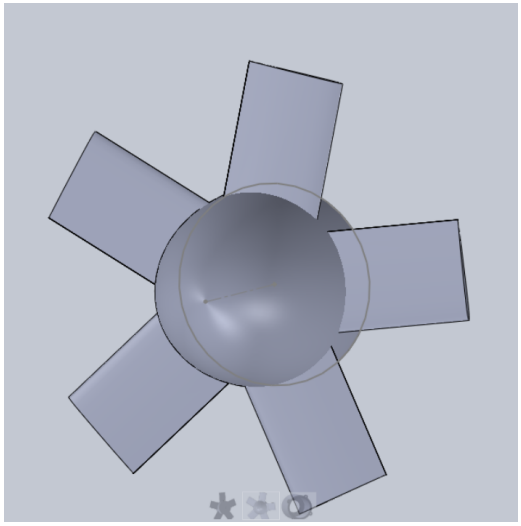

Figure 32: Turbine Head

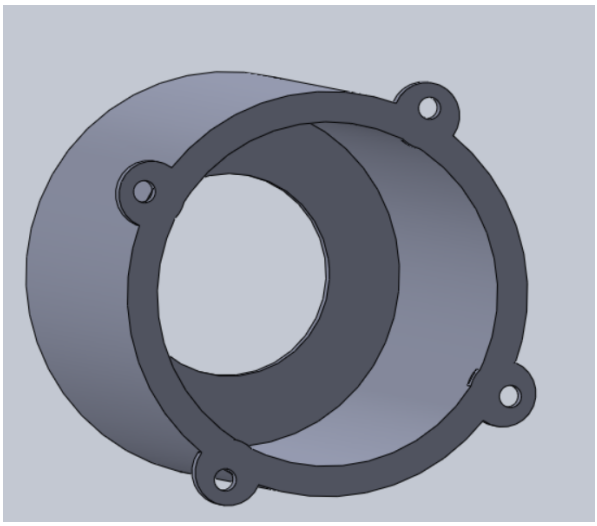

Figure 33: Generator Housing

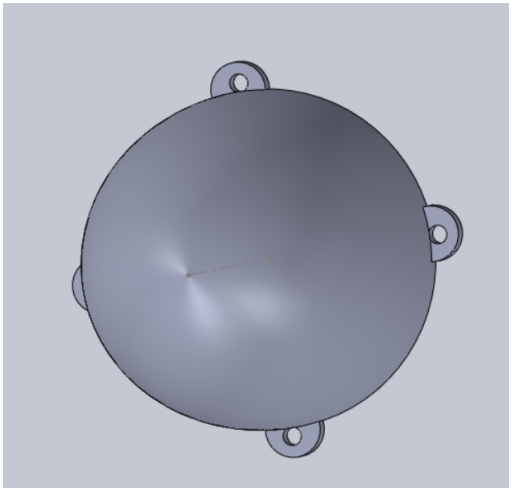

Figure 34: Conical End Cap

2.4.3 SUSK Scale Model Generator

The generator that was used in this project was a smaller model that was approximately 2 inches in diameter. It consisted of a cylindrical shape with the body being about ¾ of an inch and a shaft being one inch long. The shaft was fixed inside the small 0.13 inch diameter hole in the turbine head, so when water flows across the blades, it would cause the shaft to spin and produce electricity within the motor.

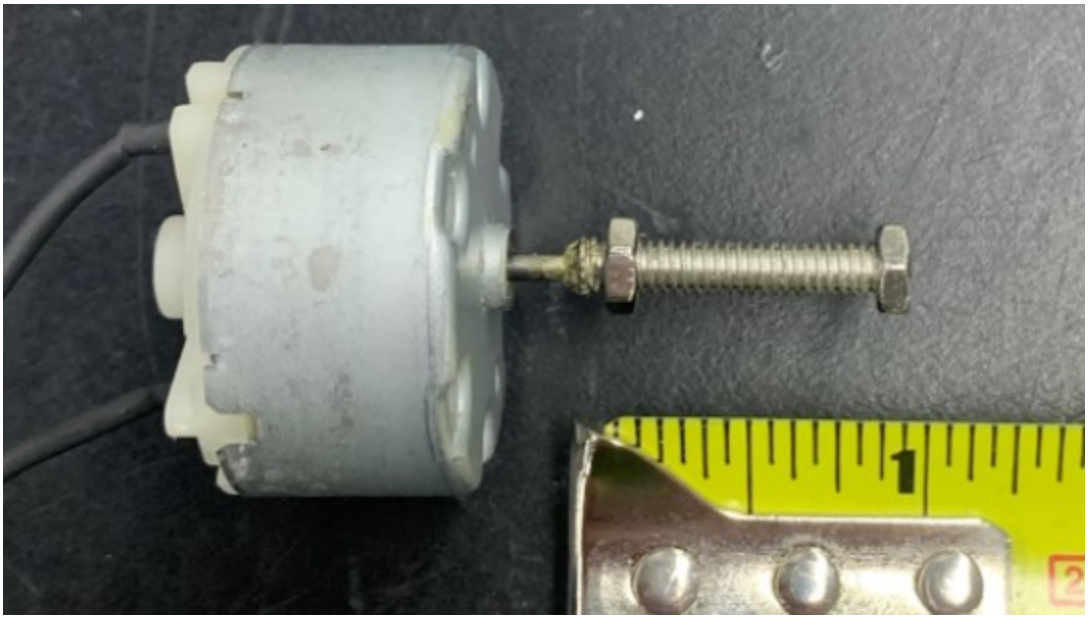

Figure 35: DC Generator

The generator shown in figure 30 was also used during the 2016 MQP project. To improve the efficiency of the design, other generators on the market could also be considered. As discussed in the section above, the generator that came with the WaterLily turbine would have also been a viable choice for this project. Waterproof turbines that exist on the market could have also been effective alternatives, and lessens the risk of breaking a generator that is not meant to withstand contact to water.

2.4.4 Turbine Nozzle Design

To increase the SUSK system power output, the turbine was placed at the throat of a newly designed turbine nozzle. This increases output power which varies with water velocity cubed, shown in equation 2.2.

$$P = CP * \rho V_o^3 A_o \quad (2.2)$$

Where CP is a turbine power coefficient and V_o is the velocity of water at the turbine rotor and A_o is the turbine rotor area.

A 2:1 ratio of inflow diameter (Di = 10 in) to outflow diameter (Do = 5 in) was used yielding a 4:1 area ratio. From mass conservation, this increases the velocity of the water entering the turbine, shown in equation 2.3.

$$V_o = V_i * \frac{A_i}{A_o} \quad (2.3)$$

Using a 2 ft/s current velocity, the speed of the flow into the turbine will be increased as shown.

$$V_o = \frac{\pi(5)^2(2)}{\pi(2.5)^2} = 8 \text{ ft/s}$$

By using the converging turbine nozzle, the turbine power output will then increase by a factor of 64 since the water velocity increases by a factor of 4 (and power scales with velocity cubed). This increase in power output shows that adding a turbine nozzle should increase the SUSK system viability as a renewable energy system.

The nozzle was designed to be able to be 3D printed using available 3D printers. This led us to design under a few constraints, mostly impacting the size of the nozzle able to be printed. We decided on a 10 inch inflow diameter since the printers we had access to had 11 inch beds.

Also, the nozzle is 6 inches long due to the time the print took, and since the 3D printers have active hours, we were only able to print a 6 inch long nozzle.

The nozzle end pieces are the same, but there is a center piece to enclose the generator and turbine underwater. This centerpiece will be printed in two pieces to be long enough to fit the entire size of the wing on top of it. All of these will be connected by 4 screws on the outside of the configuration. Additionally, the centerpiece will have a hole put into the side to allow for a connection between the turbine, nozzle, and wing. These final designs are shown in figures 36 and 37.

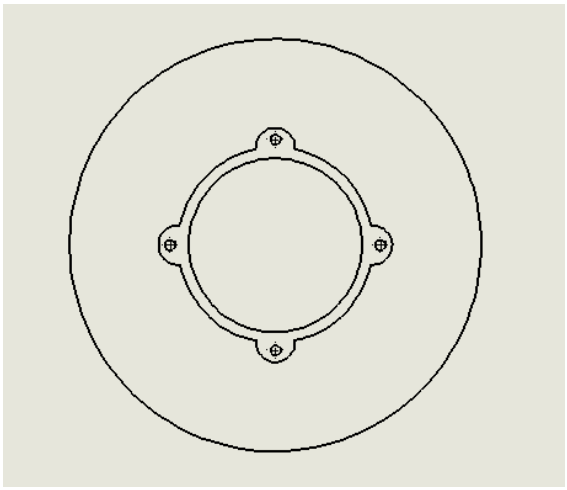

(a) Front view of turbine nozzle

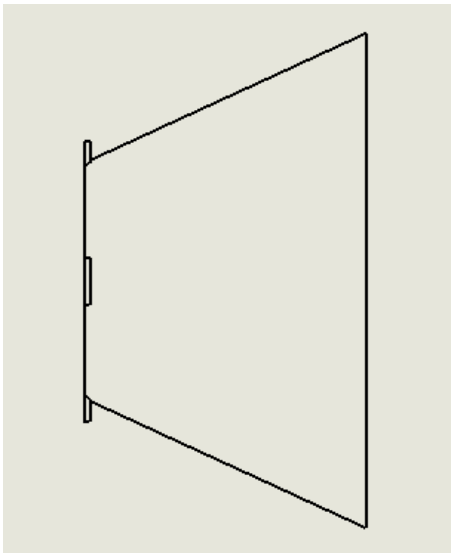

(b) Side view of turbine nozzle

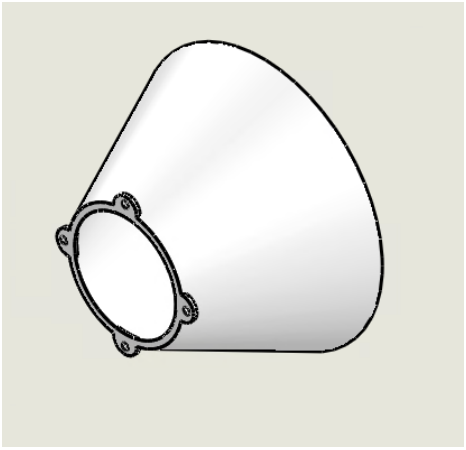

(c) Colorized isometric view of turbine nozzle

Figure 36: Final drawings of turbine nozzle in Solidworks

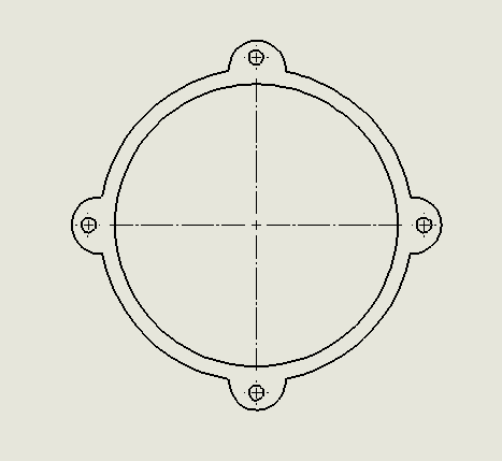

(a) Front view of center nozzle piece

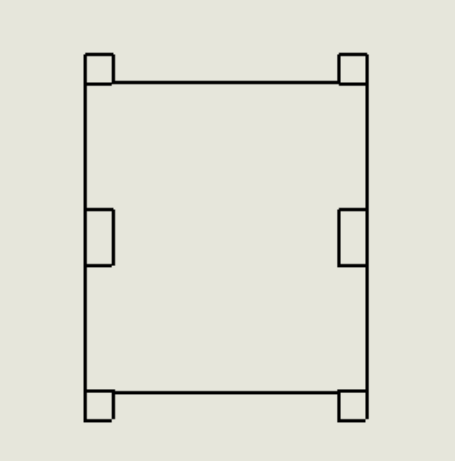

(b) Side view of center nozzle piece

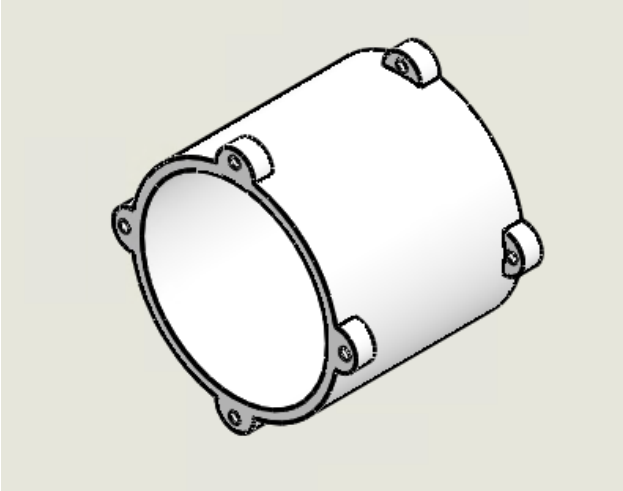

(c) Colorized isometric view of center nozzle piece

Figure 37: Final drawings of center nozzle piece in Solidworks

2.4.5 Turbine and Nozzle Assembly

For the assembly of the turbine, 3D printed parts were the main material we used. As seen in Figure 38, the turbine shaft is connected to the generator through a spray foam, while the body of the generator is housed in a centerpiece. This centerpiece is then connected to the end of the turbine assembly through spray foam bonding the two pieces. This end piece is used to increase aerodynamics of the flow through the turbine.

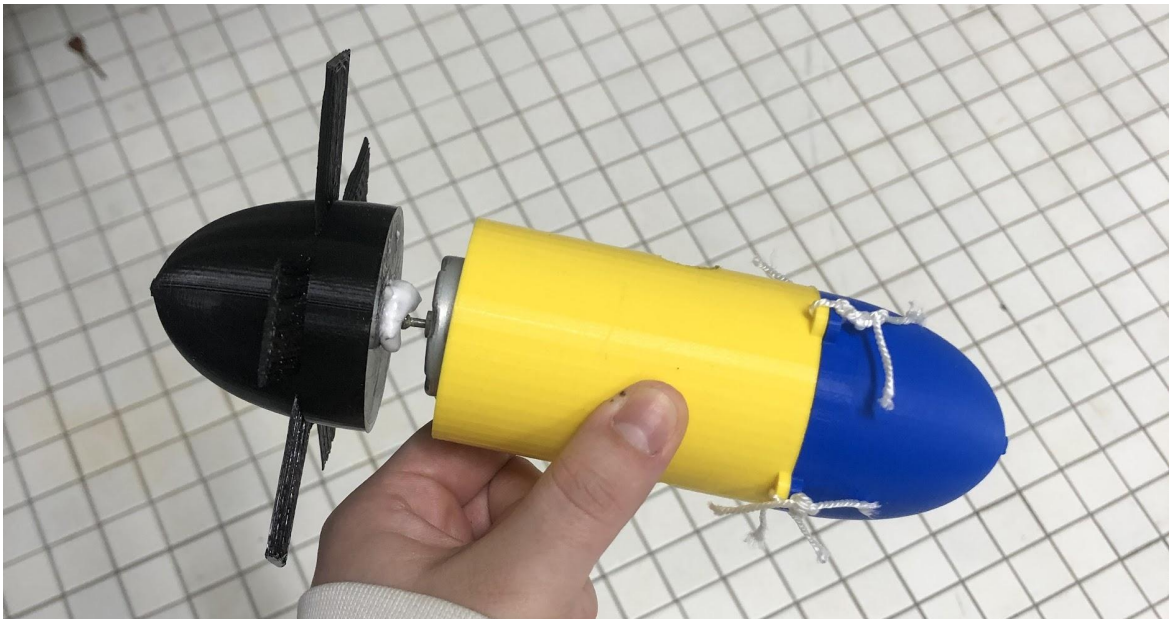

Figure 38: SUSK Turbine Assembly

The nozzle was also mostly assembled with 3D printed parts. To connect the four sections, screws and nuts are used at each of the corners. Flex seal was then added after the assembly was put together to ensure no water would seep into the cracks of the 3D printed parts. This is seen in Figure 39 and 40.

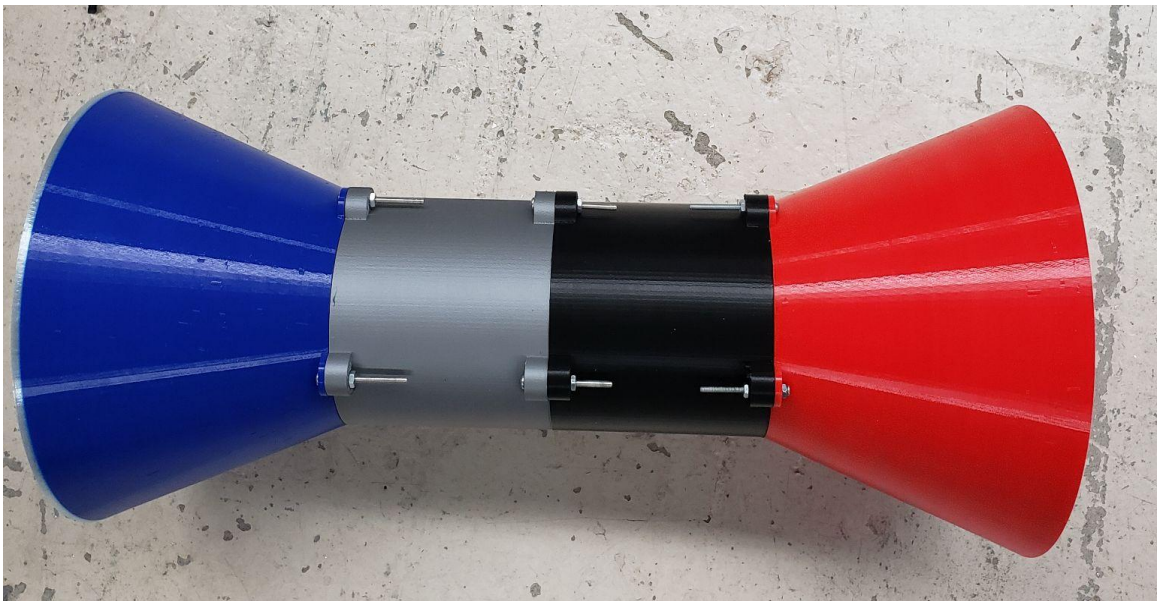

Figure 39: SUSK nozzle assembly without paint

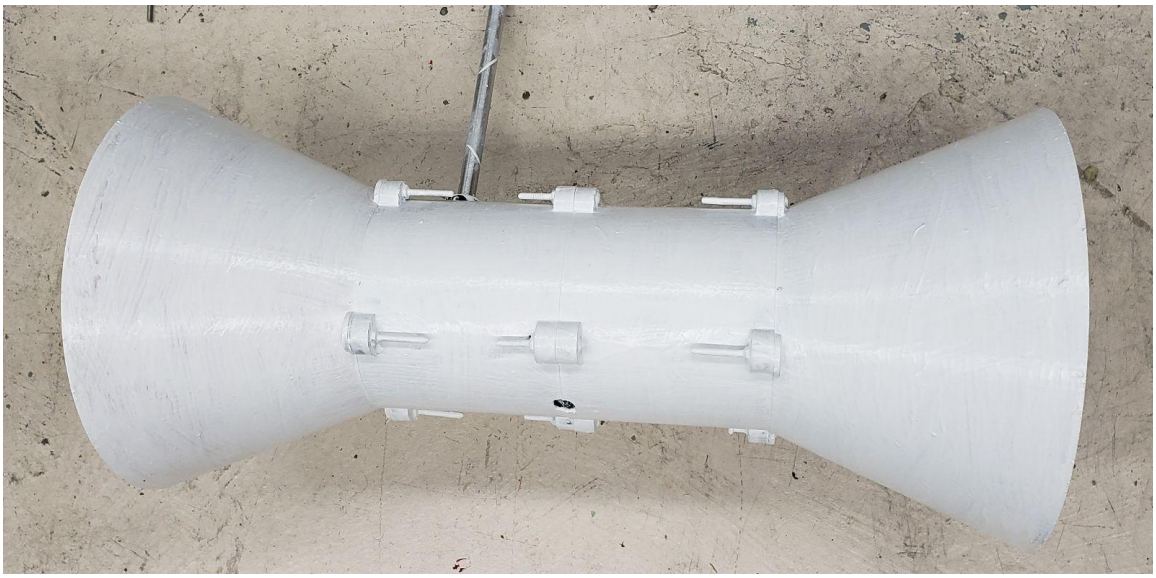

Figure 40: Nozzle assembly with white Flex Seal

Then the turbine was inserted into the nozzle as seen in Figure 41. Figure 42 also displays a secondary turbine with the same 3D printed components.

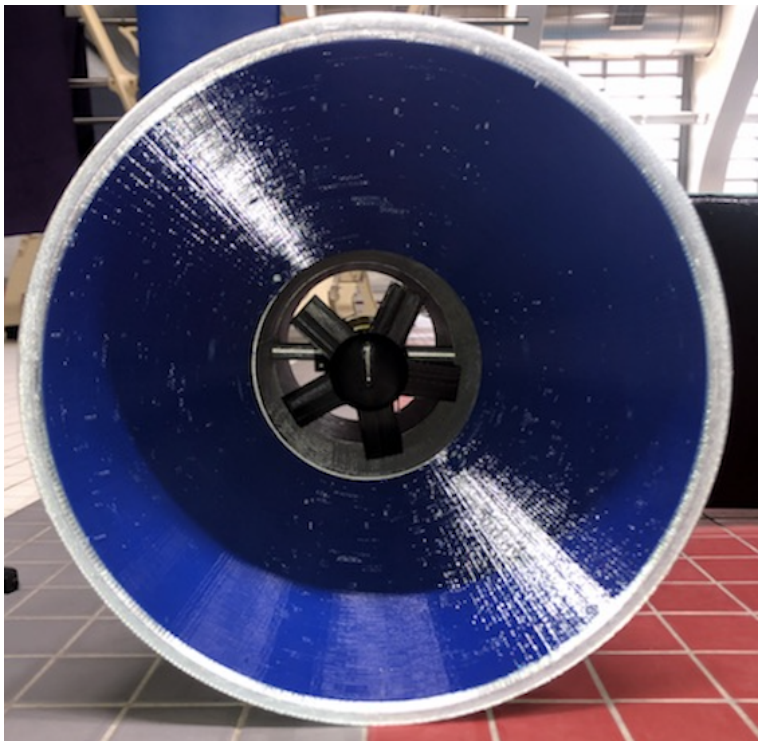

Figure 41: Turbine inside of nozzle assembly

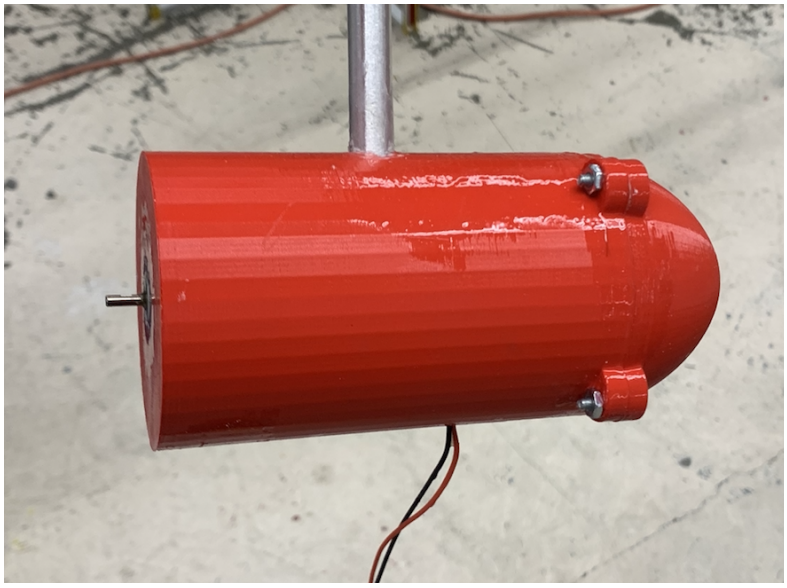

Figure 42: Alternative Generator Assembly

2.5 SUSK Control Systems

2.5.1 Servo Control Box

The SUSK servo control box consists of a layering of molding plates fitted for two arduino servos along with aluminum plating for added strength. This control box is crucial as it bears the loads of the torques on SUSK throughout its arcing motion. This component needs to be as fixed as possible due to this. The following CAD image below depicts the servo cutouts on the 6x6 inch plate. Two servos are connected to adjoining rods that are fitted into the wing on SUSK. This allows a pitching angle of the wing of about 20 degrees in both directions.

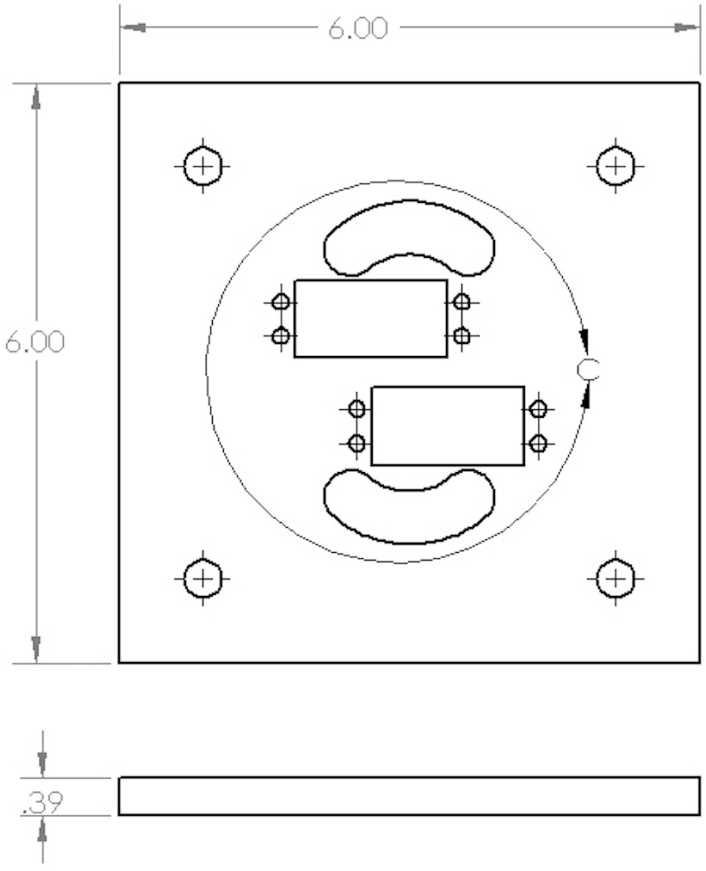

Figure 43: CAD Servo Molding Plate

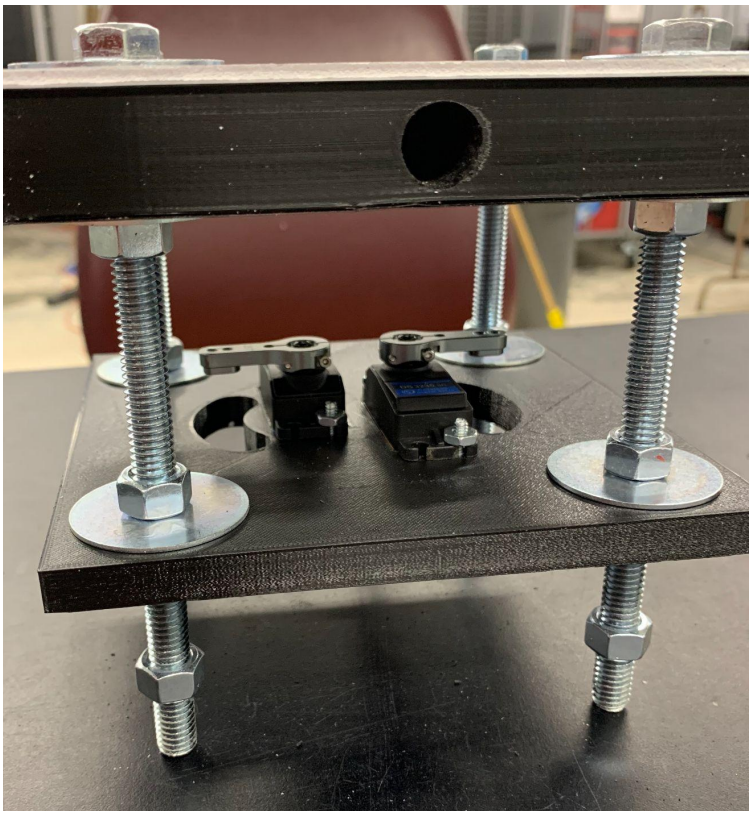

Figure 44: Servo Box Build Up

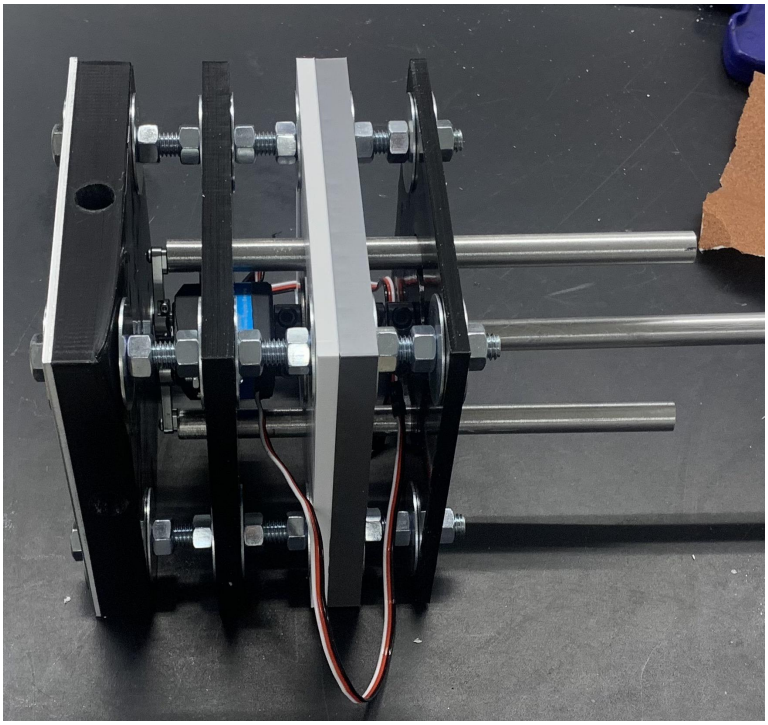

Figure 45: Servo Box Final Build Up

The servo box was built on the premise of layering these components. The two ½ aluminum rods that are connected onto the servo that control the pitch angle; these are non weight bearing. The center aluminum rod however is bound to the torques of the lowered wing and turbine assembly. Therefore to fix this joint as much as possible, ½ bore locks were used to sandwich the middle rod within its layers. Using the hex nuts on each of the layers along with the bore locks, we were able to sandwich the rod tightly without having any issues. After fabrication it turned out that if there were to be any problems to arise on this component, the torques on the rod would likely bend the rod itself, rather decouple this fixed joint. One iteration to the component due to failure is depicted below. After our first pool test, the PLA 1 inch plate at the top of the control box had snapped. Due to the forces on the stern and bow or pitching of SUSK. We then had reinforced this top 3D printed plate with a higher saturation infill and an additional aluminum plate. The Servo Box for all three testing was not wired to the carbon fiber tether, we note later on that this tether should be mounted and wired on the top of this servo box.

Figure 46: Servo Box on SUSK

3 Analysis of SUSK Scale-Model

3.1 Preliminary Calculations

3.1.1 Draft Calculations

Calculating the draft (submerged height of hull) of the designed SUSK model before initial float tests ensures that the boat will not sink and gives us an estimate on how much of the hull will be out of the water. To do this we must use a force balance between the weight of the SUSK system and the buoyancy shown in equation 3.1.

$$W_{SUSK} = Buoyancy \tag{3.1}$$

Then splitting the system into parts to make the weight calculation easier, using W for weight, V for volume, ρ for density, r for radius, and L for length.

$$W_{SUSK} = (m_{Hull} + m_{Wing} + m_{Turbine} + m_{Rods} + m_{Servo})g \tag{3.2}$$

$$m = V\,\rho \tag{3.3}$$

$$V = \pi r^2 L \tag{3.4}$$

For the hull calculations, using values for a 4 inch radius cylinder that is 5 feet long, with density of styrofoam that is 0.001120 lbs/in^3.

$$V_{Hull} = \pi(4)^2(5)(12) = 3015.93\ in^2$$

$$m_{Hull} = (3015.93)\,(0.001120) = 3.38\ lbs$$

Then calculating for both sides of the catamaran hull and adding ½ lb for flex seal.

$$m_{Hull} = 3.378(2) + \frac{1}{2} = 7.26\ lbs$$

Next, for the wing calculation each wing section weighed approximately the same amount, at 290.82 g or 0.64115 lbs, with an additional ½ lb added for paint and flex seal.

$$m_{Wing} = 0.64115(6) + \frac{1}{2} = 4.35\ lbs$$

For the turbine, the generator and turbine weight was estimated at 2.7 lbs while the nozzle weighed 2.3 lbs. The servo box was estimated as it was placed in the assembly before being able to be weighed and was put at 7.5 lbs.

For the aluminum rods calculation we used the total length of rods used, 204 inches, and the density of aluminum at 0.097544 lbs/in^3.

$$V_{Rods} = \pi(0.25)^2(204) = 40.055\ in^2$$

$$m_{Rods} = 40.055(0.097544) = 3.91\ lbs$$

Then calculating the right hand side of equation 3.1 for buoyancy we must use the submerged volume of the system with the density of water.

$$Buoyancy = V_{Submerged}\,\rho_{H_2O}\,g \tag{3.5}$$

$$V_{Submerged} = V_{Turbine} + V_{Wing} + V_{Part\ of\ hull} \tag{3.6}$$

Plugging back into equation 3.1 to solve for the submerged volume of the system.

$$(m_{Hull} + m_{Wing} + m_{Turbine} + m_{Rods} + m_{Servo})g = V_{Submerged}\,\rho_{H_2O}\,g \tag{3.7}$$

$$7.26 + 4.35 + 5 + 3.91 + 7.5 = V_{Submerged}(0.036019)$$

Then rearranging equation 3.6 to get

$$V_{Part\ of\ hull} = V_{Submerged} - V_{Turbine} - V_{Wing}$$

Using the Matlab script in Appendix F to find wing volume, and using Solidworks to find the turbine volume

$$V_{Part\ of\ hull} = 777.92 - 122.09 - 467.28 = 188.55 \text{ in}^3$$

Then calculating draft, **δ** from the submerged hull volume using equation 3.8, but using half of the submerged volume to represent one half of the catamaran hull. This equation is assuming a cylindrical hull shape with radius r (Volume of a partially filled cylinder, n.d.).

$$V_{Part\ of\ hull} = Lr^2 cos^{-1}\left(\frac{r-\delta}{r}\right) - (r - \delta)\sqrt{2r\delta - \delta^2} \tag{3.8}$$

$$94.275 = (60)(4)^2 cos^{-1}\left(\frac{4-\delta}{4}\right) - (4 - \delta)\sqrt{2(4)\delta - \delta^2}$$

To solve for draft a Matlab script was run, shown in appendix E with the value found for submerged volume, and the known values for the radius and length of the hull. This resulted in a draft of 0.57 inches.

3.1.2 Stability Calculations

To determine if the system is stable, the center of mass and volume were found. For the system to be stable, the center of mass must be below the center of buoyancy, shown in equation 3.9 with the origin at the top of the servo box and z negative downward.

$$CM_{SUSK} < CB_{SUSK} \tag{3.9}$$

To determine the center of mass, a Solidworks model was created with masses of the individual components inputted, shown in figure 47 and 48.

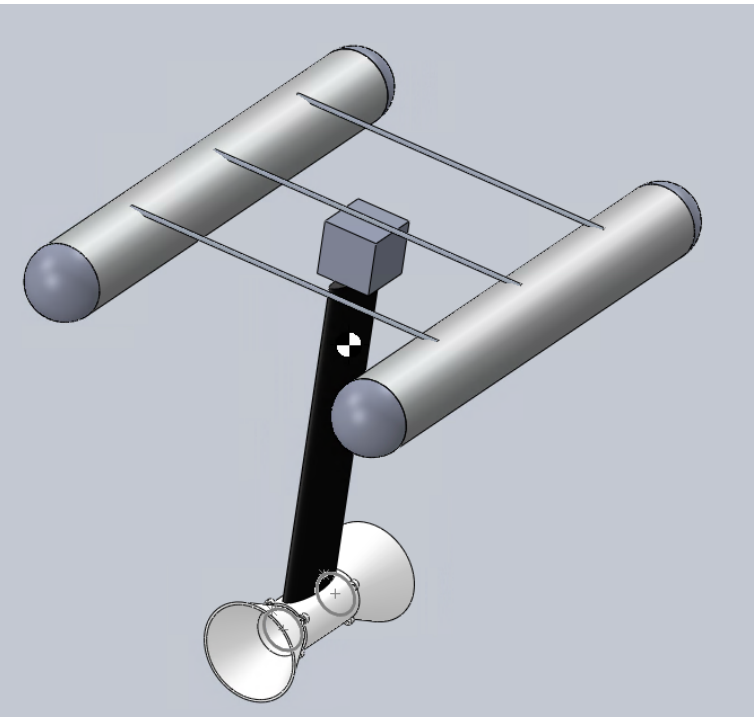

Figure 47: Isometric view of SUSK system with center of mass displayed

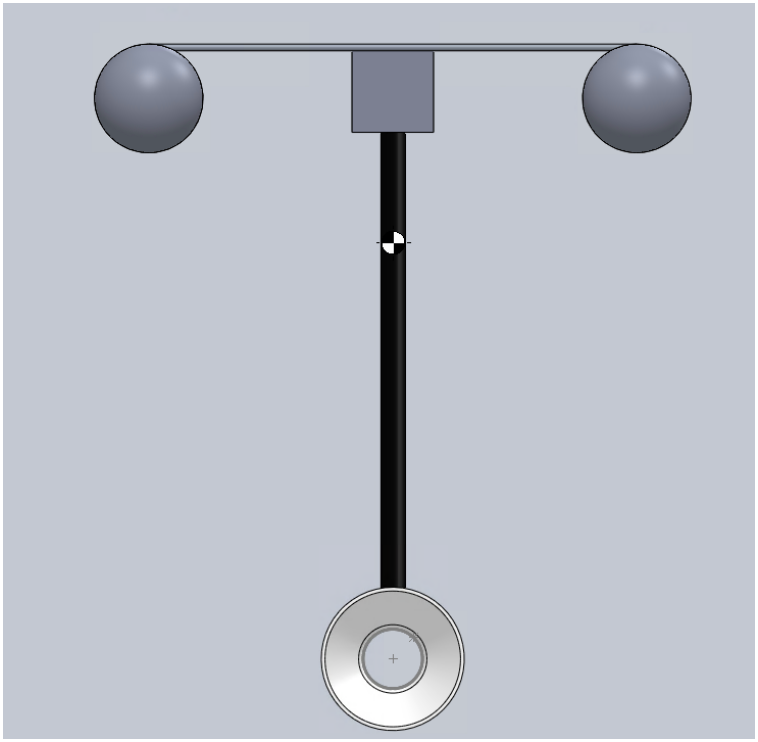

Figure 48: Front view of SUSK system with center of mass displayed

Through Solidworks, the center of mass was determined to be at 14.12 inches below the top of the hull.

To determine the center of buoyancy of the system, all components submerged must have an assumed density of water. This was also done on Solidworks by changing the density of the parts to that of water, and then finding the point at which the weight of the displaced water weighed the same as the SUSK system, shown below in Figure 49.

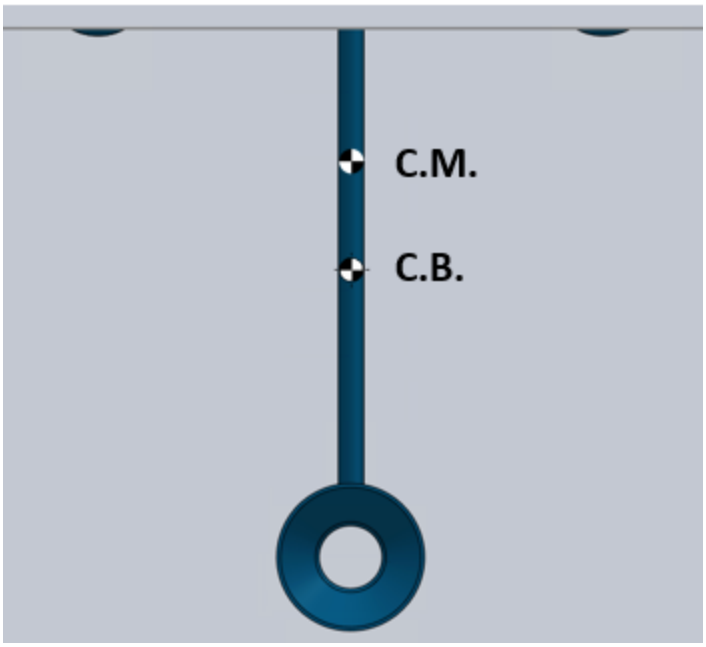

Figure 49: Front view of SUSK with center of buoyancy and center of mass displayed

But as seen here, and using Equation 3.9, the center of mass is higher than the center of buoyancy. This should mean that the system is unstable and is prone to tipping. However, using a catamaran style boat hull prevents such tipping. Additionally, the wing is mostly hollow since it was 3D printed with a 10% infill density, and provides additional buoyancy not able to be added into this calculation.

3.1.3 Maximum Lift and Power Calculations

Calculating the lift and drag coefficients on the wing will give us an estimate on the maximum achievable power output of the SUSK model. To do this, we use equation 3.10.

$$L_W = \frac{1}{2} C_L \rho V^2 A \tag{3.10}$$

Where L_w is the lift of the wing, C_L is the lift coefficient, ρ is the density, V is the velocity of the wing, and A is the area of the wing.

But first the coefficient of lift and velocity of the wing must be found, using equations 3.11 - 3.13 from finite wing theory (Anderson, 2017), (Loyd, 1980), (Diehl, 2013)

$$C_L = a\left(\alpha - \alpha_{L=0}\right) \tag{3.11}$$

$$a = \frac{a_0}{1+\frac{a_0}{\Pi AR}(1+\tau)} \tag{3.12}$$

$$V_{Wing} = \frac{2}{3}\frac{L}{D} V_C \tag{3.13}$$

Where a_0 is the lift curve slope, AR is the aspect ratio, τ is the non elliptical wing correction factor, and L/D is the lift drag ratio

Then plugging in known values of $a_0 = 0.0751 \frac{1}{degrees}$ and AR = 4 into equation 3.12 (Petilli, 2021). Also using τ = 0.7 for a rectangular wing (NASA, n.d.).

$$a = \frac{0.0751}{1+\frac{0.0751}{\Pi(4)}(1+0.7)} = 0.07434 \frac{1}{degrees}$$

Using this value of a in equation 3.11 with an angle of attack of 8 degrees, which is the angle at which maximum power is achieved (Petilli, 2021).

$$C_L = 0.07434(8 - (-4.875)) = 0.957$$

Next, to find the lift to drag ratio, the drag coefficient must be found. This is done by using equations 3.14 and 3.15.

$$C_D = C_{D,0} + C_{D_I} \tag{3.14}$$

$$C_{D_I} = \frac{C_L^2}{\pi AR\, e} \tag{3.15}$$

For our wing, an efficiency factor e of 0.7 is used, as well as the aspect ratio of 4, and a $C_{D,0}$ of 0.0348 was used (Petilli, 2021).

$$C_{D_I} = \frac{(0.957)^2}{\pi\,(4)\,(0.7)} = 0.104$$

$$C_D = 0.0348 + 0.104 = 0.139$$

This produces a drag of 0.104. To next find the left to drag ratio, we use equation 3.16, plugging in values calculated from equations 3.11 and 3.14.

$$\frac{L}{D} = \frac{C_L}{C_D} \tag{3.16}$$

$$\frac{L}{D}_{max} = \frac{0.957}{0.139} = 6.88$$

Now the velocity of the wing must be found using equation 3.14, using a lift to drag ratio of 6.88. Also, various current velocities will be used, at 0.5 ft/s, 1 ft/s, 1.5 ft/s, and 2 ft/s.

$V_{Wing} = \frac{2}{3}(6.88)(0.5) = 2.293$ ft/s

$V_{Wing} = \frac{2}{3}(6.88)(1) = 4.587$ ft/s

$V_{Wing} = \frac{2}{3}(6.88)(1.5) = 6.88$ ft/s

$V_{Wing} = \frac{2}{3}(6.88)(2) = 9.173$ ft/s

Using each of these velocities in equation 3.11, with lift coefficient as calculated above, density of water at 62.4 lbs/ft^3, and the area of the wing at 2.25 ft^2, show the lift of the wing at different current speeds.

$L_W = \frac{1}{2}(0.957)(62.4)(2.293)^2(2.25)\left(\frac{1}{32.2}\right) = 10.97$ lbf

$L_W = \frac{1}{2}(0.957)(62.4)(4.587)^2(2.25)\left(\frac{1}{32.2}\right) = 43.90$ lbf

$L_W = \frac{1}{2}(0.957)(62.4)(6.88)^2(2.25)\left(\frac{1}{32.2}\right) = 98.76$ lbf

$L_W = \frac{1}{2}(0.957)(62.4)(9.173)^2(2.25)\left(\frac{1}{32.2}\right) = 175.56$ lbf

As the current velocity is increased, the lift of the wing will increase exponentially, putting high importance on placing the SUSK in a location with high current speeds. The current speed will also increase the power generated cubically, shown in equation 3.17.

$$P = \frac{2}{27}\rho V_C^3 A C_L\left(\frac{L}{D}\right)^2 \quad (3.17)$$

Using values from above, with the four current speeds, then converted to Watts, the maximum power outputs are as shown.

$$P_{max} = \frac{2}{27}(62.4)(0.5)^3\,(2.25)(0.957)(6.88)^2\left(\frac{1}{32.2}\right) = 1.83 \text{ lbf ft/s} = 2.48 \text{ W}$$

$$P_{max} = \frac{2}{27}(62.4)(1)^3\,(2.25)(0.957)(6.88)^2\left(\frac{1}{32.2}\right) = 14.63 \text{ lbf ft/s} = 19.84 \text{ W}$$

$$P_{max} = \frac{2}{27}(62.4)(1.5)^3\,(2.25)(0.957)(6.88)^2\left(\frac{1}{32.2}\right) = 49.38 \text{ lbf ft/s} = 66.95 \text{ W}$$

$$P_{max} = \frac{2}{27}(62.4)(2)^3\,(2.25)(0.957)(6.88)^2\left(\frac{1}{32.2}\right) = 117.05 \text{ lbf ft/s} = 158.70 \text{ W}$$

With the max power ranging from 2.57 to 164.54 Watts depending on the water velocity, this scale model system would not be that viable for home use. However, a scaled up system could easily be viable for home use with the average home using 1 KW at any time.

When calculating the actual power output, we must add in the addition of the nozzle to increase power, shown in equation 3.18.

$$A_i V_i = A_o V_o \tag{3.18}$$

$$V_o = \frac{\pi(5)^2(0.5)}{\pi(2.5)^2} = 2 \text{ ft/s}$$

$$V_o = \frac{\pi(5)^2(1)}{\pi(2.5)^2} = 4 \text{ ft/s}$$

$$V_o = \frac{\pi(5)^2(1.5)}{\pi(2.5)^2} = 6 \text{ ft/s}$$

$$V_o = \frac{\pi(5)^2(2)}{\pi(2.5)^2} = 8 \text{ ft/s}$$

Then using equation 2.2 to calculate power using the Betz limit for CP as 0.593, and the updated velocities from the nozzle, with the area of the turbine as 0.136 ft^2

$$P = (0.593)(62.4)(2)^3(0.136)\left(\frac{1}{32.2}\right) = 0.625 \text{ lbf ft/s} = 0.85 \text{ W}$$

$$P = (0.593)(62.4)(4)^3(2.25)\left(\frac{1}{32.2}\right) = 5.00 \text{ lbf ft/s} = 6.78 \text{ W}$$

$$P = (0.593)(62.4)(6)^3(2.25)\left(\frac{1}{32.2}\right) = 16.88 \text{ lbf ft/s} = 22.89 \text{ W}$$

$$P = (0.593)(62.4)(8)^3(2.25)\left(\frac{1}{32.2}\right) = 40.01 \text{ lbf ft/s} = 54.25 \text{ W}$$

The actual power produced turns out to be between 0.85 and 54.25 Watts, about ⅓ of the maximum available power produced.

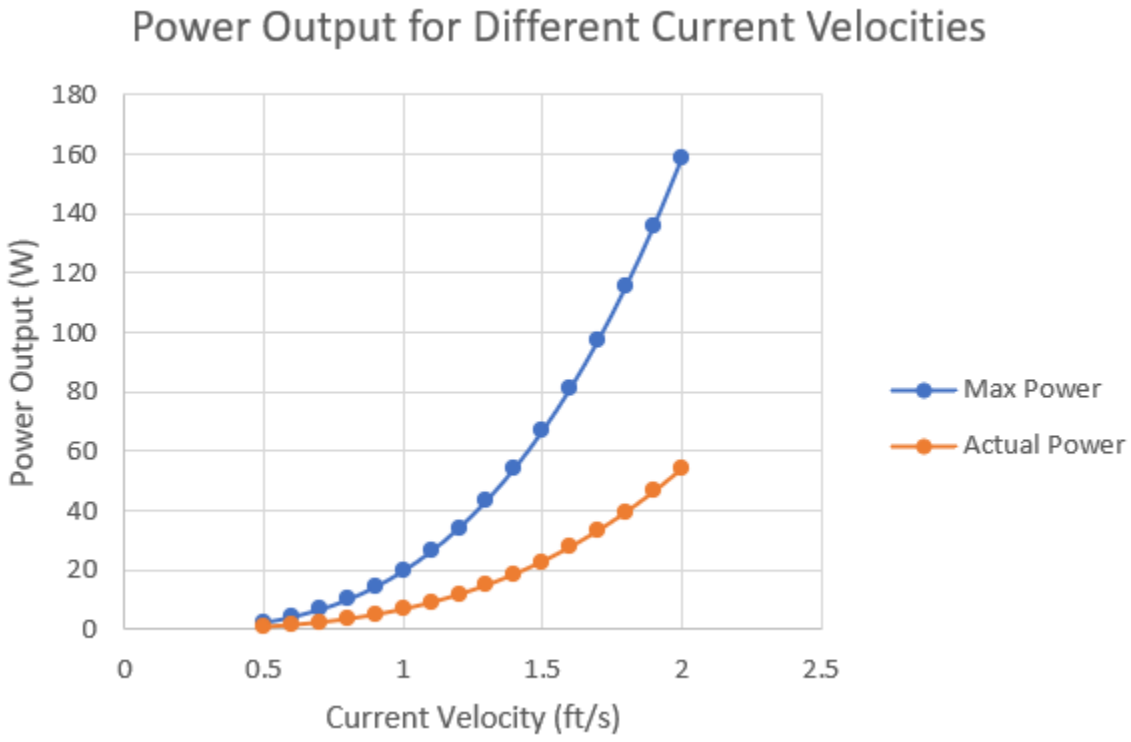

Figure 50: Power output for different current velocities in lbf ft/s

Here it can be seen that the changing current velocity has an even bigger influence on the power output, so placing the SUSK system in a location with high current velocity is very important for successful power generation. If the power for the system at a 2 ft/s current flow is converted into watts, the actual power is 54.25 W. Where the average onshore traditional wind turbine produces around 3 MW, this system could be scaled up to produce enough energy for home use, however will not be viable as a replacement for power plants.

3.2 Static Pool Testing

Testing was performed at the WPI pool with our scale model system. Initially a float test was performed to measure the draft of the boat compared to our preliminary calculations and to make sure the flex seal was successfully applied. The draft was close to the calculated value, both around 1 inch, while the boat and all 3D printed parts were found to be waterproof. For our second test, we aimed to achieve successful cross current motion of the SUSK model, however we ran into issues with the surprisingly large buoyancy of the wing and turbine assembly. This led us to adding ballast weight to the bottom of the system for our third and final pool test. During this we did not successfully get a cross current motion test although that is most likely due to either not having working servos to control the pitch angle of the wing throughout the motion or due to improper placement of the tether (string) attachment point on the boat hull or servo box that we were using to simulate current in the pool.

Additionally, pitch and roll stability were tested for the SUSK's catamaran design. Using a Tracker Software by Open Source Physics, we were able to determine the damping coefficient of the SUSK body through its harmonic resonance.

3.2.1 Pitch Stability

The static test for pitch analysis led to a failure of SUSK's servo connection upon testing. The forces applied on the center servo control box were too great for the system to resonate. Due to the failure we can infer that with this force applied to the system for pitch yielded a breaking point in its design. After initial testing the servo box was refabricated, however this test was not further examined. The figure below represents a snapshot of this breaking point.

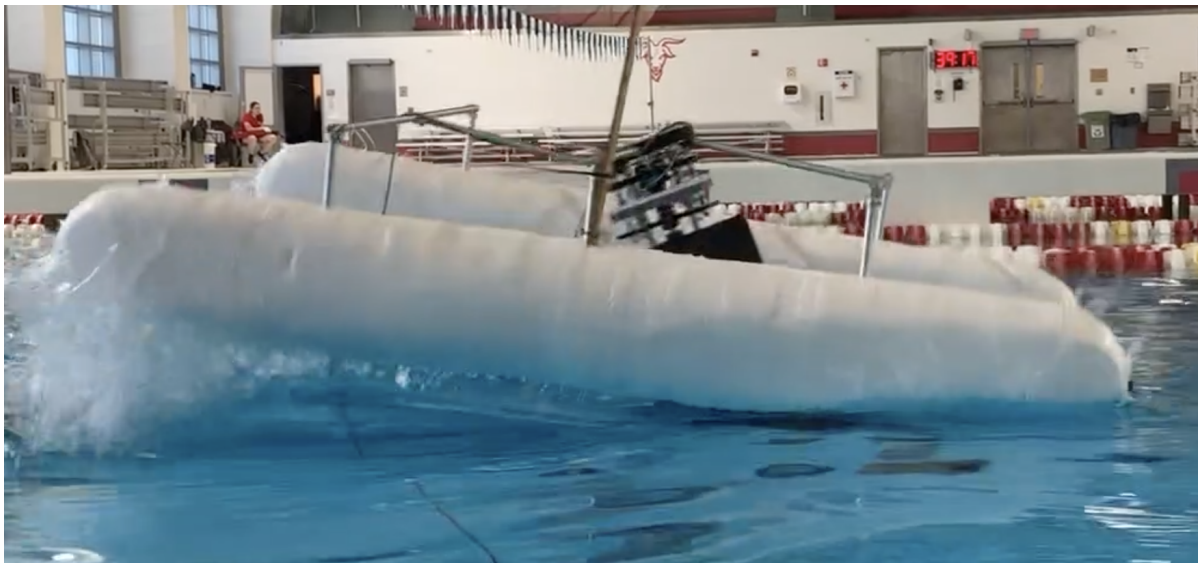

Figure 51: Pitch Stability Testing

3.2.2 Roll Stability

The static test for roll stability was analyzed via the Tracker Software to determine the system's harmonic resonance. The following figures represent the procedure of this analysis.

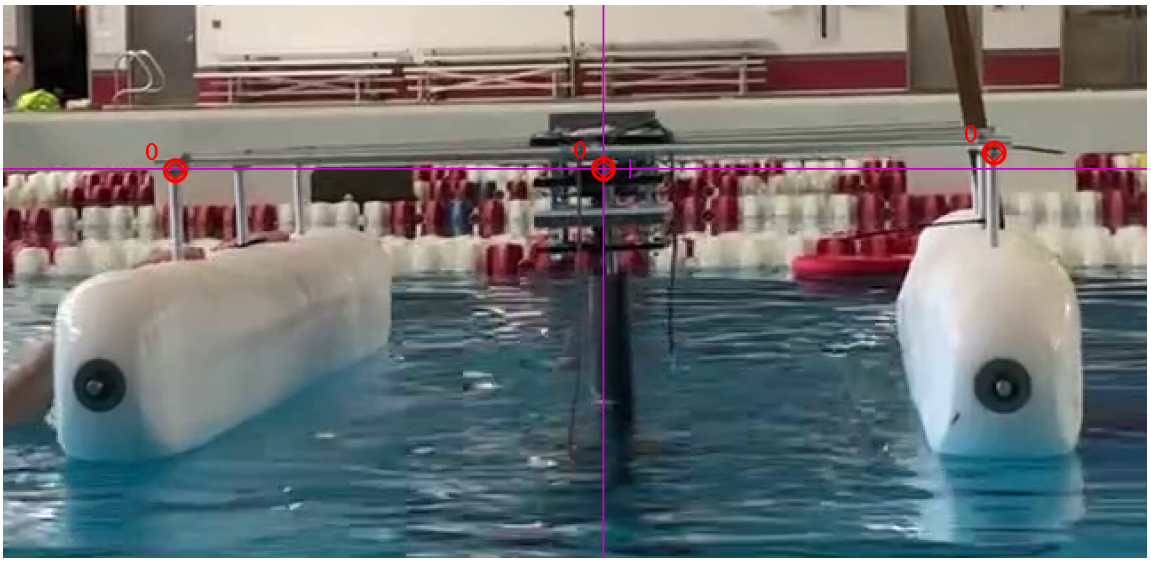

Figure 52: Roll Stability Tracker Origin

An origin was set on the center control box where the tether would be fixed. The two points on each of the hulls were used to determine the change in vertical distance.

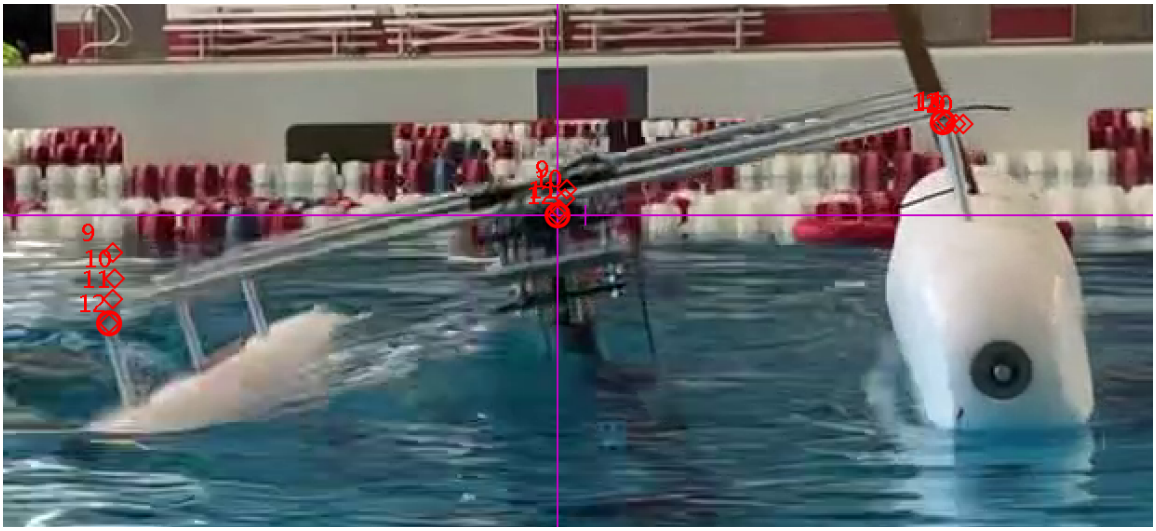

Figure 53: Roll Stability Tracker Force Applied

The restoring moment within a change in roll on SUSK is the relationship between the forces of buoyancy and gravity on each of the hulls.

$$U = \left(F_B - F_g\right) \Delta y \tag{3.17}$$

$$F_B = V\rho g \tag{3.18}$$

$$F_g = mg \tag{3.19}$$

Therefore,

$$U = (V\rho - m)\, g\, \Delta y \tag{3.20}$$

$$\phi = tan\left(\frac{\Delta y}{\Delta x}\right) \tag{3.21}$$

At an angle phi equal to 13.2 degrees a force of 944 [N] was applied to the left hull in a downward direction. This resulted in a potential difference of 118.9 [J] on the system, which

caused the SUSK system to vibrate. The following figures represent snapshots of the bodies positive and negative deflection upon stabilizing.

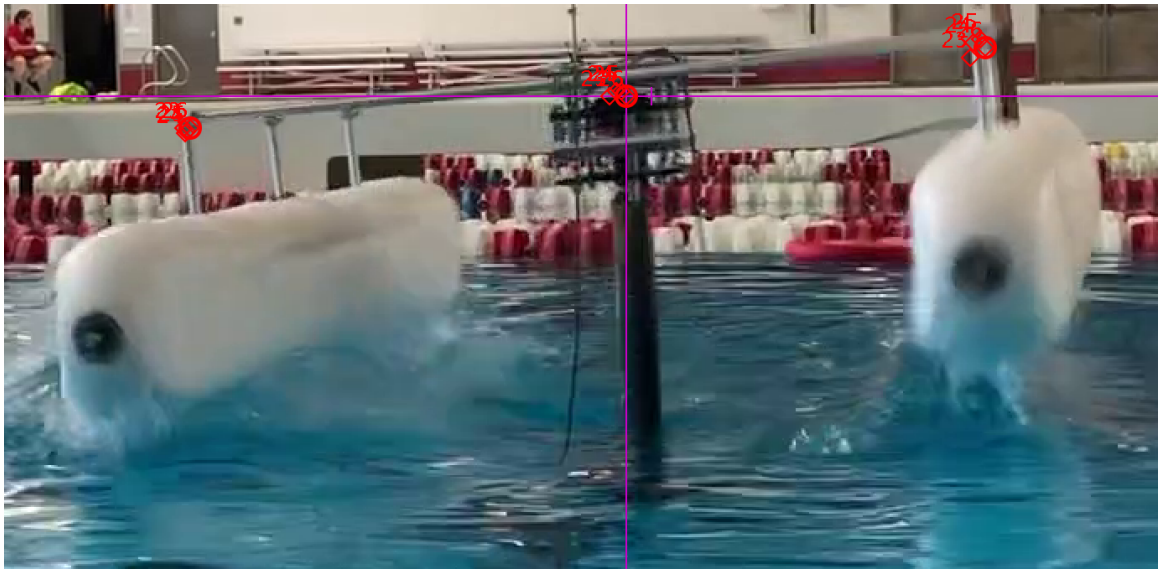

Figure 54: Roll Stability Tracker Negative Deflection

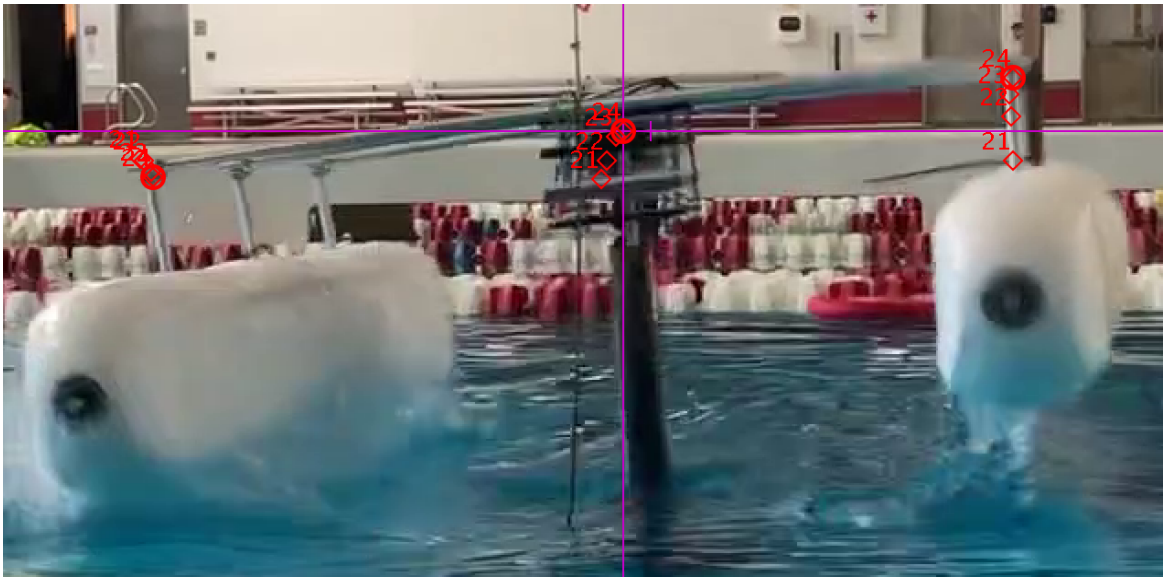

Figure 55: Roll Stability Tracker Positive Deflection

The following data points from the Tracker Software were then imported into MATLAB shown in appendix H. Using the changes in vertical distances of each of the hulls we can determine the damping of the harmonic resonance. The following equation was used for this free vibration test.

$$Ln\left(\frac{u1}{u2}\right) = \frac{2\pi\xi}{\sqrt{1-\xi^2}} \tag{3.22}$$

Where u1 and u2 represent the local maximum points within its harmonic resonance. After a time of 2 seconds the system achieved equilibrium in its roll component. Equation 3.22 concludes that the damping factor for the SUSK system experimentally proved to be $\xi = 0.09$, which was to be expected for this underdamped vibration. The following figure displays the roll angle amplitude with respect to time. The roll angle time trace can also be fitted with a damped sinusoidal oscillation function.

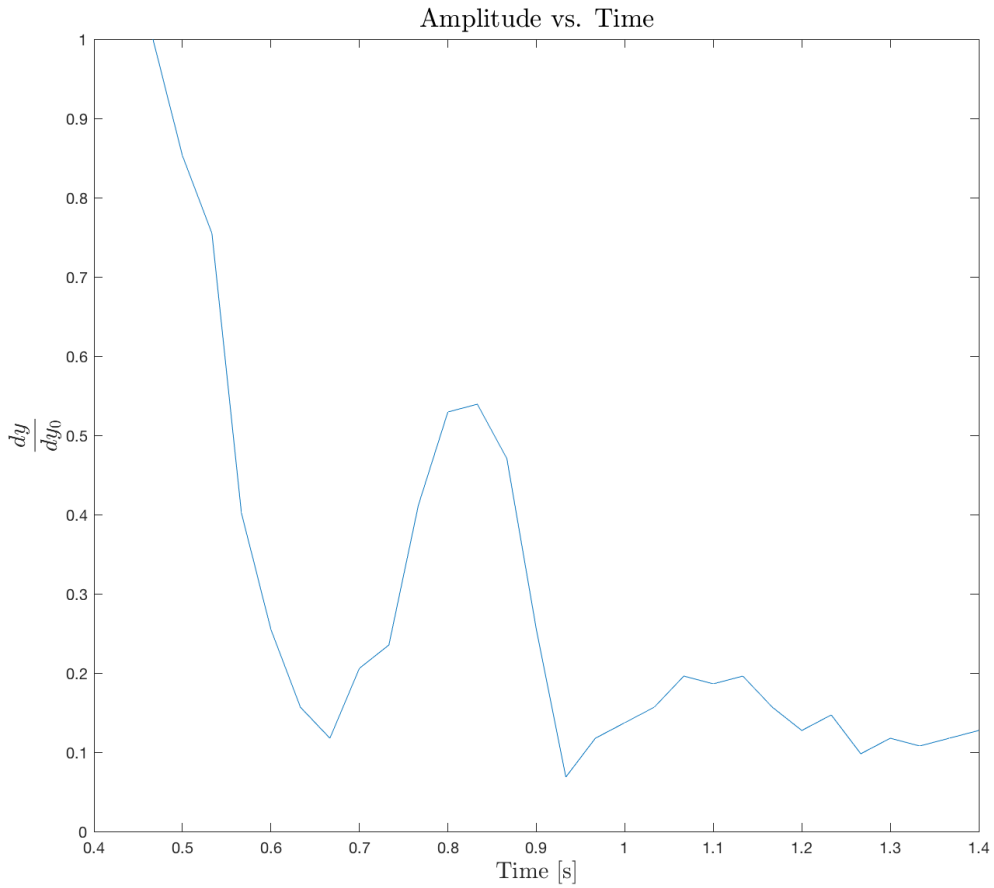

Figure 56: Roll Stability Tracker Experimental Damping Analysis

4 Modeling of SUSK

The modeling of the SUSK system orients with the projects objective to prove to be a more viable source of clean energy. This newer scale model has implemented past research and findings within its design, that this current model serves as a baseline for the project layout. Provided in this section is an updated modeling of SUSK for purposes of past, current, and future understandings on the system.

4.1 SUSK Equations of Motion (EOM)

The SUSK system uses a cross current motion that can provide a significant amount of clean energy. The potential energy stored in the current flow of moving water is where SUSK can prove its capabilities in transmitting clean kinetic energy. The SUSK Equations of Motion (EOM) demonstrate these energies within the system throughout SUSK's arcing motion. The overall objective established from the EOM is to increase the apparent velocity upon the SUSK generator, yielding the highest possible power output.

4.1.1 Introduction to System

The following figure below represents the full SUSK model. This system has a catamaran designed hull, and a wing containing a higher 4:1 aspect ratio. Past iterations of the system proved these were the best techniques for this tethered ocean energy system. This model will incorporate a fixed above water level tether connecting the SUSK system downstream; where the tether is a fixed length, at a fixed attachment point. This interpretation also contains a fixed tether connection at the top of SUSK, that this angle will always be perpendicular to the hulls. The full SUSK model figure represents a snapshot of the SUSK system with hulls perpendicular to the current velocity throughout its arc. This image is when the system is at $\theta = 0°$.

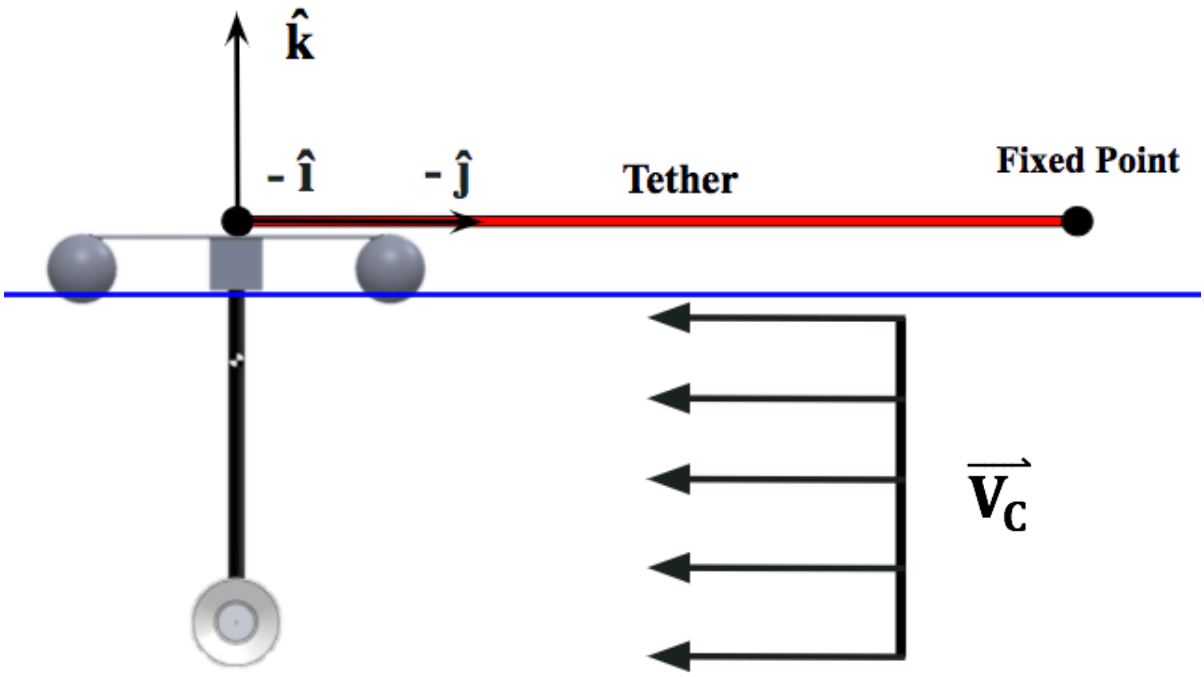

Figure 57: Full SUSK Model

The respected Cartesian Coordinate system is denoted at an origin on the tether connection on the top of SUSK, where î is out of the page. This enables the following forces and torques on the SUSK body, where the forces on SUSK below are denoted as a point mass at $\theta = 0°$.

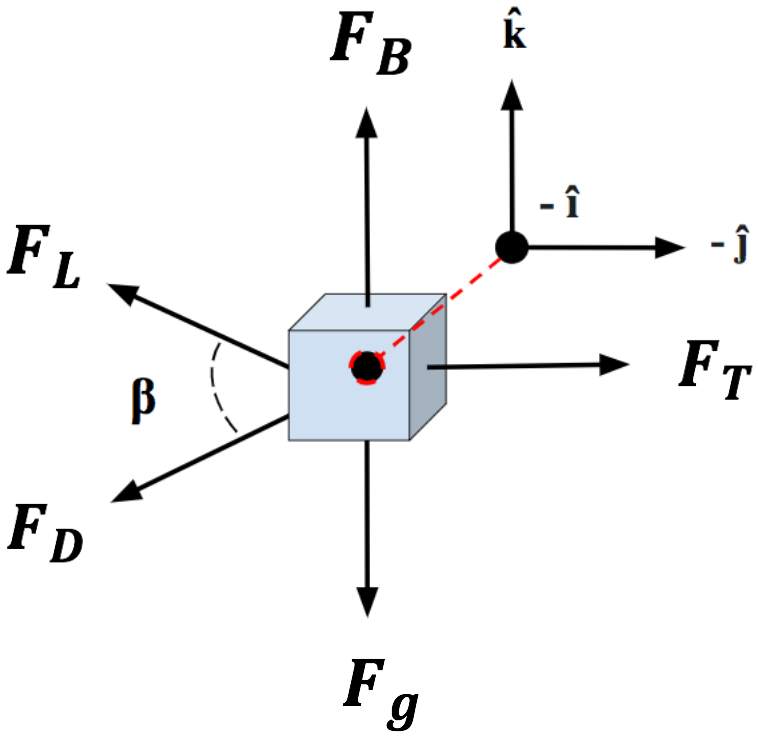

Figure 58: Forces on SUSK

In this representation, angle β is the relationship between the Force of Lift and Force of Drag on SUSK throughout its motion. The following forces are as followed:

F_L denotes the Force of Lift

F_D denotes the Force of Drag

F_B denotes the Force of Buoyancy

F_T denotes the Force of Tension from the Tether

F_g denotes the Force of Gravity

Due to the rigid connection of the tether on the top of SUSK, the following torques will be implemented on the system. The following figure below represents the nature at which these torques are applied due to the shape of SUSK.

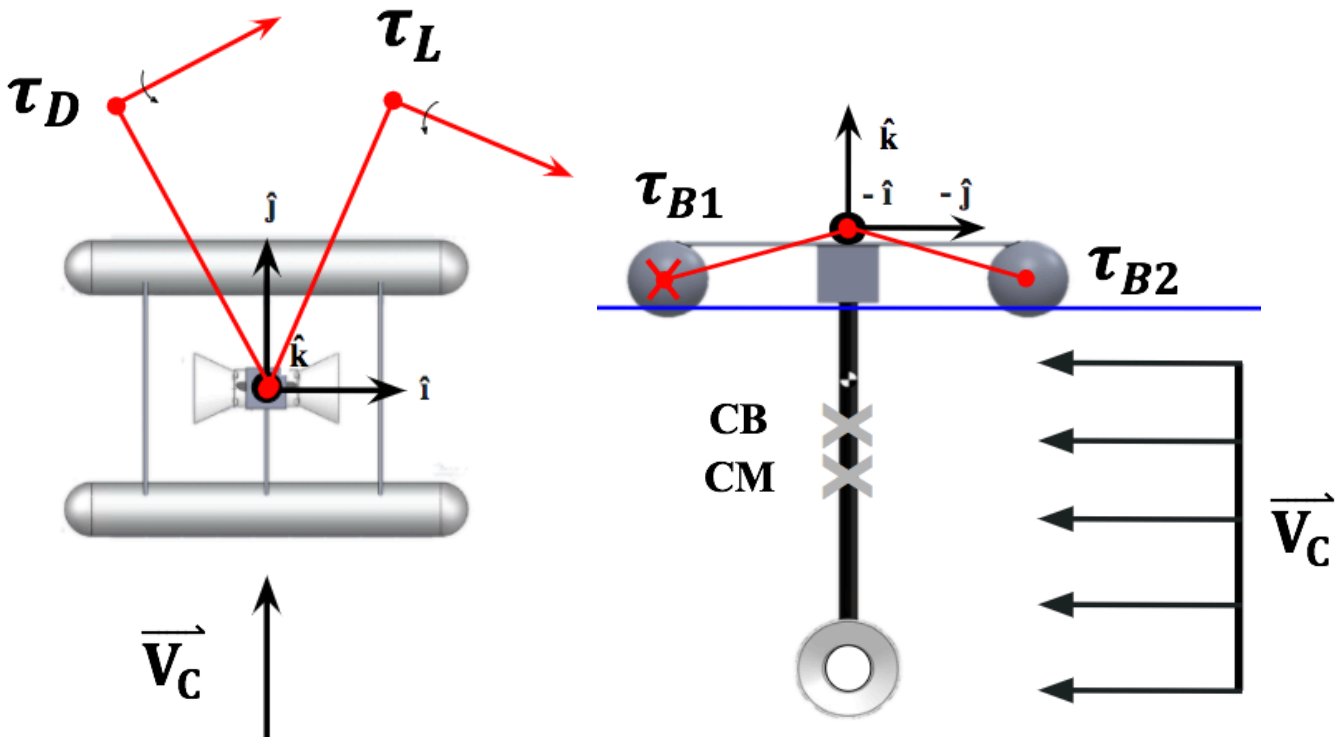

Figure 59: Torques on SUSK

In this depiction the center of mass will be symmetrical at the origin of the body in the x-y plane. This is due to the symmetric nature of the catamaran designed hull. The center of buoyancy however can move slightly throughout the SUSK motion. The following torques are applied in the orientations depicted above, SUSK is traveling in $+\hat{\imath}$. The following image legend is as followed:

CM denotes the Center of Mass

CB denotes the Center of Buoyancy

τ_L denotes the Torque due to Lift

τ_D denotes the Torque due to Drag

τ_B denotes the two Torques due to Buoyancy

Note that in this illustration the origin is taken from the tether attachment point, therefore the torque due to the tension of the tether will be zero. However this infers that this attachment point on SUSK will undergo a significant amount of stress throughout its motion.

In this model the SUSK system will oscillate in a cross current motion downstream at an angle theta. Figure 60 expresses the model at $\theta = 0°$. The figures below represent a bird's eye view of the system. That this orientation will help visualize the phases of the position of SUSK.

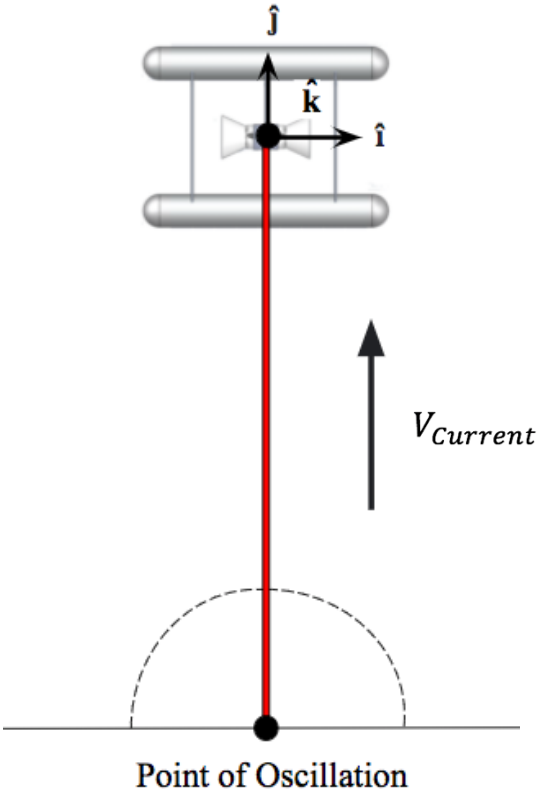

Figure 60: 'Birds Eye View' of SUSK Cross Current Motion

Throughout the motion of SUSK, the forces of lift and drag will range depending on the position of SUSK. This will correlate to the torques of lift and drag to also range. This relationship of the forces and torques of lift and drag of SUSK is denoted by angle beta shown in figure 58.

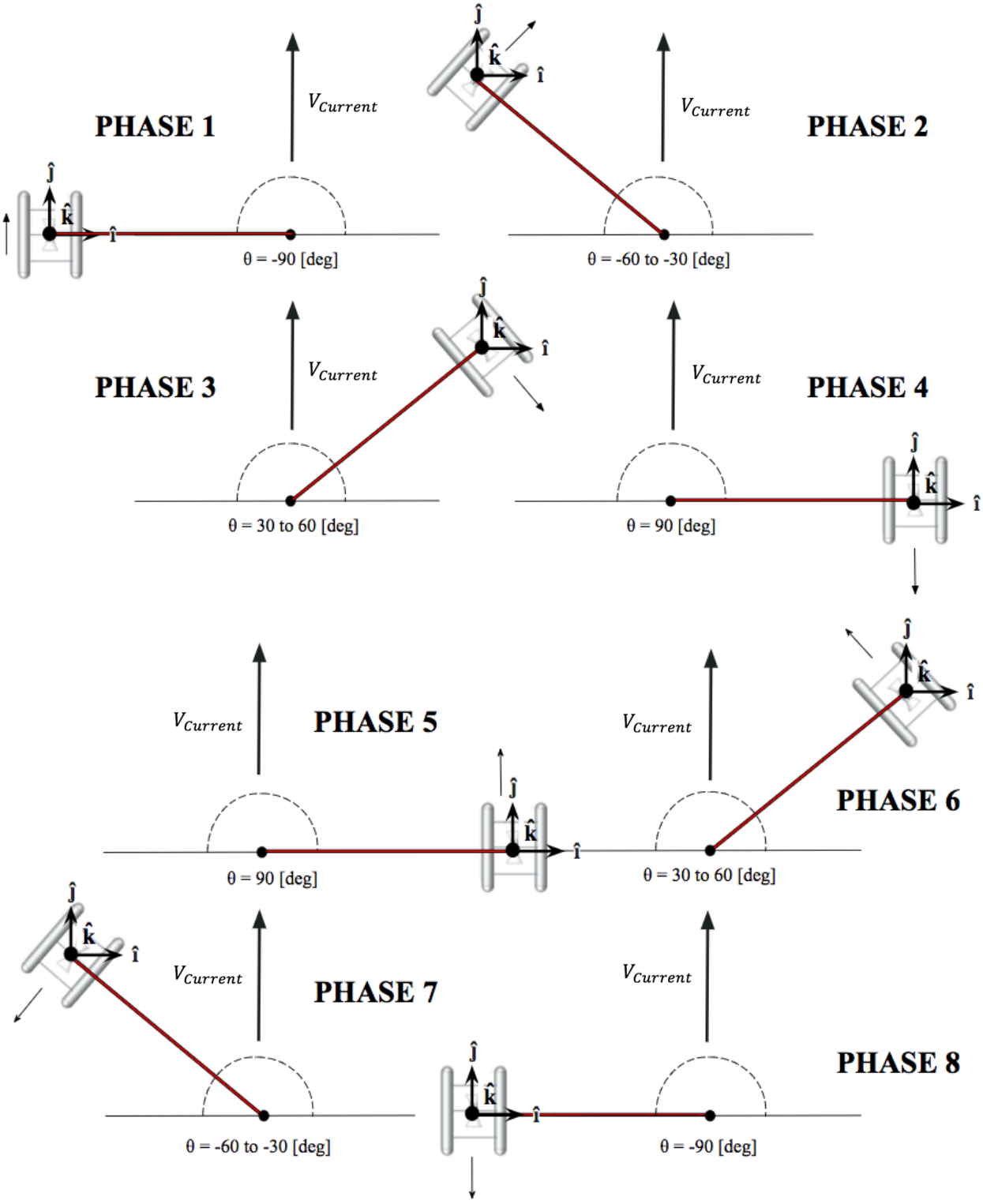

Figure 61: 'Birds Eye View' of SUSK Cross Current Phases

The above figure 61 represents the eight phases of a half period in SUSK's motion.

Denoted above at $\theta = -90$ and 90 degrees is the turning point of SUSK within its oscillation. Since SUSK is changing direction at this turning point the Force of Lift will have zero magnitude, the Force of Drag should be at its maximum magnitude. These phases above represent a maximized variation of the system. Meaning that depending on the systems numerical values, such as its area, weight, lift to drag ratio, and current velocity will determine its turning point. That its oscillations turning points may vary depending on these conditions.

4.1.2 Newtonian Approach

To better understand the EOM of SUSK first we must denote each of the Coordinate Systems. A spherical coordinate system is used to determine the position and velocity vectors of SUSK. The origin of this reference frame is at its anchored point of oscillation. Note that the SUSK body has its own cartesian origin denoted in the section above, however this represents the Euler angles of the body's orientation: yaw, pitch, and roll.

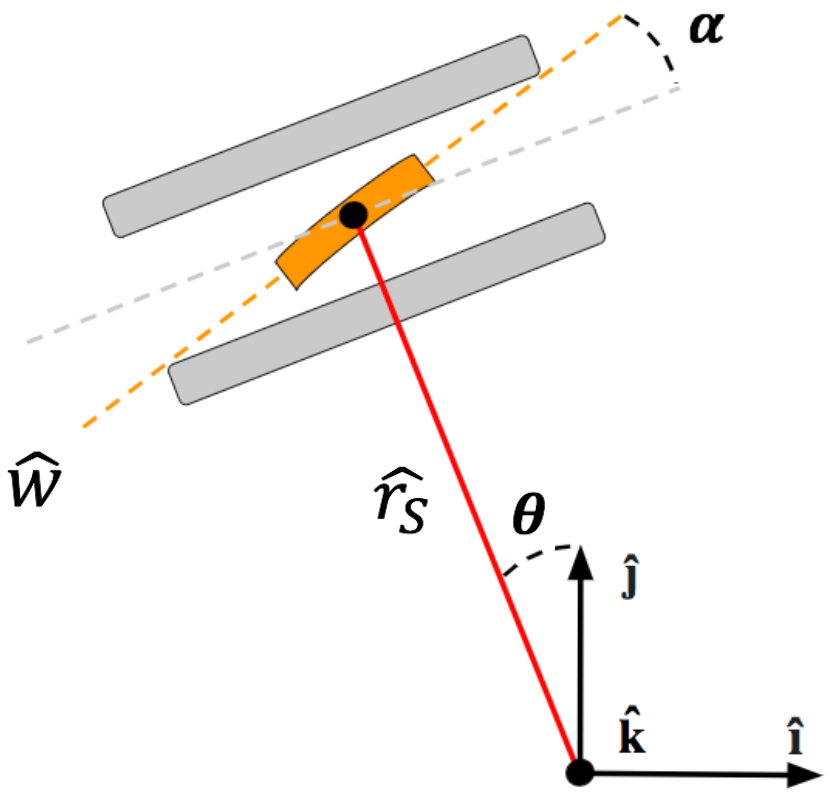

Figure 62: SUSK Position Vectors

In this representation above, $\hat{r_S}$ denotes the position vector of SUSK and $\hat{w}$ denotes the wing orientation with respect to SUSK at an angle of attack α; also known as the pitching angle that will yaw SUSK. Recall that the tether angle from the point of oscillation is at a negative θ in this depiction above. Since both points are on the same location above the water level, $\hat{k}$ is unchanging.

This system is now deduced into a 2-dimensional problem. The radial component in this system is the length of the tether, which we will refer to as L_T . The dependent variable in this scenario is θ. The following position and velocity vectors of SUSK can now be determined.

That the position is,

$$\overrightarrow{r_S} = L_T \sin(\theta)\, \hat{\imath} + L_T \cos(\theta)\, \hat{\jmath} \qquad (4.1)$$

∴ the velocity is,

$$\overrightarrow{v_S} = L_T \cos(\theta)\dot{\theta}\, \hat{\imath} - L_T \sin(\theta)\dot{\theta}\, \hat{\jmath} \qquad (4.2)$$

Now we can orient an apparent velocity on the body of SUSK, this untimely denotes the input velocity upon the generator throughout its motion.

That,

$$\overrightarrow{v_A} = \overrightarrow{v_C} - \overrightarrow{v_S} \qquad (4.3)$$

Where,

$$\overrightarrow{v_C} = v_C\, \hat{\jmath} \qquad (4.4)$$

∴

$$\overrightarrow{v_A} = \left(-L_T \cos(\theta)\dot{\theta}\right) \hat{\imath} + \left(v_C + L_T \sin(\theta)\dot{\theta}\right) \hat{\jmath} \qquad (4.5)$$

The wing orientation $\widehat{w}$ can further be reasoned to determine the effective angle of attack for SUSK.

That,

$$\widehat{w} = \cos(\theta + \alpha)\hat{\imath} + \sin(\theta + \alpha)\hat{\jmath} \qquad (4.6)$$

The effective angle of attack is denoted below for the pitching angle of the wing of SUSK throughout its motion. For purposes of controlling SUSK's yaw to maximize its velocity.

$$\cos(\alpha_{effective}) = \frac{\widehat{w} \cdot \overrightarrow{v_A}}{\|v_A\|} \qquad (4.7)$$

Due to the periodic motion the orientation of SUSK will compose of four cases of flow with respect to the positioning of the wing. These cases can be visualized by phases 2, 3, 6, and 7 previously iterated in figure 61. This will correspond to geometric conversions of the effective angle of attack within SUSK's lift and drag, this will deduce four Normal and Axial Force cases. These relations are shown in appendix D. That these relationships stem from their parent equations below.

$$C_L = C_n \cos(\alpha) - C_a \sin(\alpha) \qquad (4.8)$$

$$C_D = C_n \sin(\alpha) + C_a \cos(\alpha) \qquad (4.9)$$

For the SUSK cross current motions, the following assumptions and parameters are made. The movement of SUSK uses an angle of attack control previously iterated by SUSK research in 2017 noted in Appendix H. The newer SUSK model has made the following variations. Further assumptions are also noted in chapter's 1 and 3.

Table 3: SUSK Input Parameters

SUSK Parameters	**Value**	**Unit**
SUSK Mass	12.25	[kg]
Hull Draft Area	0.13	[m^2]
$V_{Current}$	.61	[m/s]
$\theta_{t=0}$	$\frac{\pi}{2}$	[rad]
L_T	3.66	[m]

After running the dynamic simulation, the following is determined along with SUSK's Cartesian positioning.

The figure below represents the positioning and range of SUSK throughout its arcing motion. Due to the input parameters made in table 3, specifically the current velocity, results in a settling range of roughly $\theta = +/- 49°$ after its first period. Increasing this current velocity decreases the settling range and vice versa.

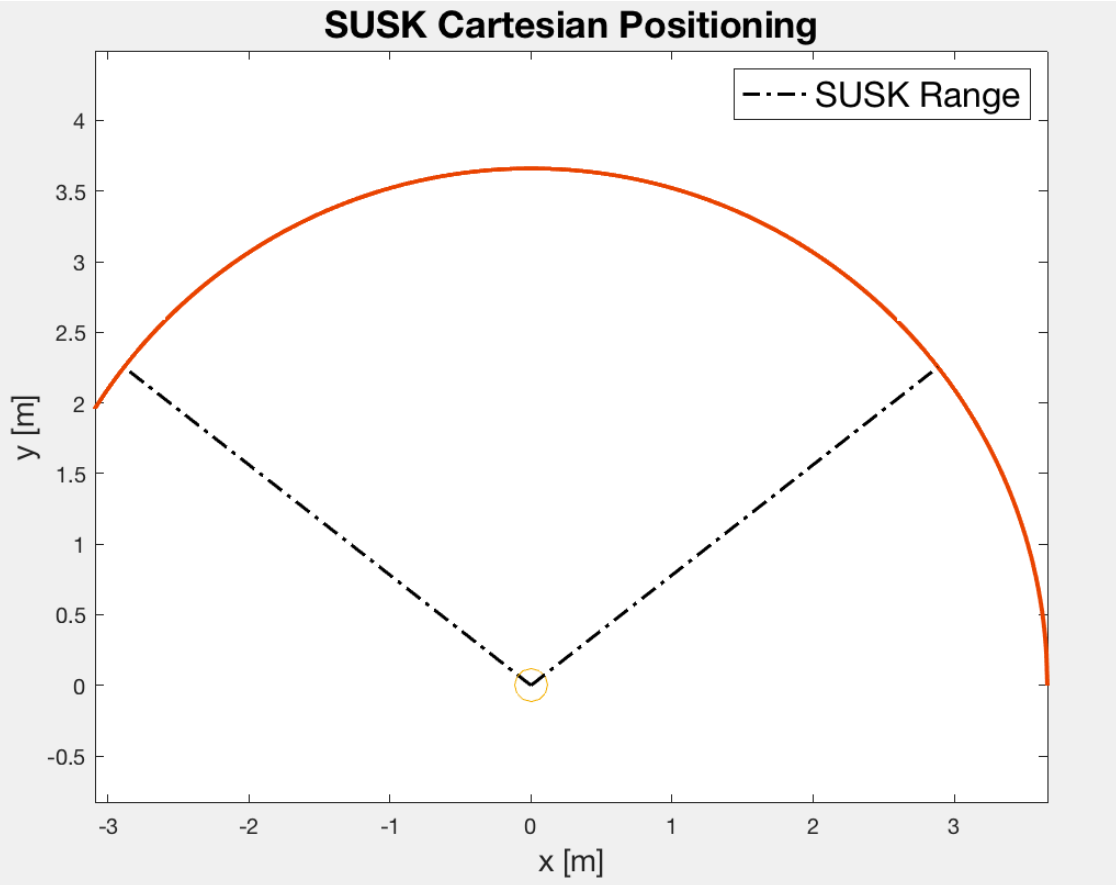

Figure 63: Cartesian Positioning and Range of SUSK

4.1.3 LaGrangian Approach

In its simplest form the Euler-Lagrange equations can be used to interpret the SUSK system. The Lagrangian Density ($\mathcal{L}$) is the energy that describes the overall energy of the system. That,

$$\mathcal{L} = T - U \qquad (4.10)$$

Where T and U represent the kinetic and potential energies respectively. For the SUSK system we denote the corresponding energies are as followed. That,

$$T = \frac{1}{2} m_S \left(\dot{x}^2 + \dot{y}^2 + \dot{z}^2 \right) \qquad (4.11)$$

$$U = U\,(x, y, z) \qquad (4.12)$$

Where the following Euler-Lagrange relations are rationalized,

$$\frac{\partial \mathcal{L}}{\partial x} = -\frac{\partial U}{\partial x} = F_x \qquad (4.13)$$

$$\frac{\partial \mathcal{L}}{\partial \dot{x}} = \frac{\partial T}{\partial x} = m\,\dot{x} = P_x \qquad (4.14)$$

For the purposes of the SUSK system in these equations, it is important to denote our generalized coordinates. This system includes three position variables in spherical coordinates, and three orientation Euler angles. The following is denoted below.

Table 4: SUSK Lagrange Generalized Coordinates

	Coordinate		SUSK System
Position in Spherical Coordinates	q_1	L_T	Fixed
	q_2	θ	Dependent Variable
	q_3	ϕ	Fixed*
Euler Orientation Angles	q_4	ϕ	N/A
	q_5	θ	N/A
	q_6	ψ	N/A

*Note: Unlike the TUSK system, the SUSK system is a surface system.

These generalized coordinates can now be used in the following Euler-Lagrange relations. Recall Hamilton's Principal for a system with six coordinates to be,

$$\mathcal{L} = \mathcal{L}\,(q_1, q_2, q_3, \dot{q_1}, \dot{q_2}, \dot{q_3}) \qquad (4.15)$$

$$\mathcal{S} = \int_{t_1}^{t_2} \mathcal{L}\,(q_1, q_2, q_3, \dot{q_1}, \dot{q_2}, \dot{q_3}, t)\ \partial t \qquad (4.16)$$

Therefore, the Euler-Lagrange equation,

$$\frac{\partial \mathcal{L}}{\partial q_i} = \frac{\partial}{\partial t}\left(\frac{\partial \mathcal{L}}{\partial \dot{q}_\iota}\right) \quad [i = 1, \dots, n] \qquad (4.17)$$

In the SUSK system we will use this equation (4.17) for $i = 1, 2, 3$ to determine the equations of motion. A full derivation of these equations is provided in appendix C. The dependent variable θ in this system ultimately becomes,

$$\ddot{\theta} = \left[Q_\theta + \frac{1}{2}(\rho_c - \rho_b) g {L_T}^2 \sin(\theta) - m_S g (RB) L_T \sin(\theta)\right] * \left(\frac{1}{3}\rho {L_T}^3 + m_S {L_T}^2\right)^{-1} \qquad (4.18)$$

In this depiction Q_θ represents the generalized force associated with θ. Where this generalized force is the summation of torques being applied on SUSK throughout its motion.

4.2 Comparative Analysis

To determine the Kinetic and Potential Energies of the SUSK system the Lagrange approach is simplified to conclude the EOM once again. The relationship of these EOM can then provide an estimate of the expected power output of SUSK.

4.2.1 Kinetic and Potential Energies

In its simplest form the SUSK system arcs back and forth over this cross current motion. The energy of this system is deduced by SUSK as a point mass over the length of the above water tether. Note that due to SUSK being on the surface of the water the potential energy here will be equal to zero, that unlike a pendulum the forces of buoyance and gravity will cancel out any potential forces. Consider the tether to be fixed and above water with an equal density throughout. From the origin of the gimbling mount, the following can be rationalized.

$$T_{system} = T_{SUSK} + T_{tether} \qquad (4.19)$$

Where the kinetic energy of SUSK,

$$T_{SUSK} = \frac{1}{2} m_S {v_S}^2 \qquad (4.20)$$

That in rotational motion,

$$v = r\,\omega = r\,\dot{\theta} \qquad (4.21)$$

∴

$${v_S}^2 = {L_T}^2\,\dot{\theta}^2 \qquad (4.22)$$

Giving,

$$T_{SUSK} = \tfrac{1}{2} m_S {L_T}^2\,\dot{\theta}^2 \qquad (4.23)$$

For the tether of the system,

$$\partial T_{tether} = \frac{1}{2}\, v^2\, \partial m = \frac{1}{2}\left(s\,\dot{\theta}\right)^2 (\rho\, \partial s) \qquad (4.24)$$

Where ρ is the linear density of the tether.

∴

$$T_{tether} = \frac{1}{2}\, \rho\, \dot{\theta}^2 \int_0^{L_T} s^2\, \partial s \qquad (4.25)$$

Giving,

$$T_{tether} = \frac{1}{6}\, \rho\, {L_T}^2\, \dot{\theta}^2 \qquad (4.26)$$

∴

$$T_{system} = \frac{1}{2}\, m_S\, {L_T}^2\, \dot{\theta}^2 + \frac{1}{6}\, \rho\, {L_T}^2\, \dot{\theta}^2 \qquad (4.27)$$

Yielding the Lagrangian Energy to be,

$$\mathcal{L} = T_{system} - U_{system} \qquad (4.28)$$

Recall that the potential energy here is zero.

Therefore $\mathcal{L}$ simplifies too,

$$\mathcal{L} = \frac{1}{2}\, {L_T}^2\, \dot{\theta}^2 \left(\frac{\rho\, L_T}{3} + m_S\right) \qquad (4.29)$$

Now the Euler-Lagrange equations can be applied to solve for $\ddot{\theta}$

$$\frac{\partial}{\partial t}\left(\frac{\partial \mathcal{L}}{\partial \dot{\theta}}\right) - \frac{\partial \mathcal{L}}{\partial \theta} = Q_\theta \qquad (4.30)$$

∴

$$\ddot{\theta} = \frac{Q_\theta}{{L_T}^2} \left(\frac{\rho\, L_T}{3} + m_S\right)^{-1} \qquad (4.31)$$

Equation (4.31) is proportional to equation (4.18), once again confirming the systems EOM. In the method provided in this section leading up to equation (4.31), the most general approach was used. That the system is a point mass with a potential energy of zero. Appendix C denotes equation (4.18) with a potential energy taking the systems reserve buoyancy into account. However, without this term the equations of motion align.

4.2.2 Simulated Power Output and Generalized Forces

The corresponding EOM denoted in appendix C were used to simulate the generalized forces upon SUSK. This section will illustrate the relationship between the SUSK motion and corresponding forces. Note that in this dynamic simulation $\theta_{t=0} = \frac{\pi}{2}$. Over a duration of 90 seconds in the simulated model of SUSK, roughly three periods were completed.

The following figure 64 represents the dynamic simulation output. Where the top plot theta represents the angle of oscillation sketched in figure 61. It is worth noting that during it's 'settling range' SUSK takes more time to accelerate after its pivot, than its deceleration prior to this turning point. This can be visualized by the angular velocity theta dot on the second plot by its slope before and after the turning point. In the dynamic simulation the code uses a servo control at every turning point. This jerk in pitch control of the wing to yaw SUSK resulted in a glitch on the plots below, specifically more noticeable on the third plot of angular acceleration theta double dot; these increments below are at t = 21, 42, 64, 85. It is also apparent that these settling points attribute the majority of the time spent of SUSK's oscillations.

The fourth and fifth plots of the simulation output correspond to the predicted power output of SUSK and the tether tension due to the forces on the tether due to SUSK. At this settling range of +/- 49 degrees the power output ranges from 2 to 8 [W]. This resembles the maximum and actual power outputs denoted in section [3.1.3].

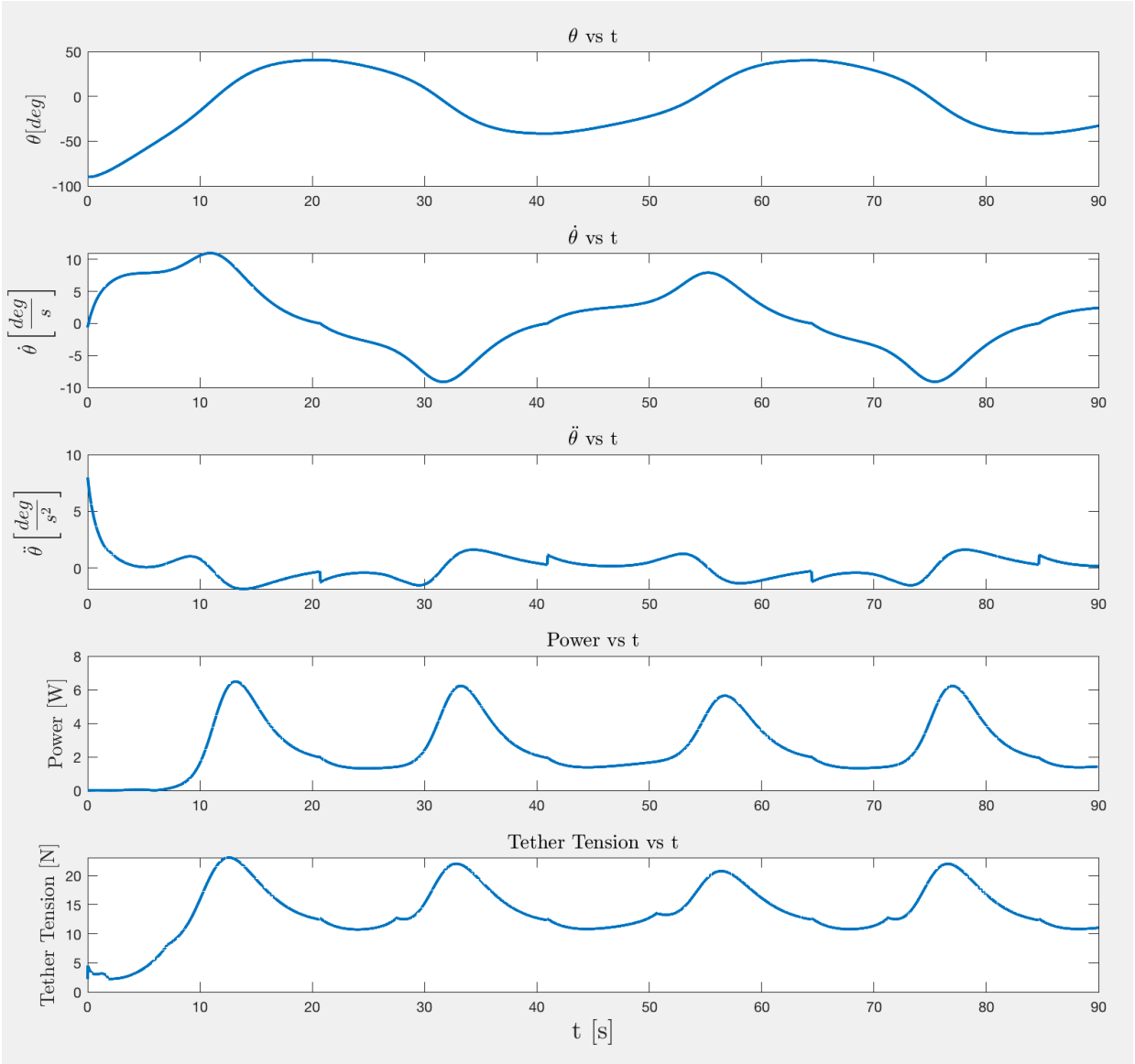

Figure 64: SUSK Dynamic Simulation Output

With the following simulation output of SUSK denoted above, we can once again question how to improve the system for future iterations. The main objective of SUSK is to increase the apparent velocity upon the turbine's generator. Our project iterated a turbine nozzle to increase this flow upon the Well's Turbine blades. However, at what limit will this nozzle attribute more drag on the system resulting in a slower SUSK velocity than its benefits in increasing the generator inflow denoted in equation (3.18). Though this limit may not be that critical in having a slower SUSK oscillation in comparison to the overall power generation. This is something to consider when designing future turbines on the SUSK system.

After this simulation it is worth noting the main takeaway from this 'apparent velocity to power output' relationship is the time it takes for SUSK to settle and redirect in the opposite direction. As noted in the figures above, the majority of the SUSK motion will be spent decelerating and accelerating within these turning points. Future ideas should consider alternative schemes for this process. Past and current interpretations yield SUSK's wing to turn perpendicular to the current flow at these turning points to create the most 'deadweight or drag' to increase acceleration during this turning point.

4.2.3 Simulated Pitch from EOM

The Euler Orientation Angles provided in Appendix A; [A.4], [A.5], [A.6], correspond to the yaw, pitch, and roll of SUSK respectively. Using the pitch of SUSK from the EOM [A.5], we can simulate the relationship of SUSK's pitch over its cross current motion.

For the initial conditions of this simulation, take it that SUSK cannot yaw or roll during this movement. That under this ridged connection from the tether, SUSK can only pitch from front to aft. In this Euler Orientation yaw can assumed to be zero degrees, and roll can assume to be 90 degrees. Therefore, initial conditions,

$$\phi = \frac{\pi}{2}$$

$$\psi = 0$$

$$\dot{\phi} = \dot{\psi} = 0$$

The pitch EOM can now be simplified. From equation [A.5] with the initial conditions provided, the equation now boils down to equation (4.32). Where J_{zz} represents the third eigenvalue in the inertial tensor demonstrated in Appendix E.

$$\ddot{q_5} = \frac{Q_{q5}}{J_{zz}} \qquad (4.32)$$

This simplification can intuitively make sense that only the inertia in the z or $\hat{k}$ direction will affect the pitch of SUSK. Using the values from the inertia tensor in Appendix E the following output simulation of the Euler Orientation angles is provided below. At the time intervals t = 21, 42, 64, 85, the servo control pivots the wing of SUSK, this corresponds to a jerk in motion to disrupt the roll angles slightly. The pitch angles of SUSK range +/- 7 degrees during its settled cross current motion.

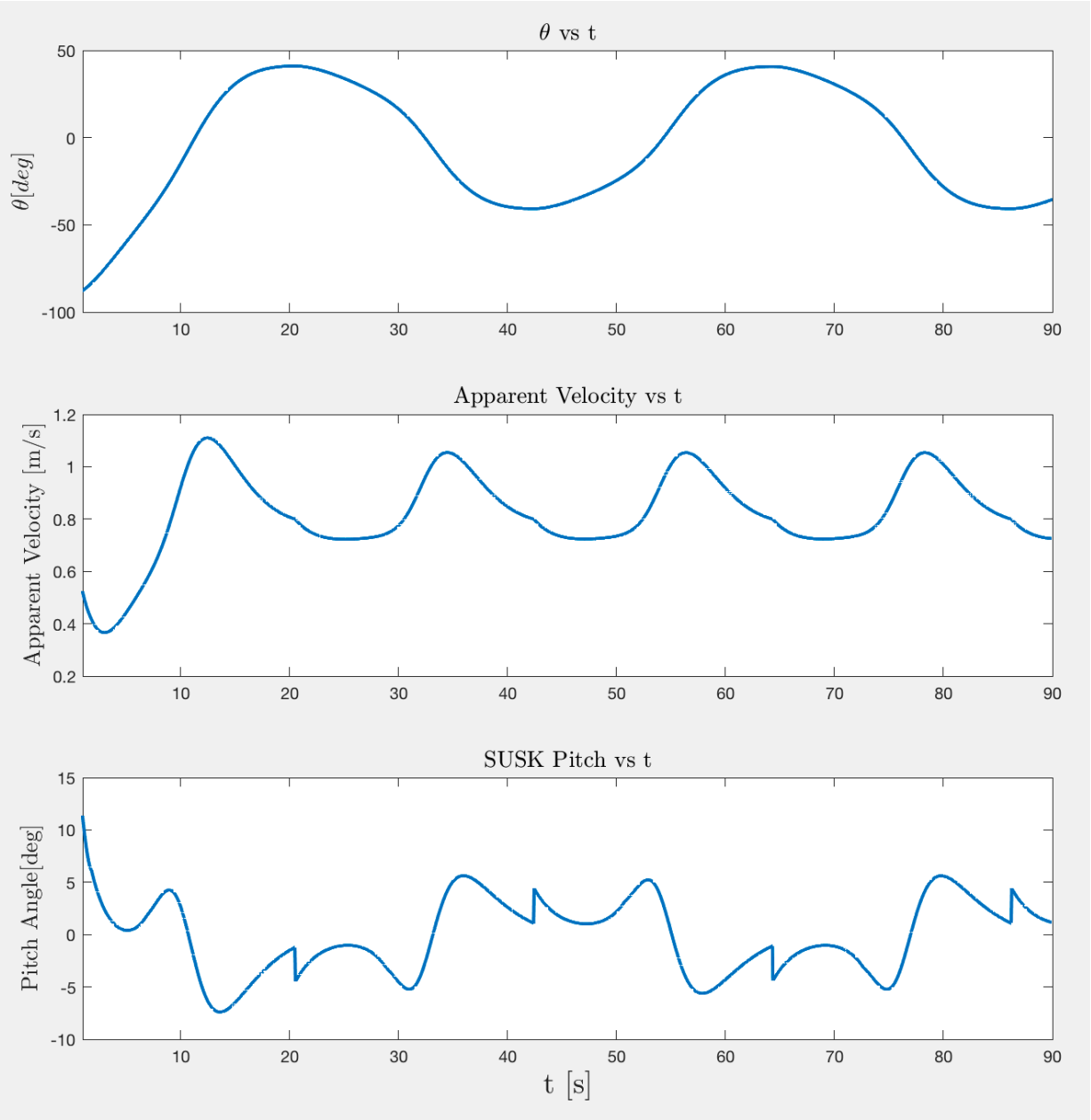

Figure 65: SUSK Dynamic Simulation Pitch Angle

To help visualize the pitching angle of SUSK the apparent velocity upon SUSK denoted in equation (4.5), is also shown to demonstrate when SUSK is traveling at its maximum velocity in phases 3 and 7 during its motion. This corresponds to the highest rate in pitch occurring at these instances.

5 Summary, Conclusions, Recommendations, Broader Impacts

5.1 Summary

Working off of previous MQP's and directed research work, our project aimed to create an improved WPI scale model SUSK system. Our project improved aspects of previous model designs with a new hull, wing, and turbine. Using parameters of a 4:1 aspect ratio with 5% camber and 20% thickness for the wing, a wing with a three foot long wingspan and a nine inch chord was designed and fabricated with 3D printing. For the hull, a catamaran hull design was selected due to having high stability over other shapes, and then created out of styrofoam and aluminum to be 5 feet long and 3 feet wide. Our turbine was created using Wells turbine blades so the blades would spin with the flow coming from both directions, and was also 3D printed. We also decided to try to implement a nozzle into the system, to increase water current velocity at the turbine rotor which increases power output. After fabrication, the hull, wing, and turbine were coated with flex seal so they would be waterproof and then the hull was painted in WPI red with decorative goat logos added.

5.2 Conclusions

The goals of this project outlined in section 1.2 were completed as of D-term of the 2021-2022 academic year. The monohull prototype from previous research was modified and improved to allow for higher power output, and a more stable system overall. The single hull was broken into a catamaran shape to prevent pitching, while the vertical wing was adjusted to have an aspect ratio equaling 4. A nozzle and Well's Turbine was also introduced to the system, which was essential for the production of energy. All components were created using CAD software, including the scale model of the entire system.

Testing was done at the WPI pool throughout the duration of the project. Using the Tracker App, the damping coefficient could be determined through harmonic resonance. This data was gathered by performing pitch and roll stability analysis on the SUSK system. Through these tests, the team was able to determine which aspects of the system required improvement. These tests also provided essential information that was used in other calculations surrounding the system. In addition to preliminary calculations and pool testing, modeling was also done to determine the behavioral motion of SUSK.

During the course of this project, the SUSK system received an overhaul from its previous designs. The team has accomplished the design and construction work that was given in section 1.2, which has laid the groundwork for additional research going forward. Suggestions for future work are outlined in the section below. The only impassible issues met during the duration of this project was due to long shipping times and budgetary constraints.

5.3 Recommendations for Future Work

For future MQP's and research groups, there are some aspects of our SUSK model that can be improved upon. For the hull, more common boat materials can be used, such as fiberglass as opposed to styrofoam, which is difficult to work with as sanding releases dangerous toxins and it can get very messy when cutting. This would also allow for an even more streamlined hull design that would have less drag then our cylinder hull with sanded end caps if a fabricated hull was used. We would also recommend to continue the use of the catamaran design for the hull as it has proven under testing that the stability is unmatched by other hull designs. The catamaran design proves its worthiness by ensuring stability even when the center of buoyancy is above the center of mass.

For the wing, we would also suggest a material change, as the 3D printed wing proved too buoyant, and was also not waterproof, leading to us needing to use Flex Seal and weights. We would suggest a steel or aluminum fabricated metal wing to be used. This would be able to be done in a single piece unlike our lego pieced wing, and could be weighted to increase the stability of the system.

Although our project never successfully included turning the servos to change the angle of attack of the wing, during testing the servo box was put under too much stress from the applied torques and cracked a piece. From this we would suggest including more supports on the servo box or using stronger materials as we used 3D printed parts, so lightweight metal connections may prove to be stronger and also light.

Throughout the project we attempted to purchase a commercial waterproof turbine and generator, however all attempts ended in failure with supply chain issues. We would suggest another attempt to buy the WaterLily turbine or more research needs to be done on current

startups that are creating waterproof turbines/generators for possible implementation into the SUSK system. These turbines could then be modified to custom fit the needs for the project. For example, printing new Well's Turbine blades and replacing those provided by the commercial turbine. Searching for a reliable waterproof generator and a completely custom turbine would also be a viable alternative.

For testing of the system, future pool tests of the SUSK system should include an existing rigid tether instead of the flexible tether that was used, Since pulling on the tether or moving a cart along the pool deck with a rigid tether mimics the current flow. The use of a working servo control box for wing pitch control should be used for better cross-current motion control.

One last suggestion is to test the system in a controlled environment such as Alden research labs to be able to test with current flow as opposed to just pulling the system to simulate current which ended up causing issues in the testing phase of the system. Additionally, instead of using a research lab, another possible testing method would be to tow the WPI SUSK model behind a small boat propelled by a bow-mounted trolling motor to mimic a current flow.

5.4 Project Broader Impacts

This project demonstrated that the SUSK system was a viable option for a renewable energy source if commercialized and placed in the correct locations. Having a reliable renewable energy source able to be used near coastal areas could play a big role in switching away from fossil fuel use as over 40 percent of the world lives near coastal areas. Additionally, the SUSK system could end up being cheaper than traditional wind turbines per kilowatt-hour depending on the price of a commercial model, maintenance costs, and longevity of the system.

Being located in the water, and possibly close to locations where people are living, could impact that area. However, if designed in a way to have a small hull design, they may not be big enough to cause an impact if placed far enough away from the shore. The system will also need to have a noticeable marker or buoy depending on where it is placed so that it will be noticed in the water and not damage the SUSK system.

Appendix A: TUSK Equations of Motion

The equations of motion in this appendix correspond to the TUSK kite-tether system. Where the generalized coordinates are denoted in the table below.

Table 5: TUSK EOM

	Coordinate	
Position in Spherical Coordinates	q_1	Tether Length
	q_2	Tether Cross Wind Angle
	q_3	Tether Elevation Angle
Euler Orientation Angles	ϕ	Roll Angle
	θ	Pitch Angle
	ψ	Yaw Angle

$$\ddot{q_1} = -\Big[-Q_{q1} + mg\,cos(q_2)\,cos(q_3) + \tfrac{1}{2}\big[2g\rho_c\,cos(q_2)\,cos(q_3)q_1 + \rho_c\dot{q_1}^2 - 2mq_1\,\dot{q_2}^2 - \rho_c{q_1}^2\dot{q_2}^2 - q_1 cos^2(q_2)\,(2m + \rho_c q_1) * \dot{q_3}^2\big]\Big] * (m + \rho_c q_1)^{-1} \quad [A.1]$$

$$\ddot{q_2} = -3 * \Big[-Q_{q2} - g\,cos(q_3)\,q_1[-2m * RB + (\rho_c - \rho_b)q_1] * \tfrac{1}{2}\sin(q_2) + q_1(2m + \rho_c q_1)\dot{q_1}\dot{q_2} + \tfrac{1}{6}\big[{q_1}^2(3m + \rho_c q_1)\sin(2q_2)\,\dot{q_3}^2\big]\Big] * [{q_1}^2(3m + \rho_c q_1)]^{-1} \quad [A.2]$$

$$\ddot{q_3} = -3 * \sec^2(q_1)\Big[-Q_{q3} - g\,cos(q_2)\,q_1[-2m * RB + (\rho_c - \rho_b)q_1] * \tfrac{1}{2}\sin(q_3) + q_1\cos^2(q_2)\,(2m + \rho_c q_1)\dot{q_1}\dot{q_3} - 2\cos(q_2){q_1}^2(3m + \rho_c q_1)\dot{q_2}\dot{q_3} * \tfrac{1}{3}\sin(q_2)\Big] * [{q_2}^2(3m + \rho_c q_1)]^{-1} \quad [A.3]$$

Where RB is the reserve buoyancy, that $RB = \frac{F_B - mg}{mg}$

$$\ddot{\phi} = -\Big[-Q_\phi - J_1\cos(\theta)\,\dot{\psi}\dot{\theta} - (J_2 - J_3)\big[\cos(\theta)\sin(\phi)\,\dot{\psi} + \cos(\phi)\,\dot{\theta}\big]\cdot\big[\cos(\theta)\cos(\phi)\,\dot{\psi} + \sin(\phi)\,\dot{\theta}\big]\Big]\cdot$$

$$\frac{1}{J_1}\Bigg\{\sin(\theta)\Bigg[-J_1(J_2 - J_3)\cos(\theta)\sin(2\phi)\cdot\Big[-Q_\theta + \Big([-2J_1 + J_2 + J_3 + (-J_2 + J_3)\cos(2\phi)]\sin(2\theta)\dot{\psi}^2\cdot\frac{1}{4}\Big) +$$

$$\dot{\phi}\Big((J_1 + (J_2 - J_3)\cos(\theta)\cos(2\phi)\,\dot{\psi} + (-J_2 + J_3)\sin(2\phi)\,\dot{\theta}\Big)\Big]\cdot\frac{1}{2} + [J_2 + J_3 + (J_2 - J_3)\cos(2\phi)]\cdot\frac{1}{2}\cdot$$

$$\Big[J_1\sin(\theta)\Big[-Q_\phi - J_1\cos(\theta)\,\dot{\psi}\dot{\theta} - (J_2 - J_3)\big[\cos(\theta)\sin(\phi)\,\dot{\psi} + \cos(\phi)\,\dot{\theta}\big]\big[\cos(\theta)\cos(\phi)\,\dot{\psi} - \sin(\phi)\,\dot{\theta}\big]\Big] +$$

$$J_1\Big[-Q_\psi + \frac{1}{2}[2J_1 - J_2 - J_3 + (J_2 - J_3)\cos(2\phi)]\sin(2\theta)\,\dot{\psi}\dot{\theta} + \frac{1}{2}(-J_2 + J_3)\sin(2\phi)\sin(\theta)\,\dot{\theta}^2 +$$

$$\cos(\theta)\,\dot{\phi}\Big(-J_1\dot{\theta} + (J_2 - J_3)\big(\cos(\theta)\sin(2\phi)\,\dot{\psi} + \cos(2\phi)\,\dot{\theta}\big)\Big)\Big]\Big]\Bigg\}\cdot\Big\{-J_1(J_2 - J_3)^2\cos^2(\theta)\sin^2(2\phi)\cdot\frac{1}{4} +$$

$$[J_2 + J_3 + (J_2 - J_3)\cos(2\phi)]\cdot\Big(J_1\Big[[2J_1 + J_2 + J_3 + (-J_2 + J_3)\cos(2\phi)]\cdot\frac{1}{4} + [-2J_1 + J_2 + J_3 +$$

$$(-J_2 + J_3)\cos(2\phi)]\cos(2\theta)\cdot\frac{1}{4}\Big] - {J_1}^2\sin^2(\theta)\Big)\cdot\frac{1}{2}\Big\}^{-1} \qquad \text{[A.4]}$$

$$\ddot{\theta} = -2\cdot\Big[-Q_\theta + \frac{1}{4}\big[(-2J_1 + J_2 + J_3 + (-J_2 + J_3)\cos(2\phi))\sin(2\theta)\dot{\psi}^2\big] + \dot{\phi}\Big[[J_1 + (J_2 -$$

$$J_3)\cos(2\phi)]\cos(\theta)\,\dot{\psi} + (-J_2 + J_3)\sin(2\theta)\,\dot{\psi}^2\Big] + \dot{\phi}\Big[[J_1 + (J_2 - J_3)\cos(2\phi)]\cos(\theta)\,\dot{\psi} +$$

$$(-J_2 + J_3)\sin(2\phi)\,\dot{\theta}\Big]\Big]\cdot[J_2 + J_3 + (J_2 - J_3)\cos(2\phi)]^{-1} + \Bigg\{(J_2 - J_3)\cos(\theta)\sin(2\phi)\cdot\Big[-\Big[J_1 +$$

$$(J_2 - J_3)\cos(\theta)\sin(2\phi)\cdot\Big[-Q_\theta + \frac{1}{4}\Big[[-2J_1 + J_2 + J_3 + (-J_2 + J_3)\cos(2\phi)]\sin(2\theta)\,\dot{\psi}^2\Big] +$$

$$\dot{\phi}\big([J_1 + (J_2 - J_3)\cos(2\phi)]\cos(\theta)\,\dot{\psi} + (-J_2 + J_3)\sin(2\phi)\,\dot{\theta}\big)\Big]\Big]\cdot\frac{1}{2} + \Big[[J_2 + J_3 + (J_2 -$$

$$J_3)\cos(2\phi)]J_1\sin(\theta)\Big[-Q_\phi - J_1\cos(\theta)\,\dot{\psi}\dot{\theta} - (J_2 - J_3)\big[\cos(\theta)\sin(\phi)\,\dot{\psi} + \cos(\phi)\,\dot{\theta}\big]\big[\cos(\theta)\cos(\phi)\,\dot{\psi} -$$

$$\sin(\phi)\,\dot{\theta}\big]\Big] + J_1\Big(-Q_\psi + [2J_1 - J_2 - J_3 + (J_2 - J_3)\cos(2\phi)]\sin(2\theta)\,\dot{\psi}\dot{\theta}\cdot\frac{1}{2} + \big[(-J_2 + J_3)\sin(2\phi)\sin(\theta)\,\dot{\theta}^2\big]\cdot$$

$$\frac{1}{2} + \cos(\theta)\,\dot{\phi}\Big(-J_1\dot{\theta} + (J_2 - J_3)\big(\cos(\theta)\sin(2\phi)\,\dot{\psi} + \cos(2\phi)\,\dot{\theta}\big)\Big)\Big)\Big]\cdot\frac{1}{2}\Big]\Bigg\}\cdot\Big\{[J_2 + J_3 + (J_2 -$$

$$J_3)\cos(2\phi)]\Big[-J_1(J_2 - J_3)^2\cos^2(\theta)\sin^2(2\phi)\cdot\frac{1}{4} + [J_2 + J_3 + (J_2 - J_3)\cos(2\phi)]\cdot\Big(J_1\Big[[2J_1 + J_2 + J_3 +$$

$$(-J_2 + J_3)\cos(2\phi)]\cdot\frac{1}{4} + [-2J_1 + J_2 + J_3 + (-J_2 + J_3)\cos(2\phi)]\cos(2\theta)\cdot\frac{1}{4}\Big] - {J_1}^2\sin^2(\theta)\Big)\cdot\frac{1}{2}\Big]\Big\}^{-1} \qquad \text{[A.5]}$$

$$\ddot{\psi} = -\left\{-\left[J_1(J_2 - J_3)\cos(\theta)\sin(2\phi)\left[-Q_\theta + \frac{1}{4}\left[[-2J_1 + J_2 + J_3 + (-J_2 + J_3)\cos(2\phi)]\sin(2\theta)\,\dot{\psi}^2\right] + \right.\right.\right.$$

$$\left.\left.\left.\dot{\phi}\left([J_1 + (J_2 - J_3)\cos(2\phi)]\cos(\theta)\,\dot{\psi} + (-J_2 + J_3)\sin(2\phi)\,\dot{\theta}\right)\right]\right] \cdot \frac{1}{2} + [J_2 + J_3 + (J_2 - J_3)\cos(2\phi)] \cdot$$

$$\left(J_1 \sin(\theta)\left[-Q_\phi - J_1\cos(\theta)\,\dot{\psi}\dot{\theta} - (J_2 - J_3)\left[\cos(\theta)\sin(\phi)\,\dot{\psi} + \cos(\phi)\,\dot{\theta}\right]\left[\cos(\theta)\cos(\phi)\,\dot{\psi} - \sin(\phi)\,\dot{\theta}\right]\right] + \right.$$

$$J_1\left(-Q_\psi + [2J_1 - J_2 - J_3 + (J_2 - J_3)\cos(2\phi)]\sin(2\theta)\,\dot{\psi}\dot{\theta} \cdot \frac{1}{2} + \left[(-J_2 + J_3)\sin(2\phi)\sin(\theta)\,\dot{\theta}^2\right] \cdot \frac{1}{2} + \right.$$

$$\left.\left.\cos(\theta)\,\dot{\phi}\left(-J_1\dot{\theta} + (J_2 - J_3)\left(\cos(\theta)\sin(2\phi)\,\dot{\psi} + \cos(2\phi)\,\dot{\theta}\right)\right)\right)\right) \cdot \frac{1}{2}\Bigg\} \cdot \Big\{-J_1(J_2 - J_3)^2\cos^2(\theta)\sin^2(2\phi) \cdot \frac{1}{4} +$$

$$[J_2 + J_3 + (J_2 - J_3)\cos(2\phi)] \cdot \left(J_1\left[[2J_1 + J_2 + J_3 + (-J_2 + J_3)\cos(2\phi)] \cdot \frac{1}{4} + [-2J_1 + J_2 + J_3 + \right.\right.$$

$$\left.\left.(-J_2 + J_3)\cos(2\phi)]\cos(2\theta) \cdot \frac{1}{4}\right] - {J_1}^2\sin^2(\theta)\right) \cdot \frac{1}{2}\Big\}^{-1} \qquad \text{[A.6]}$$

Appendix B: SUSK Equations of Motion

The equations of motion in this appendix correspond to the SUSK tethered system. Where the generalized coordinates are denoted in the table below. The following equations were deduced from Appendix A by applying the SUSK conditions.

Table 6: SUSK EOM

	Coordinate	
Position in Spherical Coordinates	q_1	Tether Length
	q_2	Tether Cross Wind Angle
	q_3	Tether Elevation Angle
Euler Orientation Angles	ϕ	Roll Angle
	θ	Pitch Angle
	ψ	Yaw Angle

$$\ddot{q_1} = -\left[-Q_{q1} + mg\,cos(q_2) + \frac{1}{2}\left[2g\rho_c\,cos(q_2)q_1 + \rho_c\dot{q_1}^2 - 2mq_1\,\dot{q_2}^2 - \rho_c q_1{}^2\dot{q_2}^2\right]\right] * (m + \rho_c q_1)^{-1} \quad [B.1]$$

$$\ddot{q_2} = -3 * \left[-Q_{q2} - gq_1[-2m * RB + (\rho_c - \rho_b)q_1] * \frac{1}{2}\sin(q_2) + q_1(2m + \rho_c q_1)\dot{q_1}\dot{q_2}\right] * [q_1{}^2(3m + \rho_c q_1)]^{-1} \quad [B.2]$$

$$\ddot{q_3} = 0 \quad [B.3]$$

The Euler Orientation angles for the TUSK and SUSK systems are identical. Therefore, [B.4], [B.5], [B.6] correspond to [A.4], [A.5], [A.6] respectively.

Appendix C: Derivation of SUSK Lagrangian and Equations of Motion (EOM)

The derivation of the SUSK Lagrangian uses the following table for its generalized coordinates.

Table 7: SUSK Lagrange Generalized Coordinates

	Coordinate		SUSK System
Position in Spherical Coordinates	q_1	L_T	Fixed
	q_2	θ	Dependent Variable
	q_3	ϕ	Fixed*
Euler Orientation Angles	q_4	ϕ	N/A
	q_5	θ	N/A
	q_6	ψ	N/A

*Note: Unlike the TUSK system, the SUSK system is a surface system.

For the generalized coordinates of SUSK's position, consider a differential length element $\bar{r}$ along the rigid above water level connection tether. With an origin at this anchoring point. Recall since we are denoting the position of SUSK, the generalized coordinate below $(\theta) = q2$.

$$\bar{r} = \begin{bmatrix} L_T \sin(\theta) \\ L_T \cos(\theta) \end{bmatrix}$$

Therefore, the radial velocity of this component with respect to time is,

$$\dot{r} = \frac{\partial r}{\partial t} = \begin{bmatrix} \dot{L_T} \sin(\theta) + L_T \dot{\theta} \cos(\theta) \\ \dot{L_T} \cos(\theta) - L_T \dot{\theta} \sin(\theta) \end{bmatrix}$$

Now we must consider the kinetic energy of this system. In this representation the total energy will compose of the two bodies: the tether and SUSK. Where,

$$T_{SUSK\ System} = T_{Tether} + T_{SUSK}$$

That,

$$T_{SUSK} = T_{Translatonal} + T_{Rotational}$$

To determine the kinetic energy due to the tether we can integrate over its length. That ρ represents its linear mass density,

$$T_{Tether} = \frac{1}{2}\rho \int_0^{L_T} |\dot{r}|^2 \, \partial L_T$$

$$T_{Tether} = \frac{1}{2}\rho \int_0^{L_T} \left| \left(\left(\dot{L_T} \sin(\theta) + L_T \dot{\theta} \cos(\theta) \right)^2 + \left(\dot{L_T} \cos(\theta) - L_T \dot{\theta} \sin(\theta) \right)^2 \right)^{\frac{1}{2}} \right|^2 \partial L_T$$

$$T_{Tether} = \frac{1}{2}\rho \int_0^{L_T} \left| \left(\dot{L_T}^2 + L_T{}^2 \dot{\theta}^2 \right)^{\frac{1}{2}} \right|^2 \partial L_T$$

$$T_{Tether} = \frac{1}{2}\rho \int_0^{L_T} \left(\dot{L_T}^2 + L_T{}^2 \dot{\theta}^2 \right) \partial L_T$$

$$T_{Tether} = \frac{1}{2}\rho \left(L_T \dot{L_T}^2 + \frac{1}{3} L_T{}^3 \dot{\theta}^2 \right)$$

Therefore,

$$T_{Tether} = \frac{1}{2}\rho L_T \dot{L_T}^2 + \frac{1}{6}\rho L_T{}^3 \dot{\theta}^2$$

Next we will determine the total kinetic energy of SUSK, that its translational energy is,

$$T_{Translatonal} = \frac{1}{2} m v^2 = \frac{1}{2} m_S |\dot{r}|^2$$

$$T_{Translatonal} = \frac{1}{2} m_S \left(\dot{L_T}^2 + L_T{}^2 \dot{\theta}^2 \right) = \frac{1}{2} m_S \dot{L_T}^2 + \frac{1}{2} m_S L_T{}^2 \dot{\theta}^2$$

To determine the rotational kinetic energy of SUSK, first we must recall its relation to its inertia tensor. Recall that this is an orientation representation, therefore $(\theta) = q5$ in this term.

$$T_{Rotational} = \frac{1}{2} \omega \cdot I \cdot \omega = \frac{1}{2} \left(J_{xx} \omega_x{}^2 + J_{yy} \omega_y{}^2 + J_{zz} \omega_z{}^2 \right)$$

$$I = J = \begin{bmatrix} J_{xx} & 0 & 0 \\ 0 & J_{yy} & 0 \\ 0 & 0 & J_{zz} \end{bmatrix}$$

The angular velocity can be determined with SUSK's Euler angles,

$$\omega = \begin{Bmatrix}\omega_x\\ \omega_y\\ \omega_z\end{Bmatrix} = \begin{bmatrix}1 & 0 & -\sin(\theta)\\ 0 & \cos(\phi) & \sin(\phi)\cos(\theta)\\ 0 & -\sin(\phi) & \cos(\phi)\cos(\theta)\end{bmatrix}\begin{Bmatrix}\dot{\phi}\\ \dot{\theta}\\ \dot{\psi}\end{Bmatrix} = \begin{bmatrix}\dot{\phi} - \dot{\psi}\sin(\theta)\\ \dot{\theta}\cos(\phi) + \psi\,\dot{\text{sin}}(\phi)\cos(\theta)\\ -\dot{\theta}\sin(\phi) + \dot{\psi}\cos(\phi)\cos(\theta)\end{bmatrix}$$

Therefore,

$$T_{Rotational} = \frac{1}{2}\Big(J_{xx}\big(\dot{\phi} - \dot{\psi}\sin(\theta)\big)^2 + J_{yy}\big(\dot{\theta}\cos(\phi) + \psi\,\dot{\text{sin}}(\phi)\cos(\theta)\big)^2 + J_{zz}\big(-\dot{\theta}\sin(\phi) + \dot{\psi}\cos(\phi)\cos(\theta)\big)^2\Big)$$

$$\begin{aligned}T_{Rotational} = {} & \frac{1}{2}J_{xx}\big(\dot{\phi}^2 - 2\dot{\phi}\dot{\psi}\sin(\theta) + \dot{\psi}^2\sin^2(\theta)\big)\\ & + \frac{1}{2}J_{yy}\big(\dot{\theta}^2\cos^2(\phi) + 2\dot{\theta}\dot{\psi}\cos(\phi)\sin(\phi)\cos(\theta) + \dot{\psi}^2\sin^2(\phi)\cos^2(\theta)\big)\\ & + \frac{1}{2}J_{zz}\big(\dot{\theta}^2\sin^2(\phi) - 2\dot{\theta}\dot{\psi}\cos(\phi)\sin(\phi)\cos(\theta) + \dot{\psi}^2\cos^2(\phi)\cos^2(\theta)\big)\end{aligned}$$

Now that all the kinetic energy terms are accounted for, we can conclude the following potential energy for the SUSK system. The two terms in the potential energy of the system are due to the potential stored between the force of gravity and buoyancy within the tether and SUSK. Note that the potential term uses $(\theta) = q2$. Therefore,

$$U = \frac{1}{2}(\rho_c - \rho_b)g{L_T}^2\cos(\theta) - m_S g(RB)L_T\cos(\theta)$$

Now we can compute the Lagrangian,

$$\mathcal{L} = T_{SUSK\ System} - U_{SUSK\ System}$$

$$\begin{aligned}\mathcal{L} = {} & \frac{1}{2}\rho L_T{\dot{L_T}}^2 + \frac{1}{6}\rho{L_T}^3\dot{\theta}^2 + \frac{1}{2}m_S{\dot{L_T}}^2 + \frac{1}{2}m_S{L_T}^2\dot{\theta}^2 + \frac{1}{2}J_{xx}\big(\dot{\phi}^2 - 2\dot{\phi}\dot{\psi}\sin(\theta) + \dot{\psi}^2\sin^2(\theta)\big)\\ & + \frac{1}{2}J_{yy}\big(\dot{\theta}^2\cos^2(\phi) + 2\dot{\theta}\dot{\psi}\cos(\phi)\sin(\phi)\cos(\theta) + \dot{\psi}^2\sin^2(\phi)\cos^2(\theta)\big)\\ & + \frac{1}{2}J_{zz}\big(\dot{\theta}^2\sin^2(\phi) - 2\dot{\theta}\dot{\psi}\cos(\phi)\sin(\phi)\cos(\theta) + \dot{\psi}^2\cos^2(\phi)\cos^2(\theta)\big)\\ & - \frac{1}{2}(\rho_c - \rho_b)g{L_T}^2\cos(\theta) + m_S g(RB)L_T\cos(\theta)\end{aligned}$$

To solve for the EOM for the generalized coordinates, the following Euler-Lagrange is as followed,

$$\frac{\partial}{\partial t}\left(\frac{\partial \mathcal{L}}{\partial \dot{q}_i}\right) - \left(\frac{\partial \mathcal{L}}{\partial q_i}\right) = Q_{q_i}$$

For the first coordinate,

$$\frac{\partial}{\partial t}\left(\frac{\partial \mathcal{L}}{\partial \dot{L_T}}\right) = Q_{L_T} + \left(\frac{\partial \mathcal{L}}{\partial L_T}\right)$$

Where,

$$\left(\frac{\partial \mathcal{L}}{\partial \dot{L_T}}\right) = \rho L_T \dot{L_T} + m_S \dot{L_T}$$

$$\left(\frac{\partial \mathcal{L}}{\partial L_T}\right) = \frac{1}{2}\rho \dot{L_T}^2 + \frac{1}{2}\rho {L_T}^2 \dot{\theta}^2 + m_S L_T \dot{\theta}^2 - (\rho_c - \rho_b) g L_T \cos(\theta) + m_S g (RB)\cos(\theta)$$

Therefore,

$$\frac{\partial}{\partial t}\left(\rho L_T \dot{L_T} + m_S \dot{L_T}\right) = Q_{L_T} + \frac{1}{2}\rho \dot{L_T}^2 + \frac{1}{2}\rho {L_T}^2 \dot{\theta}^2 + m_S L_T \dot{\theta}^2 - (\rho_c - \rho_b) g L_T \cos(\theta) + m_S g (RB)\cos(\theta)$$

$$\ddot{L_T} = \left[Q_{L_T} + \frac{1}{2}\rho \dot{L_T}^2 + \frac{1}{2}\rho {L_T}^2 \dot{\theta}^2 + m_S L_T \dot{\theta}^2 - (\rho_c - \rho_b) g L_T \cos(\theta) + mg(RB)\cos(\theta)\right] * (\rho L_T + m_S)^{-1}$$

For the second coordinate,

$$\frac{\partial}{\partial t}\left(\frac{\partial \mathcal{L}}{\partial \dot{\theta}}\right) = Q_\theta + \left(\frac{\partial \mathcal{L}}{\partial \theta}\right)$$

Where,

$$\left(\frac{\partial \mathcal{L}}{\partial \dot{\theta}}\right) = \frac{1}{3}\rho {L_T}^3 \dot{\theta} + m_S {L_T}^2 \dot{\theta} = \left(\frac{1}{3}\rho {L_T}^3 + m_S {L_T}^2\right)\dot{\theta}$$

$$\left(\frac{\partial \mathcal{L}}{\partial \theta}\right) = \frac{1}{2}(\rho_c - \rho_b) g {L_T}^2 \sin(\theta) - m_S g (RB) L_T \sin(\theta)$$

Therefore,

$$\frac{\partial}{\partial t}\left(\left(\frac{1}{3}\rho {L_T}^3 + m_S {L_T}^2\right)\dot{\theta}\right) = Q_\theta + \left(\frac{1}{2}(\rho_c - \rho_b) g {L_T}^2 \sin(\theta) - m_S g (RB) L_T \sin(\theta)\right)$$

$$\ddot{\theta} = \left[Q_\theta + \frac{1}{2}(\rho_c - \rho_b) g {L_T}^2 \sin(\theta) - m_S g (RB) L_T \sin(\theta)\right] * \left(\frac{1}{3}\rho {L_T}^3 + m_S {L_T}^2\right)^{-1}$$

For the third coordinate, note ϕ here is q3.

$$\frac{\partial}{\partial t}\left(\frac{\partial \mathcal{L}}{\partial \dot{\phi}}\right) = Q_\phi + \left(\frac{\partial \mathcal{L}}{\partial \phi}\right)$$

Where,

$$\left(\frac{\partial \mathcal{L}}{\partial \dot{\phi}}\right) = 0$$

$$\left(\frac{\partial \mathcal{L}}{\partial \phi}\right) = 0$$

Therefore,

$$\ddot{\phi} = 0$$

Appendix D: Lift and Drag Relationships

The following represents the four Normal and Axial Forces upon SUSK throughout its motion. The effective angle of attack is denoted in section 4.1.2. This is then used to calculate the Normal and Parallel Forces to numerically solve for Q_θ. In the table below $\alpha = \alpha_{effective}$.

Table 8: Geometric Normal and Axial Forces

Phase	Normal Force	Axial Force
2	$N = L\cos(\alpha) + D\sin(\alpha)$	$A = L\sin(\alpha) - D\cos(\alpha)$
3	$N = L\cos(\alpha) + D\sin(\alpha)$	$A = -L\sin(\alpha) + D\cos(\alpha)$
6	$N = L\cos(\alpha) - D\sin(\alpha)$	$A = L\sin(\alpha) - D\cos(\alpha)$
7	$N = L\cos(\alpha) - D\sin(\alpha)$	$A = -L\sin(\alpha) + D\cos(\alpha)$

Appendix E: SUSK Inertia Tensor

The following Inertia was produced in SolidWorks from the full SUSK model provided in section [3.1.1]. The inertia has a reference point from the origin of the SUSK body, where the tether connection lays on the servo control box; this is denoted in section [4.1.1].

Recall that the inertial tensor is as followed,

$$I = J = \begin{bmatrix} J_{xx} & 0 & 0 \\ 0 & J_{yy} & 0 \\ 0 & 0 & J_{zz} \end{bmatrix}$$

From SolidWorks we are able to determine each of these eigenvalues,

That,

$$J = \begin{bmatrix} 14700 & 0 & 0 \\ 0 & 14700 & 0 \\ 0 & 0 & 5780 \end{bmatrix} \quad [lb * in^2]$$

Therefore,

$$J = \begin{bmatrix} 4.3018 & 0 & 0 \\ 0 & 4.3018 & 0 \\ 0 & 0 & 1.6915 \end{bmatrix} \quad [kg * m^2]$$

The following matrix is used in the dynamic simulation for the Euler Orientation Angles of SUSK.

Appendix F: MATLAB Code for Draft Calculations

```
clear; clc;

syms draft;

V = 94.275;   % Volume of submerged hull (in^3)

L = 60;  % Length of hull (in)

R = 4;   % Radius of hull (in)

eqn = L*(R^2 *acos((R-draft)/R)-(R-draft)*sqrt(2*R*draft-draft^2)) == V;

delta = vpasolve(eqn, draft);

fprintf('The Draft of the SUSK system is %.2f inches.\n', delta);

The Draft of the SUSK system is 0.57 inches.
```

Published with MATLAB® R2019b

Appendix G: MATLAB Code for Wing Cross Sectional Area and Volume

```
clear all; clc;


P = [4.5    -0.42489;
    4.97763 -0.42534;
    5.43564 -0.42804;
    5.87565 -0.432;
    6.30027 -0.4356;
    6.70644 -0.43758;
    7.09011 -0.43641;
    7.44804 -0.43038;
    7.77645 -0.41796;
    8.07246 -0.39726;
    8.33238 -0.36648;
    8.55342 -0.32445;
    8.73306 -0.26892;
    8.86842 -0.19836;
    8.95824 -0.10647;
    9 0.01224;
    8.99271 0.09603;
    8.93493 0.21105;
    8.82675 0.33705;
    8.66844 0.46395;
    8.46216 0.58905;
    8.20899 0.71217;
    7.9119  0.83043;
    7.57431 0.94185;
    7.20009 1.04436;
    6.79383 1.13634;
    6.36066 1.21608;
    5.90598 1.28196;
    5.43591 1.33209;
    4.9635  1.36386;
    4.5     1.37493;
    4.0365  1.36386;
    3.56409 1.33209;
    3.09402 1.28196;
    2.63934 1.21608;
    2.20617 1.13634;
    1.79991 1.04436;
    1.42569 0.94185;
    1.0881  0.83043;
    0.79101 0.71217;
    0.53784 0.58905;
    0.33156 0.46395;
    0.17325 0.33705;
    0.06507 0.21105;
    0.00729 0.09603;
    0       0.01224;
    0.04176 -0.10647;
```

```
    0.13158 -0.19836;
    0.26694 -0.26892;
    0.44658 -0.32445;
    0.66762 -0.36648;
    0.92754 -0.39726;
    1.22355 -0.41796;
    1.55196 -0.43038;
    1.90989 -0.43641;
    2.29356 -0.43758;
    2.69973 -0.4356;
    3.12435 -0.432;
    3.56436 -0.42804;
    4.02237 -0.42534;
    4.5     -0.42489];

polyin = polyshape(P);
plot(polyin)
axis equal
height = 36                                                    %[in]
Cross_Sectional_Wing_Area = area(polyin)                       %[in^2]
Volume_of_Wing = Cross_Sectional_Wing_Area * height            %[in^3]
```

Published with MATLAB® R2019b

Appendix H: MATLAB Code for Dynamic Simulation

```
clc; clear variables; close all;

global Qq2 L rho M q2lim vcurrent Qq6 J2 S A_t rho_t
global C_p Servo_Torque A_b Re visc Servo_Speed

size = 'small';
l_boat = 1.5;                       %
w_boat = 0.9;                      %
hull_radius = .1016;
A_b = (2)*(.07125)*((2*pi*hull_radius*l_boat)+(2*pi*hull_radius^2));
Servo_Speed = 2;
L =     3.66;
M = 27  * (0.453592);
rho = 997;

vcurrent = .60; % 2 ft/s
S = 0.20903184;
A_t = pi*0.074^2;
rho_t = 0.2;
C_p = 16/27;
visc = 1E-3;
SF = 20;

q2lim =  52*pi/180;

if strcmp(size,'large') % not used
l_boat = l_boat*SF;
w_boat = w_boat*SF;
visc = visc*1;
A_b = l_boat*w_boat;
Servo_Torque = Servo_Torque*1;
Servo_Speed = Servo_Speed*1;
L = L*2*SF;
M = M*SF^3;
rho = rho*1;
Qq2 = Qq2*1;
q2lim = q2lim*1;
vcurrent = vcurrent*sqrt(SF);
Qq6 = Qq6*1;
J2 = J2*SF^5;
S = S*SF^2;
A_t = A_t*SF^2;
rho_t = rho_t*SF^2;
C_p = C_p*1;
end

iterations = 10000;
subiterations = 5;
tinit = 0;
tfinal = 90;

q2_init = -90*pi/180;
q2dot_init = -0.01;
theta_init = 0;
thetadot_init = 0;

q2_cum = zeros(1,(subiterations - 1)*iterations);
```

```
q2dot_cum = zeros(1,(subiterations - 1)*iterations);
alpha_cum = zeros(1,(subiterations - 1)*iterations);
t_cum = zeros(1,(subiterations - 1)*iterations);
power_cum = zeros(1,(subiterations - 1)*iterations);
vctotal_cum = zeros(1,(subiterations - 1)*iterations);
tension_cum = zeros(1,(subiterations - 1)*iterations);
moment_cum = zeros(1,(subiterations - 1)*iterations);
theta_cum = zeros(1,(subiterations - 1)*iterations);
thetadot_cum = zeros(1,(subiterations - 1)*iterations);
loverd_cum = zeros(1,(subiterations - 1)*iterations);

for n = 1:iterations
    if abs(q2dot_init) > 100;
        break
    end

tspanfinal = (tfinal - tinit)/iterations*n;
tspaninit = (tfinal - tinit)/iterations*(n-1);
tsubspan = linspace(tspaninit, tspanfinal, subiterations);
vcurrent_vec = [0; vcurrent; 0]; %Current Vector
rboat_vec = [-L*sin(q2_init); L*cos(q2_init); 0];
vboat_vec = [-L*q2dot_init*cos(q2_init); -L*q2dot_init*sin(q2_init); 0]; % Boat Velocity
Vector
boat_hat = [cos(q2_init); sin(q2_init); 0];
vinduced_vec = -vboat_vec;
vctotal_vec = vinduced_vec + vcurrent_vec;
vctotal = norm(vctotal_vec);
w_angle = q2_init + theta_init;
w_hat = [cos(w_angle); sin(w_angle); 0];
cosalpha = dot(w_hat, vctotal_vec)/vctotal;

if cosalpha >= 0
    vel_direction = atan2(vctotal_vec(2), vctotal_vec(1));
    if abs(vel_direction - w_angle) >= pi/2
        if vel_direction < w_angle
            vel_direction = vel_direction + 2*pi;
        else
            w_angle = w_angle + 2*pi;
        end
    end
    if vel_direction >= w_angle
        alpha = acos(cosalpha);
    elseif vel_direction < w_angle
        alpha = -acos(cosalpha);
    end
    alpha_deg = alpha*180/pi;
    [CL, CD] = getliftanddragcoeff(alpha_deg);
    Lift = 0.5*rho*vctotal^2*S*CL;
    Drag = 0.5*rho*vctotal^2*S*CD;
    Drag_Other = turbine_and_boat_drag(vctotal);
    Drag = Drag + Drag_Other;
    Force_Normal_To_Wing = Lift*cos(alpha) + Drag*sin(alpha);
    Force_Axial_To_Wing = -Lift*sin(alpha) + Drag*cos(alpha);
    Force_Along_Tether = Force_Normal_To_Wing*sin(theta_init) -
Force_Axial_To_Wing*cos(theta_init);
elseif cosalpha < 0
    vel_direction = atan2(vctotal_vec(2), vctotal_vec(1));
    psi1 = mod(vel_direction,2*pi);
    psi2 = mod((w_angle + pi),2*pi);
    if abs(psi1 - psi2) >= pi/2
        if psi1 < psi2
            psi1 = psi1 + 2*pi
        else
            psi2 = psi2 + 2*pi;
```

```
        end
    end
    if psi1 >= psi2
        alpha = -acos(-cosalpha);
    elseif psi2 > psi1
        alpha = acos(-cosalpha);
    end
    alpha_deg = alpha*180/pi;
    [CL, CD] = getliftanddragcoeff(alpha_deg);
    Lift = 0.5*rho*vctotal^2*S*CL;
    Drag = 0.5*rho*vctotal^2*S*CD;
    Drag_Other = turbine_and_boat_drag(vctotal);
    Drag = Drag + Drag_Other;
    Force_Normal_To_Wing = Lift*cos(alpha) + Drag*sin(alpha);
    Force_Axial_To_Wing = Lift*sin(alpha) - Drag*cos(alpha);
    Force_Along_Tether = Force_Normal_To_Wing*sin(theta_init) -
Force_Axial_To_Wing*cos(theta_init);
end
Tether_Tension = sqrt(Lift^2 + Drag^2 - Force_Along_Tether^2);
Re = rho*vctotal*l_boat/visc;
Qq2 = L*Force_Along_Tether;

trim_thetas = [41 -38 -46 -46 41 41 34 -46]*pi/180;

position_and_speed_case = 1;
if q2dot_init < 0
    if q2_init < -q2lim
        position_and_speed_case = 1;
    elseif q2_init < 0
        position_and_speed_case = 2;
    elseif q2_init >= 0 && q2_init <= q2lim
        position_and_speed_case = 3;
    elseif q2_init > q2lim
        position_and_speed_case = 4;
    end
elseif q2dot_init >= 0
    if q2_init < -q2lim
        position_and_speed_case = 5;
    elseif q2_init < 0
        position_and_speed_case = 6;
    elseif q2_init >= 0 && q2_init <= q2lim
        position_and_speed_case = 7;
    elseif q2_init > q2lim
        position_and_speed_case = 8;
    end
end

if abs(trim_thetas(position_and_speed_case) - theta_init) > 0.02
    thetadot_init = sign(trim_thetas(position_and_speed_case) - theta_init)*Servo_Speed;
else
    thetadot_init = 0;
end

q(:,1) = Qq2/L^2*(rho_t*L/3 + M)^(-1)*(tsubspan - tsubspan(1)).^2/2 +
q2dot_init*(tsubspan - tsubspan(1)) + q2_init;
q(:,2) = Qq2/L^2*(rho_t*L/3 + M)^(-1)*(tsubspan - tsubspan(1)) + q2dot_init;
q(:,3) = theta_init + thetadot_init*(tsubspan - tsubspan(1));
q(:,4) = thetadot_init;

%  Calculate Lift to Drag Ratio
loverd = Lift/Drag;
% Add to cumulative arrays of coordinates
q2_cum((n-1)*(subiterations - 1) + 1: n*(subiterations - 1)) = q(1:end-1,1);
q2dot_cum((n-1)*(subiterations - 1) + 1: n*(subiterations - 1)) = q(1:end-1,2);
```

```
theta_cum((n-1)*(subiterations - 1) + 1: n*(subiterations - 1)) = q(1:end-1,3);
thetadot_cum((n-1)*(subiterations - 1) + 1: n*(subiterations - 1)) = q(1:end-1,4);
alpha_cum((n-1)*(subiterations - 1) + 1: n*(subiterations - 1)) = alpha;


% End of previous interval becomes new initial conditions
q2_init = q(end,1);
q2dot_init = q(end,2);
theta_init = q(end,3);
thetadot_init = q(end,4);

% Add to cumulative arrays
tension_cum((n-1)*(subiterations - 1) + 1:n*(subiterations - 1)) = Tether_Tension;
moment_cum((n-1)*(subiterations - 1) + 1:n*(subiterations - 1)) = Qq2;
t_cum((n-1)*(subiterations - 1) + 1:n*(subiterations - 1)) = tsubspan(1:end-1);
vctotal_cum((n-1)*(subiterations - 1) + 1:n*(subiterations - 1)) = vctotal; power_cum((n-
1)*(subiterations - 1) + 1:n*(subiterations - 1)) =...
        abs(C_p*0.5*rho*vctotal^2*A_t*dot(vctotal_vec,[sin(q2_init); cos(q2_init); 0]));
    loverd_cum((n-1)*(subiterations - 1) + 1:n*(subiterations - 1)) = loverd;
end

fprintf('Average lift = %f\n', mean(Lift));
fprintf('Average drag = %f\n', mean(Drag));

close all;
cartesian_cum = [L*cos(q2_cum); -L*sin(q2_cum); 0*q2_cum];
limit_cartesian1 = [L*cos(q2lim); -L*sin(q2lim);0];
limit_cartesian2 = [L*cos(q2lim); L*sin(q2lim);0];
x = cartesian_cum(1,:);
y = cartesian_cum(2,:);
z = cartesian_cum(3,:);
figure('name','q2andq2dot');
subplot(5,1,1)
plot(t_cum, q2_cum*180/pi,'linewidth',2);
ylabel('q2 [deg]','fontsize',14,'interpreter','latex');
title('q2 vs t','interpreter','latex','fontsize',14);
subplot(5,1,2)
plot(t_cum, q2dot_cum*180/pi,'linewidth',2);
ylabel('$$\dot{q_2} \left[\frac{deg}{s}\right]$$','fontsize',14,'interpreter','latex');
title('$$\dot{q_2}$$ vs t','interpreter','latex','fontsize',14);
subplot(5,1,3)
plot(t_cum, theta_cum*180/pi,'linewidth',2);
ylabel('$$\theta [deg]$$','fontsize',14,'interpreter','latex');
title('$$\theta$$ vs t','interpreter','latex','fontsize',14);
subplot(5,1,4)
plot(t_cum, thetadot_cum*180/pi,'linewidth',2);
ylabel('$$\dot{\theta}
\left[\frac{deg}{s}\right]$$','fontsize',14,'interpreter','latex');
title('$$\dot{\theta}$$ vs t','interpreter','latex','fontsize',14);
subplot(5,1,5)
plot(t_cum, alpha_cum*180/pi,'linewidth',2);
xlabel('$$t$$','fontsize',18,'interpreter','latex');
ylabel('$$\alpha [deg]$$','fontsize',14,'interpreter','latex');
title('$$\alpha$$ vs t','interpreter','latex','fontsize',14);
fig = gcf;
fig.PaperUnits = 'inches';
fig.PaperPosition = [0 0 5 7];
print('MostRecentangles','-dpng')

figure('name','vctotal');
subplot(5,1,1)
plot(t_cum, vctotal_cum/vcurrent,'linewidth',2);
ylabel('$$\frac{V_a}{V_{current}}$$','interpreter','latex','fontsize',16);
```

```
title('Apparent Velocity as a Multiple of Current Velocity vs
t','interpreter','latex','fontsize',14)
subplot(5,1,2)
plot(t_cum, tension_cum,'linewidth',2);
ylabel('Tether Tension [N]','interpreter','latex','fontsize',14);
title('Tether Tension vs t','interpreter','latex','fontsize',14)
subplot(5,1,3)
plot(t_cum, moment_cum,'linewidth',2);
ylabel('q2 [Nm]','interpreter','latex','fontsize',14);
title('q2 vs t','interpreter','latex','fontsize',14)
subplot(5,1,4)
plot(t_cum, power_cum,'linewidth',2);
ylabel('Power [kW]','interpreter','latex','fontsize',14);
title('Power vs t','interpreter','latex','fontsize',14);
subplot(5,1,5)
plot(t_cum,loverd_cum,'linewidth',2);
ylabel('$$\frac{L}{D}$$','fontsize',14,'interpreter','latex')
xlabel('t (s)','interpreter','latex','fontsize',18)
title('Lift to Drag Ratio vs t','interpreter','latex','fontsize',14)
fig = gcf;
fig.PaperUnits = 'inches';
fig.PaperPosition = [0 0 7 9];
print('MostRecentOther','-dpng')

figure('name','cartesian2d');
plot([0 limit_cartesian1(2)],[0 limit_cartesian1(1)],'k-.','linewidth',1.5)
hold on
plot(y,x,'linewidth',2);
hold on
plot(0,0,'o','markersize',15)
plot([0 limit_cartesian2(2)],[0 limit_cartesian2(1)],'k-.','linewidth',1.5)
axis equal
legendd = legend('SUSK Range');
set(legendd,'fontsize',16)
xlabel('x [m]','fontsize',14);
ylabel('y [m]','fontsize',14);
title('SUSK Cartesian Positioning','fontsize',17)
print('MostRecentCartesian','-dpng')

fprintf('Average Power = %f\n', mean(power_cum));

 figure;
 for i = 1:length(t_cum)/100:length(t_cum);
     plot3(x,y,z);
     xlim([-1.1*L 1.1*L]);
     ylim([-1.1*L 1.1*L]);
     zlim([-1.1*L 1.1*L]);
 hold on
     xlabel('y [m]');
     ylabel('x [m]');
     zlabel('z [m]');
     title('3D Position With Tether');
     plot3([0 x(i)], [0 y(i)], [0 z(i)],'k');
     plot3([0 x(i)], [0 y(i)], [0 z(i)],'xk');
     title(strcat('t = ', num2str(t_cum(i))));
     plot3(x(i), y(i), z(i),'.r','markersize',25);
     pause(0.001);

     hold off
 end


function xdot = Simple_ODE(t,x)
% q2, q2dot, theta, thetadot
```

```
global Qq2 L rho M rho_t Servo_Torque J2
xdot = ones(4,1);
xdot(1) = x(2);
xdot(2) = Qq2/L^2*(rho_t*L/3 + M)^(-1);
xdot(3) = x(4);
xdot(4) = 0;

end

function [cl, cd] = getliftanddragcoeff(alpha_deg)
if alpha_deg < -10 && alpha_deg >= -90
    cl = 0.00028125*alpha_deg^2 + 0.020625*alpha_deg - 0.421875;
    cd = 0.00002235577*alpha_deg^2 - 0.007014423*alpha_deg - 0.0123798;
elseif alpha_deg <= 16
     cl = -0.000376346*alpha_deg^3 + 0.00061774*alpha_deg^2 + 0.135442*alpha_deg +
0.3163;
    cd = 0.000346154*alpha_deg^2 - 0.00053846*alpha_deg + 0.02;
elseif alpha_deg <= 90
    cl = -0.00044515*alpha_deg^2 + 0.032321145*alpha_deg + 0.69682035;
    cd = 0.0000949879*alpha_deg^2 + 0.00749885*alpha_deg - 0.0442985;
else
    disp('Error: Angle of attack exceeds 90 degrees')
end

end
function drag = turbine_and_boat_drag(velocity)
global rho A_t A_b
turbine_drag = (4/9)*velocity^2*A_t*rho; %Betz Turbine
boat_drag_coeff = 0.04;
boat_drag = boat_drag_coeff*0.5*rho*velocity^2*A_b;
drag = turbine_drag + boat_drag + .05*.5*.008374*velocity^2*rho; % + wing drag
end
```

Published with MATLAB® R2019b

Appendix I: MATLAB Code for Roll Analysis

```
clear all; close all; clc;


% import Tracker Data:

left_hullx = [-1.5679608658764304
-1.5679608658764312
-1.5744669275605654
-1.5679608658764304
-1.5744669275605654
-1.5679608658764304
-1.5744669275605654
-1.5809729892446995
-1.5744669275605654
-1.5874790509288346
-1.5744669275605654
-1.5614548041922962
-1.5679608658764312
-1.5874790509288346
-1.5744669275605654
-1.6004911742971037
-1.6200093593495062
-1.6395275444019113
-1.6460336060860454
-1.6460336060860454
-1.6330214827177763
-1.6395275444019104
-1.6460336060860454
-1.6525396677701796
-1.6720578528225838
-1.685069976190852
-1.6915760378749871
-1.7045881612432563
-1.6980820995591221
-1.7045881612432563
-1.7306124079797947
-1.7241063462956596
-1.7176002846115255
-1.7045881612432563
-1.750130593032198
-1.7371184696639297
-1.7371184696639288
-1.7631427164004672
-1.7696487780846022
-1.763142716400468
-1.7371184696639288
-1.7436245313480638
-1.7371184696639288];
```

```
left_hully = [ -0.00650606168413459
-0.01301212336826918
-0.01301212336826918
-0.03903637010480754
-0.04554243178894213
-0.07807274020961463
-0.14313335705096009
-0.1626515421033643
-0.18867578883990266
-0.22120609726057516
-0.279760652417786
-0.3122909608384594
-0.3773515776798049
-0.3578333926274011
-0.32530308420672815
-0.2732545907336519
-0.23421822062884434
-0.08457880189374967
0.058554555157210864
0.07807274020961463
0.06506061684134545
0.07156667852548004
0.0
-0.12361517199855676
-0.16265154210336386
-0.15614548041922927
-0.12361517199855676
-0.08457880189374967
-0.00650606168413459
0.058554555157210864
0.09108486357788381
0.09108486357788426
0.09108486357788426
0.11060304863028758
0.0975909252620184
0.08457880189374922
0.07156667852548049
0.06506061684134545
0.06506061684134545
0.07156667852548004
0.06506061684134545
0.0650606168413459
0.07807274020961508];


right_hullx = [ 1.4313335705096053
1.4183214471413352
1.398803262088931
1.4248275088254703
1.4183214471413343
1.4118153854572002
1.398803262088932
1.398803262088932
1.3857911387206627
1.3857911387206618
```

```
1.3662729536682576
1.3532608302999902
1.3467547686158552
1.3402487069317202
1.3467547686158552
1.3597668919841244
1.3727790153523944
1.3727790153523927
1.3727790153523944
1.3922972004047978
1.4248275088254694
1.4638638789302778
1.4378396321937386
1.398803262088931
1.3857911387206627
1.3922972004047978
1.3922972004047969
1.3597668919841244
1.3597668919841244
1.3597668919841244
1.346754768615856
1.333742645247587
1.3337426452475851
1.327236583563451
1.3077183985110477
1.3142244601951818
1.3077183985110477
1.3012123368269135
1.3012123368269126
1.320730521879316
1.3207305218793168
1.3207305218793168
1.3207305218793168];


right_hully = [ 0.058554555157210864
0.07807274020961463
0.07807274020961463
0.08457880189374922
0.10409698694615299
0.11060304863028758
0.14963941873509512
0.15614548041922927
0.1951818505240368
0.22771215894470975
0.2602424673653827
0.312290960838459
0.32530308420672815
0.3448212692591319
0.33831520757499733
0.2927727757860552
0.2667485290495173
0.18216972715576762
0.11060304863028758
0.02602424673653836
```

```
0.01301212336826918
0.06506061684134545
0.1561454804192297
0.14963941873509512
0.18867578883990266
0.20168791220817184
0.18867578883990266
0.08457880189374922
0.03903637010480754
0.019518185052403325
0.0
-0.01301212336826918
-0.039036370104807094
-0.01301212336826918
-0.03253030842067295
-0.01951818505240377
-0.01301212336826918
-0.03253030842067295
0.0
-0.00650606168413459
-0.00650606168413459
-0.013012123368268735
-0.00650606168413459];


left_hull = [left_hullx, left_hully];


right_hull = [right_hullx, right_hully];


servo_center = [ zeros(43,2)];


time = [ 0.0
0.03333333333333303
0.06666666666666697
0.1
0.1333333333333335
0.16666666666666652
0.2
0.23333333333333348
0.2666666666666665
0.30000000000000043
0.3333333333333335
0.36666666666666653
0.4
0.43333333333333346
0.46666666666666695
0.5
0.533333333333333
0.566666666666667
0.6
0.6333333333333335
0.666666666666667
```

```
0.7
0.7333333333333335
0.7666666666666665
0.8000000000000005
0.8333333333333335
0.8666666666666665
0.9
0.9333333333333335
0.966666666666667
1.0
1.0333333333333334
1.0666666666666669
1.1
1.1333333333333335
1.166666666666667
1.2
1.2333333333333334
1.2666666666666666
1.3000000000000005
1.3333333333333335
1.3666666666666665
1.4];


% Damping
% at t = .467, start wave, row 15


hull_r = right_hull(15:43,:);
hull_l = left_hull(15:43,:);
origin = servo_center(15:43,:);
time_wave = time(15:43);


dy = (abs(origin(:,2)-hull_l(:,2))+abs(origin(:,2)-hull_r(:,2)))-0;


y = dy/dy(1,:);


plot(time_wave,y)
title('Amplitude vs. Time','interpreter','latex','fontsize',17);
xlabel('Time [s]','interpreter','latex','fontsize',15);
ylabel('$$\frac{dy}{dy_{0}}$$','interpreter','latex','fontsize',15);
ylim([0,1])




u1 = y(1,:);
u2 = y(12,:);
u3 = y(21,:);


m = log(u1/u2);
zeta = (m*((m^2+4*pi^2)^.5))/(m^2+4*pi^2)
```

```
% damped SDOF; roll / q4 / phi


% aluminum rod
l = .9144;
r = .5;
cross_rod = (pi*r^2)/1550;
volume_rod = cross_rod*l;
rod_mass = 1.25; %kg , estimate
E = 68*10^9;
density = 2700;


% force p(t)


V = .1079;
m = 14.37;
g = 9.81;
rho = 1025;


F_b = V*rho*g;  % [N]
F_g = m*g;  % [N]
delta_y = -.126;    % [m]


U = (F_b-F_g)*delta_y % [J]
P_t = F_b-F_g   % [N]


K = 0;
L_roll = K - U   % [J]
```

Published with MATLAB® R2019b

References

Airborne wind energy captures high altitude wind power. Global Opportunity Explorer. (2019, May 7). Retrieved January 27, 2022, from https://goexplorer.org/airborne-wind-energy-captures-high-altitude-wind-power/#:~:text=Unlike%20conventional%20wind%20turbines%2C%20which,both%20stronger%20and%20more%20consistent.

Alvarez, Miguel, et al. "An Integrated Model of the Kite and Tether Dynamics of a Marine Hydrokinetic Energy Harvesting System." *2021 European Control Conference (ECC)*, 2021, DOI: 10.23919/ecc54610.2021.9655075.

Anderson, J. D. (2017). *Fundamentals of aerodynamics*. McGraw-Hill Education.

Aye-Addo, N., O'Connor, J., Perez, R., "Design of a Scale-Model Tethered Undersea Kite for Power Generation," WPI Major Qualifying Project (MQP) Report, Advisor: D. Olinger, Co-Advisor: A. Linn, 2014

Beccario, C. (n.d.). *A global map of wind, weather, and ocean conditions*. earth. Retrieved January 27, 2022, from https://earth.nullschool.net/#current/ocean/surface/currents/orthographic=289.18,38.08,3635/loc=-66.776,38.362

Cherubini, A., Papini, A., Vertechy, R., & Fontana, M. (2015, July 31). *Airborne Wind Energy Systems: A review of the technologies*. Renewable and Sustainable Energy Reviews. Retrieved October 22, 2021, from https://www.sciencedirect.com/science/article/pii/S1364032115007005#bib9.

Denchak, M. (2021, August 6). *Fossil fuels: The dirty facts*. NRDC. Retrieved October 24, 2021, from https://www.nrdc.org/stories/fossil-fuels-dirty-facts.

Diehl, M. (2013). Airborne wind energy: Basic concepts and physical foundations. *Airborne Wind Energy*, 3–22. https://doi.org/10.1007/978-3-642-39965-7_1

Fredette, Ryan A. "Scale-Model Testing of Tethered Undersea Kites for Power Generation." *Worcester Polytechnic Institute*, 2015.

Higgins, A., O'Hara, J., Pepic, M., Porter, D., Melander, P., "Design and Testing of a Scale-Model Surface Undersea Kite (SUSK)," WPI Major Qualifying Project (MQP) Report DJO-1701, Advisor: D. Olinger, co-Advisor: N. Burnham, 2017

Kool, T. (2020, March 25). *The Complete History of Fossil Fuels*. Oil Price. Retrieved October 24, 2021, from https://oilprice.com/Energy/Energy-General/The-Complete-History-Of-Fossil-Fuels.html.

Kuo, G. (2021, February 23). *When fossil fuels run out, what then?* MAHB. Retrieved October 24, 2021, from https://mahb.stanford.edu/library-item/fossil-fuels-run/.

Loyd, M. L. (1980). Crosswind Kite Power (for large-scale wind power production). *Journal of Energy*, *4*(3), 106–111. https://doi.org/10.2514/3.48021

Miller, L. M., Gans, F., & Kleidon, A. (2011, November 29). *Jet stream wind power as a renewable energy resource: Little Power, big impacts*. Earth System Dynamics. Retrieved October 22, 2021, from https://esd.copernicus.org/articles/2/201/2011/.

NASA. (n.d.). *Induced drag coefficient*. NASA. Retrieved February 10, 2022, from https://www.grc.nasa.gov/www/k-12/airplane/induced.html#:~:text=For%20a%20rectangular%20wing%2C%20the,shaping%20of%20the%20wing%20tips.

Olinger, D. J., & Wang, Y. (2015). Hydrokinetic energy harvesting using tethered undersea kites. *Journal of Renewable and Sustainable Energy*, *7*(4), 043114. DOI: 10.1063/1.4926769

Petilli, N. (2021, April). *Analysis of a Re-designed Surface Undersea Kite System*. Worcester Polytechnic Institute.

Rampion Offshore Wind. (2021, April 12). *The South Coast's first offshore Wind Farm*. Rampion Offshore Wind. Retrieved October 24, 2021, from https://www.rampionoffshore.com/.

Reed, J., Cobb, M., Daniels, J., Siddiqui, A., Muglia, M., & Vermillion, C. (2020). Hierarchical control design and performance assessment of an Ocean Kite in a turbulent flow environment. *IFAC-PapersOnLine*, *53*(2), 12726–12732. DOI: 10.1016/j.ifacol.2020.12.1887

The Future of Renewable Energy. Minesto. (2021). Retrieved March 2, 2022, from https://minesto.com/our-technology#:~:text=Minesto's%20Deep%20Green%20technology%20generates,current%20to%20move%20the%20kite.

The world counts. (n.d.). Retrieved October 22, 2021, from https://www.theworldcounts.com/stories/current_world_energy_consumption.

US Department of Commerce, N. O. and A. A. (2013, June 1). *How fast is the Gulf Stream?* NOAA's National Ocean Service. Retrieved January 27, 2022, from https://oceanservice.noaa.gov/facts/gulfstreamspeed.html

U.S. Energy Information Administration (EIA). (2021, September 7). *Hydropower made up 66% of Brazil's electricity generation in 2020*. U.S. Energy Information Administration - EIA - independent statistics and analysis . Retrieved October 24, 2021, from https://www.eia.gov/todayinenergy/detail.php?id=49436.

U.S. Energy Information Administration (EIA). (2020, September 14). *Fossil fuels account for the largest share of U.S. energy production and consumption*. U.S. Energy Information Administration - EIA - independent statistics and analysis. Retrieved October 24, 2021, from https://www.eia.gov/todayinenergy/detail.php?id=45096#.

U.S. Energy Information Administration (EIA). (2021, May 2). *Renewable energy explained*. U.S. Energy Information Administration - EIA - independent statistics and analysis. Retrieved October 24, 2021, from https://www.eia.gov/energyexplained/renewable-sources/.

Volume of a partially filled cylinder. Volume of a partially filled cylinder with calculator - Math Open Reference. (n.d.). Retrieved March 9, 2022, from https://www.mathopenref.com/cylindervolpartial.html

Wind speed 2018 data. (2018). Retrieved January 27, 2022, from https://www.ncei.noaa.gov/pub/data/ccd-data/wndspd18.dat